Simultaneous measurement of air flow conditions and the resultant blade and gearbox loading at large-scale cooling system fans

by

Jacques Muiyser

Thesis presented in partial fulfilment of the requirements for the degree of Master of Science in Mechanical Engineering in the Faculty of Engineering at Stellenbosch University

Department of Mechanical and Mechatronic Engineering,
University of Stellenbosch,
Private Bag X1, 7602 Matieland, South Africa.

Supervisors:

Dr. D.N.J. Els Dr. S.J. van der Spuy

December 2012

The financial assistance of the National Research Foundation (NRF) towards this research is hereby acknowledged. Opinions expressed and conclusions arrived at, are those of the author and are not necessarily to be attributed to the NRF.

Declaration

By submitting this thesis electronically, I declare that the entirety of the work contained therein is my own, original work, that I am the sole author thereof (save to the extent explicitly otherwise stated), that reproduction and publication thereof by Stellenbosch University will not infringe any third party rights and that I have not previously in its entirety or in part submitted it for obtaining any qualification.

Date: .....

Abstract

Simultaneous measurement of air flow conditions and the resultant blade and gearbox loading at large-scale cooling system fans

J. Muiyser

Department of Mechanical and Mechatronic Engineering,
University of Stellenbosch,
Private Bag X1, 7602 Matieland, South Africa.

Thesis: MScEng (Mech)

December 2012

Axial flow fans used in large-scale air-cooled steam condensers (ACSCs) may operate under distorted inflow conditions. These conditions occur due to the prevailing wind conditions, the presence of buildings, and the location of the fan within the ACSC. Fans located on the periphery of the ACSC are affected the most due to their exposure to strong winds and the inner fans drawing in air past them. Distorted inflow conditions cause varying fan blade and gearbox loading conditions.

The purpose of the investigation was to simultaneously measure the inlet air flow and the resultant blade and gearbox loading conditions of a single fan located on the periphery of a large-scale ACSC. Inlet and heat exchanger bundle outlet air flow velocities were measured using a combination of ultrasonic and propeller anemometers while blade loading was measured with strain gauges attached at the neck of the specific blade being monitored. Strain gauges were also attached to the low-speed fan shaft to measure gearbox loading.

Measurements were recorded over a period of 8 days where it was found that increased wind resulted in increased air flow in the axial direction of the fan, which then caused a reduction in average blade loading. This was due to a decreased static pressure rise over the fan. The fan blade was found to vibrate at its own natural frequency of 6 Hz when excited by the variable aerodynamic loading. The aerodynamic loading was extracted from the measured data and was found to correlate well with previous experimental work performed by Bredell *et al.* (2006*a*). Shaft bending stresses and torque were found to oscillate at the fan's rotational frequency of 2 Hz with a large torque exerted on the shaft during fan start-up.

Uittreksel

Gelyktydige meting van lugvloei toestande en die gevolglike lem en ratkas belastings by groot verkoelingstelselwaaiers

J. Muiyser

Departement Meganies en Megatroniese Ingenieurswese,
Universiteit van Stellenbosch,
Privaatsak X1, 7602 Matieland, Suid Afrika.

Tesis: MScIng (Meg)

Desember 2012

Aksiaalvloeiwaaiers wat by groot lugverkoelde stoomkondensors gebruik word, werk dikwels onder verwronge inlaat lugvloei toestande wat geskied as gevolg van heersende winde, die teenwoordigheid van geboue en die posisie van die waaier in die kondensor. Waaiers wat geleë is op die rand van die kondensor word die meeste beïnvloed as gevolg van blootstelling aan die sterk winde en dwarsvloei wat deur die binneste waaiers geïnduseer word. Verwronge inlaat lugvloei veroorsaak gevolglik variërende waaierlem en ratkas belastingstoestande.

Die doel van hierdie ondersoek was om terselfdetyd die inlaat lugvloei asook waaierlem en ratkas belastingstoestande van 'n enkele waaier wat op die rand van 'n grootskaalse lugverkoelde stoomkondensor geleë is, te meet. Waaier inlaat en warmteruiler uitlaat lugvloei snelhede is gemeet met 'n kombinasie van ultrasoniese- en skroefwindsnelheidsmeters terwyl die lem en ratkas belastings gemeet is met rekstrokies.

Metings is oor 'n tydperk van 8 dae geneem. Die bevindinge toon dat 'n toename in windsnelheid 'n toename in aksiale lugvloei tempo, deur die waaier veroorsaak. 'n Afname in die gemiddelde lembelasting is waargeneem as gevolg van 'n afname in die waaier statiese druk. Daar is ontdek dat die waaierlem teen 'n natuurlike frekwensie van 6 Hz vibreer wanneer dit opgewek word deur die wisselende aerodinamiese belasting. Die aerodinamiese belasting is verkry uit die gemete data en vergelyk goed met die numeriese werk van Bredell *et al.* (2006*a*). Daar is ook bevind dat waaier-as buigspannings en wringkragte ossileer teen die waaier se rotasiefrekwensie van 2 Hz met 'n groot wringkrag wat op die as uitgeoefen word wanneer die waaier aangeskakel word.

Acknowledgements

For their involvement in helping me complete this work I would like to thank:

- My supervisors, Dr. Danie Els and Dr. Johan van der Spuy, for their continued faith in my abilities as well as their guidance, assistance and encouraging words,
- GEA Aircooled Systems and Howden Fan Equipment for their financial and technical support. In particular I would like to thank, Dr. Albert Zapke and Mr. Paul Barratt for their involvement as well as their technical and organisational support and Mr. Hans Heunis for his assistance and support on-site,
- Eskom for the opportunity to record measurements at a working facility and, in particular, Mr. Johnny Ballabio and Mr. Hein Goldschagg for their assistance during the implementation and measurement phases,
- Dr. Terry Terblanche for his tutelage and assistance regarding strain gauge measurements and data capturing systems,
- The personnel at the Mechanical and Mechatronic Engineering workshop for their assistance in manufacturing and their help with the laboratory tests. In particular I would like to thank Mr. Ferdi Zietsman for the many weekends spent on-site assisting with the strain gauge work.

Contents

List of Figures

Nomenclature

Symbols

A	-	Amplitude of vibration
d	-	Fan shaft diameter
D	-	Fan diameter
E	-	Modulus of elasticity
F	-	Force
G	-	Modulus of rigidity
H	-	Aerodynamic load
I	-	Moment of inertia
J	-	Polar moment of inertia
k	-	Gauge factor
L	-	Distance between strain gauges and applied force
M	-	Bending moment
N	-	Rotational speed
p	-	Pressure
P	-	Power
Q	-	Torque
R	-	Resistance
t	-	Time
T	-	Period of vibration
v	-	Air flow velocity
V	-	Voltage
y	-	Distance from centre of cantilevered beam
Y	-	Deflection

Greek symbols

α	-	Out-of-plane air flow angle
β	-	Off-axis air flow angle
δ	-	Logarithmic decrement
ϵ	-	Linear strain
γ	-	Shear strain
ρ	-	Density
ω	-	Vibrational frequency
Ω	-	Rotational frequency
ϕ	-	Phase shift
σ	-	Normal stress
θ	-	Flap-wise strain gauge angle
τ	-	Shear stress
ζ	-	Damping ratio

Subscripts

an	-	Anemometer
d	-	Dynamic
in	-	Input
m	-	Measurement
n	-	Natural frequency
out	-	Output
s	-	Static
t	-	Total
wt	-	Wind tunnel

Chapter 1

Introduction

1.1 Thermoelectric power generation and direct dry cooling

Electrical power can be generated in a variety of ways. In a steam turbine cycle water is boiled to produce steam which is then used to drive a turbine which generates electricity. This is known as a Rankine cycle and is depicted in Figure 1.1. When the steam has passed through the turbine, it is condensed in order to complete the cycle.

The low pressure turbine exhaust steam is condensed using either water or air as the coolant. Kröger (2004) states that in arid regions where there is little or no cooling water available, air-cooling is the only viable method of heat rejection and is known as dry-cooling. In direct cooled thermoelectric power plants where air is used as the cooling medium, mechanical draft air-cooled steam condensers (ACSCs) are often used to condense the low pressure steam. In this way no water is consumed in the cooling process

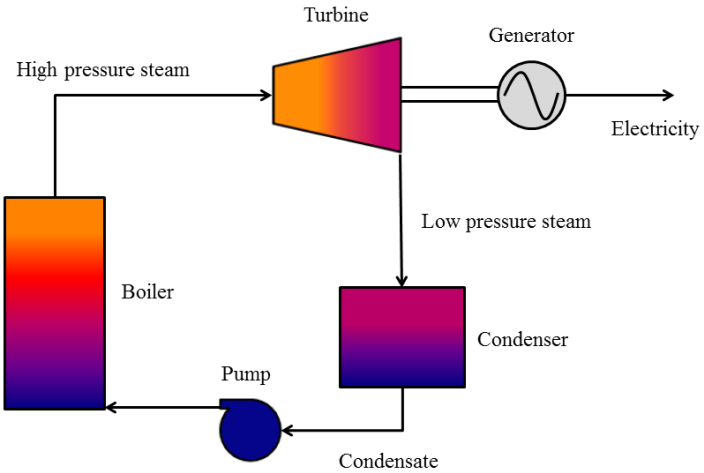

Figure 1.1: Rankine cycle

and the power plant's total fresh water consumption is much less than that of a plant employing wet-cooling. A photo of a full-scale ACSC is shown in Figure 1.2.

Figure 1.2: Photo of an ACSC

1.1.1 Description of the ACSC and fan units

There are many thermoelectric power plants in operation that use ACSCs. However, not all of these ACSCs operate in the exact same way and as such, the following description of an ACSC fan unit only applies to the power plant on which the current investigation is focused.

Low pressure turbine exhaust steam is ducted to steam headers which run along the top of a number of ACSC fan units where it is condensed in inclined finned tube heat exchanger bundles. Photos taken from above the ACSC, showing the steam ducts and heat exchangers, are presented in Figure 1.3.

(a) (b)

Figure 1.3: Photos of the ACSC steam ducts and heat exchangers

The fan units below the steam ducts are arranged in 48 rows of six. Each of the six turbine units then have eight rows of fans. Figure 1.4 is a diagram of a section of the facility as viewed from above. Each square in the matrix representing the ACSC depicts a single fan unit. Three of the six turbine units are shown as well as the location of the facility's weather mast. A photo taken from below the ACSC, showing some of the fan rows, is presented in Figure 1.5.

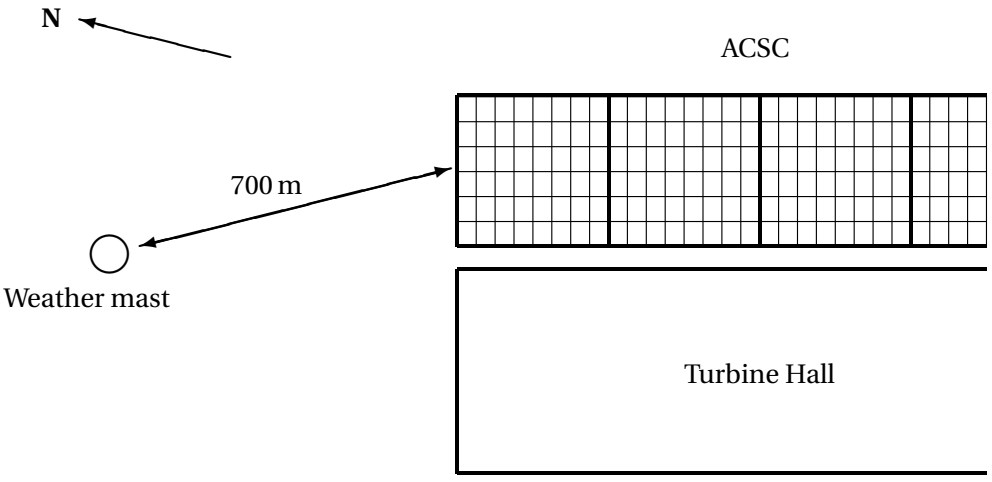

Figure 1.4: Diagram of ACSC with location of weather mast

Figure 1.5: Photo of ACSC fans from below

A diagram representing one of the fan units situated on the periphery of the ACSC is shown in Figure 1.6. Each ACSC fan unit consists of an axial flow fan that is located beneath, and blows air through inclined finned tube heat exchanger bundles. The inclination of the heat exchanger bundles maximizes the available heat transfer surface and is known as an A-frame configuration. Four of these inclined heat exchanger bundles are installed on either side of the fan. Steam condenses inside the finned tubes as a result of the heat transfer between the cooler ambient air being forced through the heat exchangers and the low pressure steam.

The area above the fan, which is enclosed by the heat exchanger bundles, is known as the plenum chamber. Inside the plenum chamber the fan is suspended from a bridge that serves as a walkway as well as a mounting point for the fan's motor and gearbox. The entire load of the fan rotor is suspended from the low speed shaft which extends out below the bridge. Below the fan, at the mouth of the inlet shroud surrounding it, is a screen made up of a grid constructed from thick wire placed over a support beam structure. This combination of wire grid and support beams is strong enough to support the weight of multiple workers when performing regular maintenance on the fan and can be seen in Figure 1.7.

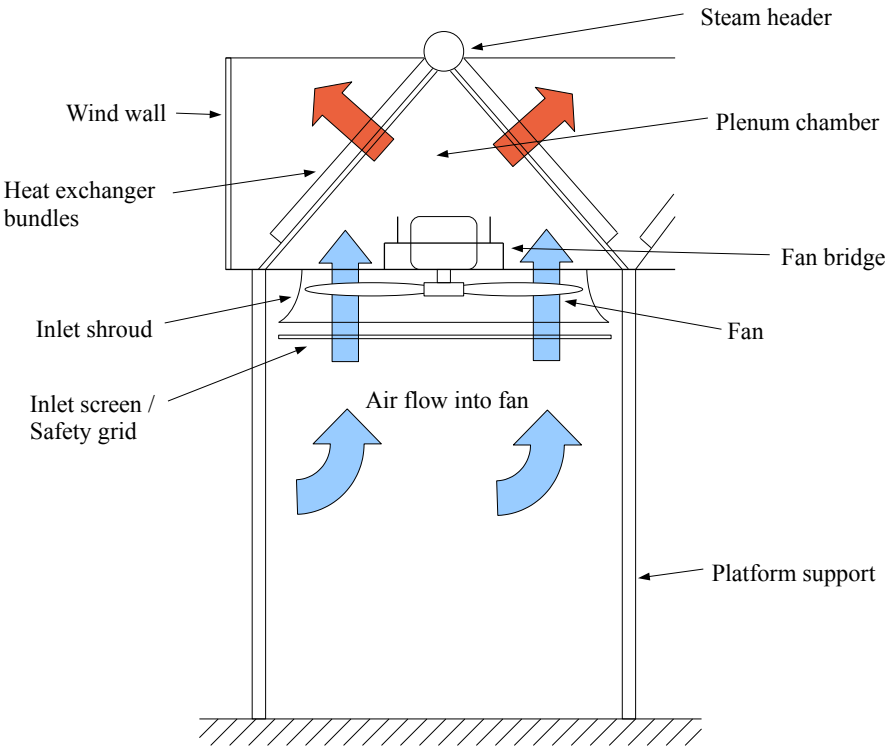

Figure 1.6: Typical ACSC fan unit

Figure 1.7: Safety grid located below fan

The fans used in the ACSC each have eight glass reinforced polyester (GRP) blades approximately 4.3 m long and 0.8 m wide. Each blade is attached to the fan's hub at its neck with two 30 mm diameter U-bolts and a set of saddles, shown in Figure 1.8. The fan blades are constructed in two halves which are bonded together to complete the blade. The exterior geometries, or skins, of the upper and lower surface are defined by using chopped strand mat and woven rovings whereas the load is transferred to the neck of the blade by means of unidirectional plies. These unidirectional plies are arranged in a fan-like pattern radiating out from the neck of the blade. In addition to this, two internal PVC foam webs are bonded to the upper and lower laminates along the full length of the blade.

Figure 1.8: Fan blade attachment to hub

1.2 Problem definition

As described in Section 1.1.1, the ACSC fan units at the power plant under investigation are placed in an array of hundreds of individual units. According to Thiart and Von Backström (1993) fans located in such an array can be subjected to distorted inflows due the presence of buildings, other fans and wind. Figure 1.9 schematically shows how the inner fans induce cross-flow in front of the fans located on the outer edges of the ACSC by drawing air in past them. This cross-flow, which is increased by unfavourable wind conditions, causes off-axis and maldistributed air flow into the fans. The distorted inflow conditions then result in varying pressure distributions on the fan blades as they rotate, which induces fluctuating mechanical loads on the blades and gearbox.

When a fan or any other form of rotating machine is being designed, the designer needs to account for any variable loading which might occur during operation of the machine. The actual loads experienced by an axial flow fan are not always available during the design phase. However, once the fan is in operation the loading on a rotating fan blade can be measured for a variety of inlet conditions. The data obtained from these

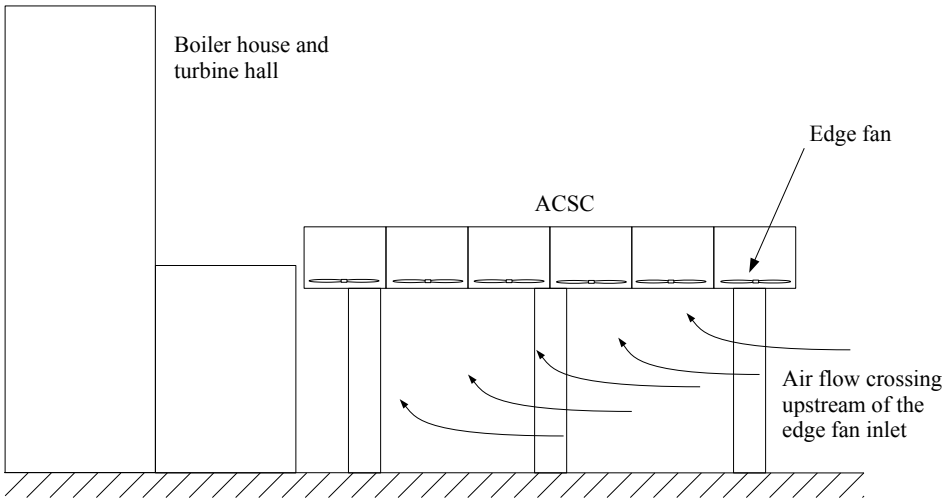

Figure 1.9: Air flow distribution underneath fan array

measurements can then be used to improve the blade design by considering the fatigue life of the blade due to the oscillating loads.

Moreover, the fan blades are not the only components of the system that experience variable loading on account of bad weather and distorted fan inlet air flow conditions. Vibration experienced by the fan rotor is transferred to the gearbox via the low-speed shaft where it causes fatigue in the shaft and internal components of the gearbox which could then lead to premature failures.

1.3 Objectives of the study

The primary objective of the study was to develop a measurement system that is able to measure, in real time, the ambient conditions and the effect thereof on inlet air flow and the loading exerted on the fan blades and gearbox. The measurements to be recorded were:

1. Ambient weather conditions
2. Loading at the blade neck as a function of the blade's position
3. Stresses and torque exerted on fan shaft
4. Inlet air flow velocity and temperature
5. Air flow at the heat exchanger outlet

Each of the sensors required for the project as well as the data capturing system needed to be specified, purchased and tested before the measurement system could be

installed at the full-scale facility. The purpose of the tests was to ensure that the correct equipment was being used and was functioning as required. Preliminary testing could also be used to test the hardware limitations, which would improve the confidence in, and reliability of the measurements being recorded.

In addition to recording the measurements, the captured data needed to be processed and analysed for any important trends. The primary goal of the data analysis was to identify any relationships between the loading data and the inlet air flow conditions. Also, information regarding the blade and shaft loading amplitudes during the fan's rotation could be used to perform fatigue calculations for the blades and gearbox at a later stage.

1.4 Literature survey

In order to ascertain the current level of knowledge within the field of the investigation, it was important to study the available literature regarding the subject at hand. This section aims to provide an overview of the literature available and also point out the necessity of the current investigation.

1.4.1 The effect of distorted inflow on an axial flow fan

Significant amounts of experimental as well as numerical work have been performed to analyse the effect of cross-flow at the fan inlet on the performance of an ACSC. Salta and Kröger (1995) performed experiments on a multiple fan arrangement to determine the effect of varying the distance between the platform and the ground level as well as changing the width of the walkway. They measured flow rates through the individual fans and found that the fans situated along the edge of the multiple fan arrangement are most affected by the distorted inlet air flow pattern. However, this investigation only considered the two-dimensional flow scenario of an infinitely long ACSC in windless conditions.

Duvenhage *et al.* (1996) continued Salta and Kröger's research by determining, both numerically and experimentally, the effect that varying platform heights as well as different types of inlet shrouds has on fan performance within a multiple fan arrangement. They found that bell-mouth or conical inlet shrouds offer lower inlet losses than a cylindrical inlet.

Stinnes (1998) performed more experimental work on a standard test facility designed by Venter (1990). Off-axis flow was induced at the inlet of an axial flow fan by guiding the air through a pipe with centreline at a specific angle relative to the axial direction fan. He recorded detailed measurements of the flow fields in up- and downstream of the fan and concluded that the power requirement of the fans remain largely unchanged irrespective of the cross-flow magnitude. Stinnes and Von Backström (2002) later reported that the fan total-to-total pressure rise is independent of off-axis inflow angles up to 27°.

Thiart and Von Backström (1993) reported that the flow field near an axial fan with distorted inflow conditions induces a maldistribution of thrust along the fan blades. The fan was modeled using an actuator disc which uses the lift and drag characteristics of the blade to determine the forces exerted on the flow. The numerical results obtained were compared to experimental data generated by Thiart (1990). It was found that the

numerical and experimental results correlate well, but that the numerical model underestimates the increase in shaft power.

Using a similar model to the one used by Thiart and Von Backström (1993), Meyer and Kröger (2001) investigated the effect of adding an annular exit to an axial flow fan, which they compared to experimental data. The most important of these results is that the numerically determined velocity profiles up- and downstream of the fan predicted the experimental results accurately.

The current methods of modelling axial flow fans, namely the actuator disc and the pressure jump method, which uses the static pressure increase given by the standard fan curves, were investigated by Van der Spuy *et al.* (2009). They found that the actuator disc model underestimates the fan static pressure at low flow rates.

Meyer (2005) extended the work done by Duvenhage *et al.* (1996) to two and four rows of fans and found that the inlet flow losses experienced by the first two rows of fans are dominated by the separation of flow around the fan inlet. It was also concluded that the second row of fans experiences very little separation but that the inlet flow losses are instead dominated by cross-flow into the fan.

Bredell *et al.* (2006*b*) used the actuator disc to model a section of an ACSC consisting of six fans. The effect of using fans with different hub-tip ratios was investigated and it was found that a fan with a higher hub-tip ratio is less sensitive to inlet flow distortions. It was also concluded that fans with low hub-tip ratios are prone to recirculation or backflow near the hub.

Hotchkiss *et al.* (2006) developed a numerical fan model, based on the one used by Meyer and Kröger (2001), capable of simulating off-axis inflow conditions. The numerical results were compared to the experimental findings of Stinnes (1998) to validate the model. It was found that static pressure rise across an axial flow fan is adversely affected by the presence of cross-flow at the fan inlet.

1.4.2 The effect of wind on the performance of an ACSC

A study regarding the performance of the ACSC under windy conditions was completed by Van Rooyen (2007) where the effect wind has on fans located at different positions within the array was investigated. It was discovered that the fans situated on the edges of the array experience the greatest drop in volumetric effectiveness whereas the other fans remain largely unaffected. Figure 1.10 shows the static pressure distribution at an ACSC edge fan where it is clear that a rotating fan blade will experience large pressure variations. It can be assumed that blade loading is proportional to static pressure rise over the fan and as such the blade will experience a variation in loading as a function of its rotational position.

1.4.3 Fan blade loading and vibration

Even though numerous numerical studies have been completed regarding the performance of axial flow fans under distorted inflow conditions, little has been done to investigate the aerodynamic loading exerted on an axial flow fan blade. Bredell *et al.* (2006*a*), again using the actuator disc model, investigated the bending moments exerted on fan blades under distorted inflow conditions. It was found that, in general, fans experience higher bending moments on the windward side. It was also discovered that separation

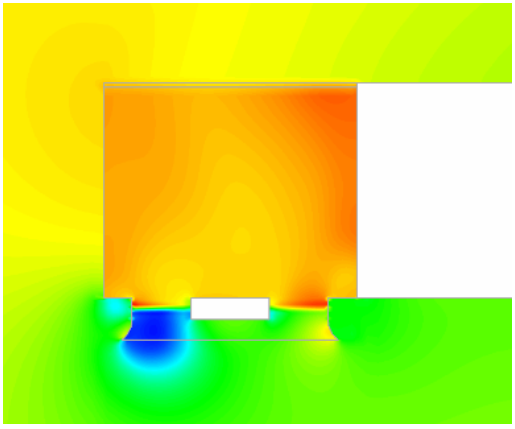

Figure 1.10: Static pressure distribution at ACSC edge fan as described by Van Rooyen (2007)

is more likely to occur on the this side of the fan. These conclusions serve to further validate the hypothesis that fan blades experience increased loading under windy conditions when cross-flow is increased.

Xu *et al.* (2004) performed tests on an axial flow fan of 1.829 m diameter, documenting the unsteady pressure distribution on the fan blade during start-up. The results obtained showed that the flow field produced by an axial fan is not completely steady. Even when the fan was running at a constant speed there was a variation in the blade static pressure distribution. However, the frequency of this variation was much smaller than the rotational frequency of the fan. They also fitted the blade with several strain gauges and compared the measurements to results obtained through a Finite Element Method (FEM) simulation.

Van der Spek (2003) describes the different vibrational modes of an ACSC fan unit installation and proposes a way in which to reduce vibration by means of an attachment to the tip of each fan blade. The proposed attachment is called the Aerotip and reduces the pressure pulses exerted on the fan casing which in turn reduces the vibrations of the surrounding structure while simultaneously improving the efficiency of the fan.

1.4.4 Contribution of the current investigation

As shown in this literature survey, there is no shortage of information available regarding the numerical simulation of ACSCs and the axial flow fans located therein. Numerical simulations provide valuable insight regarding the air flow distribution at the fan inlet and the fan performance under windy conditions. However, experimental work is often used to verify numerical solutions and as such there is always a need for empirical data.

Numerous researchers have performed experiments on fans installed in test facilities. However, less work has been done on full-scale fans installed in working ACSCs. Van Aarde (1990) measured the air flow at the inlet and outlet of the fan installed at the same full-scale facility as the one used for the current investigation. However, he did not couple his measurements to any mechanical loading on the fan blades or gearbox. Also, he took measurements at different locations within the ACSC over a period of four days for approximately an hour each day. These measurement times are not sufficiently

long enough to be able to draw conclusions regarding the relationship between ambient conditions and fan performance parameters.

The current investigation aims to provide an abundance of measured data regarding air flow and mechanical loading for use in future numerical simulations and system designs. In addition to this, the system being designed and hardware used will also be usable at other installations for similar investigations in the future.

1.5 Measurement state of the art

Current measurement techniques and apparatus were researched in order to decide which systems would be most suited to the project being undertaken. Strain gauge measurements are accepted as the standard manner in which to collect mechanical loading data and as such were to be used for the measurements on the fan blade and shaft. However, it was unclear which sensors would be best suited to measure air flow and the blade's rotational position. Air flow velocity is usually measured with anemometers, but there are many different types of anemometers and research needed to be conducted to determine which type would be best suited to the current application.

1.5.1 Strain gauge measurements, configurations and calibration

Strain gauges are a type of electrical resistor used to measure the deformation of any structure to which it is attached. As the structure deforms, so does the strain gauge and as a result its resistance changes based on the magnitude of the deformation and whether the structure undergoes compression or elongation. The change in resistance of the strain gauge is measured indirectly as a change in voltage by connecting the strain gauges in a Wheatstone bridge configuration. Such a configuration is shown in Figure 1.11. When all four strain gauges have the same resistance value, the bridge is said to be balanced and the output voltage, V_{out}, is equal to zero. This output voltage then changes with changes in the resistance of the strain gauges.

It can be shown that the equation relating the output (sensor) and input (excitation) voltages as a function of the change in each strain gauge resistance value is given by

$$\frac{\Delta V_{out}}{V_{in}} = \frac{1}{4}\left(\frac{\Delta R_1}{R_1} - \frac{\Delta R_2}{R_2} + \frac{\Delta R_3}{R_3} - \frac{\Delta R_4}{R_4}\right) \tag{1.1}$$

With the gauge factor, k, and linear strain, ϵ, the strain gauge equation is given by

$$\frac{\Delta R}{R} = k\epsilon \tag{1.2}$$

This can then be substituted into equation 1.1 to obtain the following

$$\frac{\Delta V_{out}}{V_{in}} = \frac{k}{4}(\epsilon_1 - \epsilon_2 + \epsilon_3 - \epsilon_4) \tag{1.3}$$

By using the properties of the Wheatstone bridge strain gauge equation, one can place the four strain gauges making up a full bridge configuration in such a way that it eliminates certain modes of deformation. This is particularly useful when wanting to measure bending and axial strains separately. When the fan is spinning, each blade will

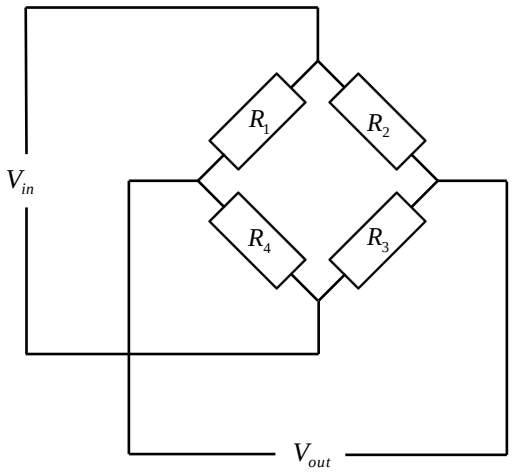

Figure 1.11: Wheatstone bridge configuration for strain gauges

be subjected to centrifugal loads which will exert an axial force on the blade. However, this axial strain is not related to the cyclical loading caused by distorted inlet flow conditions and as such does not have to be measured. By attaching strain gauges R_1 and R_3 on one side of the blade and strain gauges R_2 and R_4 on the other, the axial component of the strain will be canceled out in equation 1.3. As a result one is able to obtain the average value of the bending strain measured by the four strain gauges. This strain gauge configuration is shown in Figure 1.12a. Note that bending strain can also be measured using a half bridge configuration where only 2 strain gauges are required. However, half bridges were not used because the data capturing system (described in Section 2) was configured to work with full bridge strain gauge configurations.

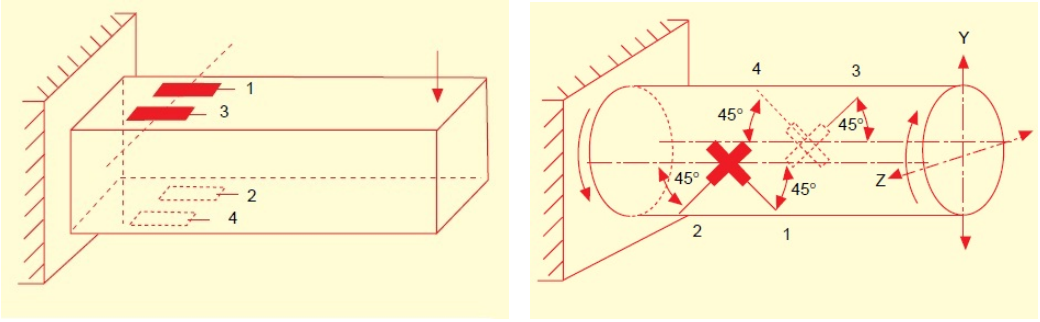

(a) Bending (b) Torsion

Figure 1.12: Full-bridge strain gauge configurations as described by Omega

Torsional strain is also measured by means of a full-bridge strain gauge configuration. The configuration for measuring torsional strain is shown in Figure 1.12b. These

strain gauges are attached at an angle of 45° with the axis of the blade neck. This particular configuration also compensates for temperature loads as well as axial and bending strain. The relationship between shear strain, γ, and the measured strain, $\epsilon_{45°}$, is given by equation 1.4 where

$$\gamma = 2 \times \epsilon_{45°} \tag{1.4}$$

Calibration of a set of strain gauges configured in a Wheatstone bridge is commonly performed using shunt resistors. When a strain gauge undergoes a deformation, there is a change in resistance. By using equation 1.2 and a gauge factor of $k = 2$, it can be shown that for a 350 Ω strain gauge a strain of 1000 μm/m yields the following change in resistance

$$\begin{aligned} \Delta R &= Rk\epsilon \\ &= 350 \times 2 \times 1000 \times 10^{-6} \\ &= 0.7\,\Omega \end{aligned} \tag{1.5}$$

Inversely then, changing the resistance from 350 Ω to 350.7 Ω will have the same result as applying a strain of 1000 μm/m to the strain gauge. However, it is impractical to add a 0.7 Ω resistor in series with the strain gauge and as such it is simpler to simulate a negative strain by connecting a resistor in parallel with the strain gauge. This reduces the effective resistance to 349.3 Ω and is known as shunt resistor calibration. When connected, the shunt resistor can be used to correctly scale the output of the bridge amplifier by making temporary adjustments to the strain gauge factor, k. During calibration the output should also be balanced to a zero reading when zero load is applied.

1.5.2 Air flow sensors

Air flow velocity is commonly measured using an anemometer. However, numerous types of anemometers well as other alternatives needed to be researched.

Propeller anemometer A propeller-type anemometer consists of a propeller attached to a tacho-generator that generates a voltage output based on the rotational speed of the propeller. Figure 1.13a shows a 3-axis anemometer consisting of three orthogonally mounted propeller anemometers. Van Aarde (1990) used propeller-type anemometers to measure the inlet flow field below a fan at the same facility as used for this project. He attached the anemometers to a beam situated below the fan on top of the safety grid. The beam was then rotated through an angle of 360° with a stepper motor and as such gave an indication of the entire inlet flow field under steady operating conditions.

(a) 3-axis propeller

(b) 2-axis ultrasonic

(c) 3-axis ultrasonic

Figure 1.13: Anemometer types

Pressure probe An alternative to the use of an anemometer is a pressure probe. A pressure probe, also known as a Pitot tube, measures the difference in total and static pressure to determine the air flow velocity. The total pressure, p_t, is measured at the tip, or the stagnation point, of the probe and the static pressure, p_s, at one or more holes on the wall of the instrument. Equation 1.6 shows how the air flow velocity, v, is calculated using these two values and the density, ρ, of air. Figure 1.14 shows the probe used by Pierce (2008) during his experiments conducted in a wind tunnel on wind turbine blades.

$$\begin{aligned} p_t &= p_s + p_d \\ &= p_s + \frac{1}{2}\rho v^2 \end{aligned} \tag{1.6}$$

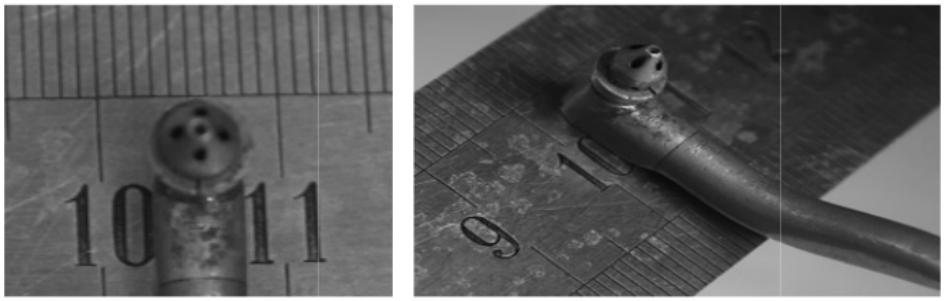

Figure 1.14: 5-Hole pressure probe used by Pierce (2008)

Similar to work done by Venter (1990), Stinnes (1998) used a 5-hole pressure probe to measure the air flow conditions directly up- and downstream of an axial flow fan. He moved the probe to various locations in the radial and circumferential directions and

recorded steady-state measurements. A pressure probe is a good alternative to a propeller anemometer because it provides data regarding the flow velocity as well as its direction. However, the problem with a pressure probe is that it can only measure accurately within approximately 40° of its main axis. Consequently, the pressure probe cannot measure highly distorted flow or reverse flow from the fan. A second concern regarding the use of pressure probes is their generally low response time. The holes on the tip of a pressure probe are usually connected to a pressure transducer with plastic pipes. For the pressure transducer to register a change in direction or velocity, the entire column of air in the tube has to respond to the change, thus giving the instrument a relatively slow response time. Alternatively, one can place the pressure transducers in the tip of the probe, but this would require transducers that are very small and subsequently, very expensive. Such a fast-response probe, supplied by Aeroprobe Corporation, is shown in Figure 1.15.

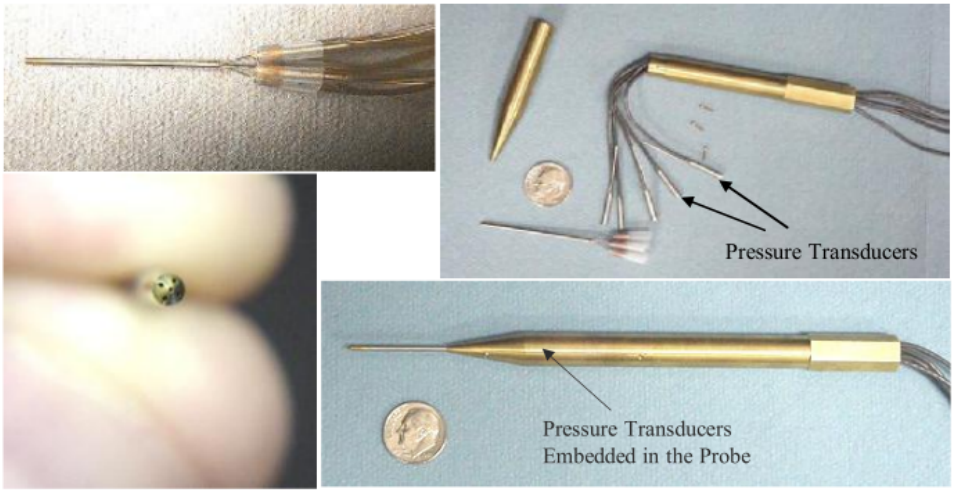

Figure 1.15: Aerospace Corporation fast-response pressure probe

Ultrasonic anemometer Ultrasonic anemometers measure air flow by relaying ultrasonic pulses between probes and then, by using the time of flight of the pulses, the air flow velocity and direction can be calculated. The main advantage of ultrasonic anemometers is that they have a much lower response time than propeller-type anemometers. They can generally measure in the range of 0.25 Hz to 20 Hz, which makes them ideal for measuring the transient flow conditions required for this investigation. Ultrasonic anemometers are configured to either measure flow in 2 or 3 directions, shown in Figure 1.13b and Figure 1.13c, respectively.

The 2-axis ultrasonic anemometer, as depicted in Figure 1.13b measures the wind velocity and direction in a plane which is perpendicular to its mounting axis. Tests, similar to those conducted by Wauben (2005), were performed in a wind tunnel to determine the measurement limits of the anemometer when subjected to out-of-plane flow and are presented in Section 3.1.

1.5.3 Fan blade position sensors

In order to analyse the strain gauge data and correlate it with any airflow measurements it is desirable to know the location of the blade at all times during its rotation.

Laser distance sensor A laser distance sensor uses a laser beam to determine the distance of objects. It calculates the distance of an object based on the time taken for a pulse that is sent towards the object, to be reflected back. Figure 1.16a shows an industrial laser distance sensor manufactured by Leuze electronic. The sensor would be placed, pointing upward, below the fan on the safety grid where it would measure the distance between itself and each fan blade as it passes by. Every time a blade passes the sensor, the distance being measured would be significantly lower than what is measured otherwise. These lower distance measurements would then provide a time-based signal which can be used to interpolate the rotational position of each fan blade. However, one needs to consider the fact that there are eight blades passing the sensor. As such, determining which blade's position is being measured becomes a challenge.

Camera An alternative to the laser distance sensor would be to attach a small camera to the hub of the fan. The camera would be pointing directly down the span of the blade towards the fan casing. The Point Grey Grasshopper high speed camera is shown in Figure 1.16b along with its primary dimensions. Markings on the casing would indicate the fan blade's position as well as an indication of its tip deflection. However, the problem with using a camera is that very large amounts of data would need to be stored if images are to be captured at a high enough rate. Also, the output from the camera would need to be analysed, frame by frame, to determine the values being sought. Software can be written or purchased to do this, but it adds an unwanted, and perhaps unnecessary, additional layer of complexity to the system.

(a) Leuze optical distance sensor

(b) Point Grey Grasshopper camera

Figure 1.16: Fan blade position sensors

Hall-effect proximity sensor The simplest way to determine the blade's location is by using a Hall-Effect proximity sensor placed close to the low-speed shaft. This sensor provides a voltage output relative to the proximity of a metal object caused by the changes in the magnetic field. The only concern with such a proximity sensor is that the object creating the impulse needs to pass by the sensor with a clearance of a few millimetres at most. If there are any large vibrations in the system the sensor could end up making contact with the passing object.

1.6 Fan unit selection and directional convention

Before the installation of the measurement equipment, a decision needed to be made regarding which fan to monitor. There were practical implications to consider as well as the predominant air flow direction at the selected fan. Firstly, from a practical point of view all the fan rotors are identical. However, two different types of gearboxes are installed at the facility: Flender and Hansen. The low-speed shaft connecting a Flender gearbox to its fan rotor is shown in Figure 1.17. One can see that it would be impossible to attach strain gauges to the shaft because it is unexposed. As a result, a fan unit with a Hansen gearbox, which has an exposed low-speed shaft, had to be selected.

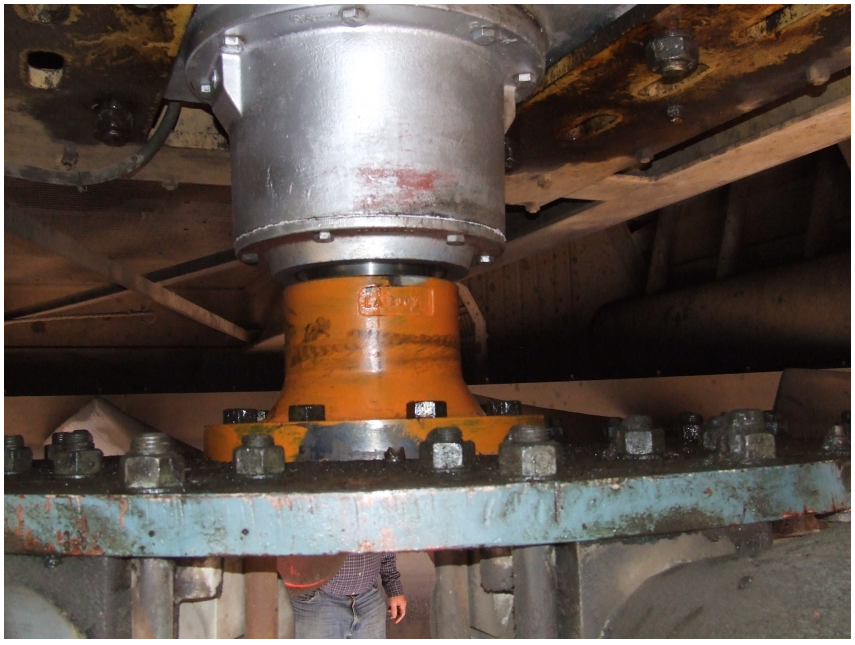

Figure 1.17: Low-speed shaft of a Flender gearbox

The second factor influencing the decision of which fan to use is the effect that its position within the ACSC has on the predominant direction of air flow entering the fan. For the purpose of this project it was required that a fan situated on the periphery of the ACSC be used. The reason for this was that the edge fans often experience greater blade loading conditions than the inner fans due to increased cross-flow, as explained in Section 1.2.

Figure 1.18 shows a top view of the ACSC with the position of the selected fan as well as the North direction and the directional axes which will be referred to in this document. Similarly to the description offered in Section 1.1.1, each open square of the grid representing the ACSC is a single fan unit while the blackened square indicates which fan was selected to be monitored. The x-axis is parallel to the longitudinal axis of the ACSC while the z-axis is parallel to the lateral axis and extends from the outer walkway to the turbine hall. With these directional axes fixed, the y-axis points upwards, out of the page. Fans situated near the longitudinal center (the edge between unit 3 and unit 4) of the ACSC experience more stable flow conditions than those on the edges (fans in unit 1 and unit 6) because the flow at the inlet of these fans are mostly two-dimensional in the y- and z-directions. It is as a result of these two-dimensional flow conditions that the specific fan was selected. Measurements of a two-dimensional flow field would be easier to obtain and simpler to interpret than if the flow field was three-dimensional.

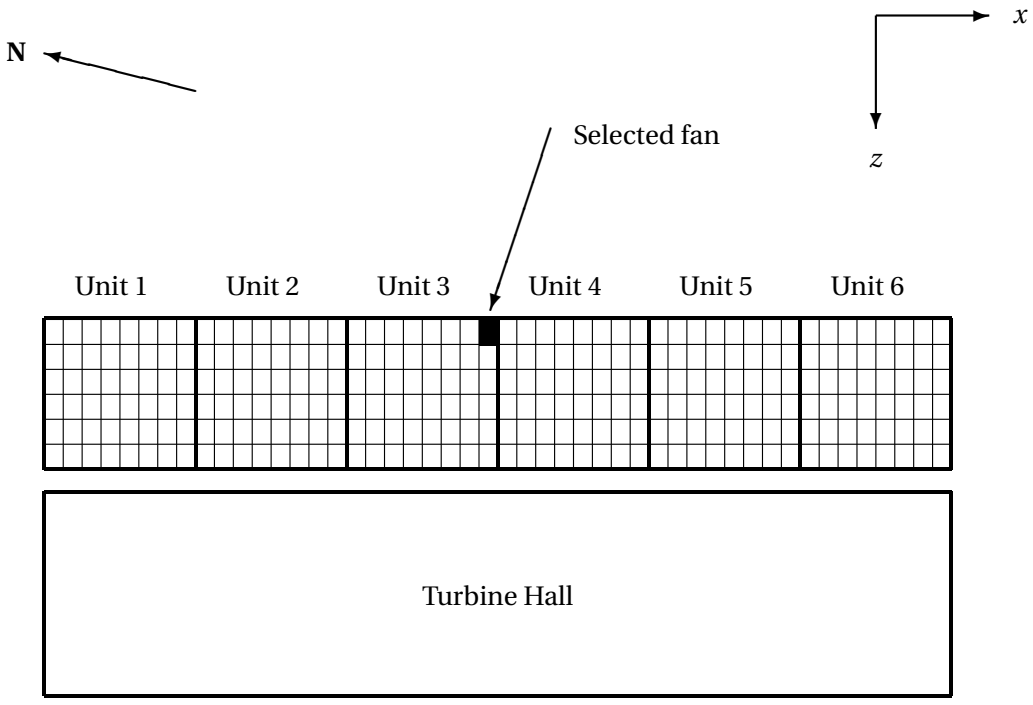

Figure 1.18: Fan unit selection within ACSC

Chapter 2

Data capturing system

An important part of the measurement system being developed is the manner in which data will be captured from the various sensors. Difficulties are brought about not only by the sheer amount of sensors that need to be sampled from, but also by the fact that measurements need to be taken on the rotating fan.

Figure 2.1 shows an overview of the data capturing system configuration. The diagram describes how the measurement devices on the rotating fan and the devices placed at the fan inlet and bundle outlet are connected to the data capturing system. The data capturing system has been divided into three parts: wireless data capturing, wired data capturing and data synchronisation and recording. Wireless data capturing refers to the measurements taken from the rotating fan assembly while wired data capturing includes all of the measurements taken from stationary devices at the fan inlet and bundle outlet. Each of the components shown in the diagram are discussed in the following sections.

2.1 Wireless data capturing

Traditionally, data has been recorded from rotating machinery by means of slip-rings. A slip-ring is an electrical connection between a rotating assembly and a stationary data capturing unit. It works by maintaining contact between stationary brushes and rings on the rotating assembly. However, it was decided that slip-rings would not be feasible for the project due to the large diameter of the fan shaft and the possibility of noise in the recorded data due to the harsh environment that the slip-rings would be operating in.

A decision was therefore made to either have two separate measurement systems for the rotating assembly and the stationary sensors or to have a wireless system transmitting to a receiver that could be incorporated with the rest of the data recording hardware. The main concern regarding the use of two separate systems was the synchronisation of the measurements taken on the fan and the measurements from the stationary sensors. Measurements can be manually synchronised after recording by using the time-stamp from each data point, but this would introduce an added layer of complexity and uncertainty in the system. As such it was decided to use a wireless system that could be attached to the fan along with the relevant sensors and that could easily be incorporated into the data capturing hardware to be used with the stationary sensors.

The selected system was the MicroStrain V-Link wireless voltage node, shown in Figure 2.2a. These units each have four fully-differential strain gauge channels, which can

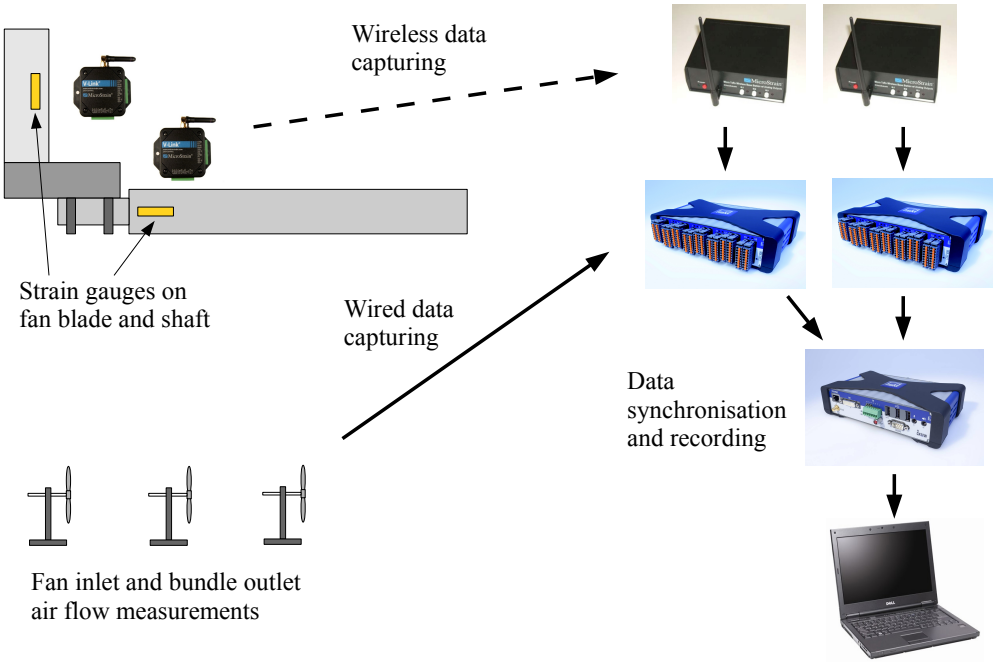

Figure 2.1: Data capturing system overview

be set up for either quarter-, half- or full-bridge strain gauge configurations and sample at a minimum rate of 565 Hz if all 4 channels are active. These wireless amplifiers have a bridge excitation voltage of 3 V which is low enough to not cause any significant heating effects when used with 350 Ω strain gauges. However, the most attractive feature of the V-Link system is that each unit streams data to a base station which converts the signal to an analogue output between 0 V and 5 V. This makes the system easy to use with data capturing devices already recording analogue signals from other sources. The analogue base station can be seen in Figure 2.2b.

(a) V-Link wireless voltage node (b) Analogue base station

Figure 2.2: MicroStrain V-Link system

As well as having an analogue output channel for each of the 4 strain gauge bridges connected to the V-Link, the base station can also be connected to a PC via a USB connection. The Node Commander software can be used to initiate streaming on each node and calibrate strain gauge channels. Each V-Link works by converting the voltage signal over the strain gauge bridge to a 12 bit digital signal. The signal is then transmitted to the base station where it is converted to an analogue voltage signal or transferred to a PC via the USB connection.

The strain gauge calibration function in the Node Commander software provides the user with coefficients for a relationship between the signal from the V-Link, which is a 0 - 4096 bit signal, to a strain reading in μm/m. The 0 -5 V analog output on the base station is directly related to the digital 0 -4096 bit signal and as such the strain can be determined from the voltage reading with the strain calibration coefficients.

To provide the capacity for the 6 strain gauge channels that were planned, 3 V-Link units had to be used. Each V-Link was attached to the fan hub by 2 4 mm screws. This method of attachment required holes to be drilled and tapped into the fan hub for the screws and is shown in Figure 2.3. By attaching the V-Link units to the hub, close to the shaft, the centrifugal load exerted on the hardware is greatly reduced and ensures that the system does not get damaged.

One shortcoming of the MicroStrain system was that the internal batteries of a V-Link could only sustain approximately 10 h of continuous streaming. This meant that the units had to be charged from a 220 V power source on a daily basis. The charging cables were dropped down through holes in the gearbox mounting plate every morning after the fan was switched off and the batteries were charged for approximately three to four hours.

Figure 2.3: MicroStrain V-Link units attached to fan hub

2.2 Wired data capturing

In addition to the measurements being recorded by the wireless system attached to the fan hub, an array of sensors was placed at the fan inlet on top of the safety grid as well as at the outlet of the heat exchanger bundles. All of these sensors were connected to the data capturing system with shielded cabling and required hardware with a large number of channels which could be recorded simultaneously.

After it was decided which sensors were to be used it was found that the data capturing system required a total of 31 measurement channels. Six of these channels were from the two V-Link units while the rest were occupied by the array of stationary sensors. Fortunately, most of the channels would simply need to record analogue voltages or currents from the V-Link base stations and other sensors and as such there was no need for a complicated data capturing system with the capacity to record data from a large variety of signal sources. This simplicity allowed the specification of a data recording system with a very low cost per channel, which in turn granted the capacity to simultaneously measure from most of the sensors.

Due to previous experience with similar hardware and adherence to the requirements of the planned data capturing system, the decision was made to use 2 HBM QuantumX MX1601 units. Each of these units has 16, individually configurable, channels for voltage and current signals and also has the capacity to provide power to the various sensors attached to it. The two units together then provided the required amount of channels at a maximum sampling rate of 19.2 kHz which equates to 1.2 kHz with all 16 channels active. The MX1601 device is shown in Figure 2.4a.

(a) HBM QuantumX MX1601 (b) HBM QuantumX Data Recorder CX22W

Figure 2.4: HBM QuantumX data capturing hardware

2.3 Data synchronization and recording

Even though each MX1601 is capable of recording its own data, a problem arises when there is a requirement for the data from both units to be accurately synchronised. The data could be manually synchronised using the time stamp from each reading, but at a recording rate as high as 150 Hz and no way to correlate the starting time of each unit this was not a valid option. As a result of this difficulty it was decided to use the HBM

QuantumX CX22W to not only synchronise the data, but to also record it and power the 2 MX1601 units.

The CX22W, shown in Figure 2.4b, was connected to the 2 MX1601 units via FireWire which is used for data transfer as well as power supply. The CX22W has an embedded Windows operating system and can be implemented in a number of ways. Originally, the unit was to be used with a monitor, mouse and keyboard and would serve the same purpose as a PC. The other QuantumX units would transfer data to the CX22W where the bundled HBM Catman AP software would be used for real-time graphing and data recording. However, at the full-scale facility, it was discovered that it would be better to make use of the wireless capabilities of the CX22W to enable a remote desktop connection from a laptop. The reason for this was that it was too windy inside the plenum chamber to safely use an LCD screen. There was also no suitable surface for using a mouse. Consequently, it was better to use a laptop from the walkway outside the plenum chamber or from a vehicle parked below the ACSC.

As mentioned previously, the CX22W came with Catman AP installed, which greatly offsets the cost of the system, making it a very attractive solution. In order to make use of the remote desktop capabilities from a laptop the QuantumX Data Recorder Assistant software had to be installed. This package enables the remote desktop connection once the laptop is connected to the wireless network created by the CX22W.

2.4 Placement and protection of data recording hardware

In order to maintain a good signal, the V-Link base stations had to be placed within the plenum chamber. The best place to put them was on top of the fan bridge where they had a clear line-of-sight with the V-Link units attached to the fan hub. The base stations were able to receive data from the wireless units while initially placed outside the plenum chamber on the walkway, but some signal loss was occasionally observed and the decision to move them inside was made.

The 2 V-Link base stations, along with the three QuantumX units were placed inside a metal container which was closed and secured with padlocks at night to protect it from theft, tampering and the elements. Power was routed to the devices in the container from one of the many 220 V sockets positioned along the walkway through a gap in the stairs leading up to the entrance to the plenum chamber. Figure 2.5a shows the positioning of the metal case on the fan bridge and Figure 2.5b shows the data capturing hardware stored inside the case.

(a) Data capturing hardware case on fan bridge

(b) Base stations and QuantumX units inside metal case

Figure 2.5: Storage container for data capturing hardware

Chapter 3

Sensor testing and verification

In order to confirm the measurement system's capabilities and functionality each component needed to be tested individually in a laboratory environment before commissioning. Testing of components before installation at the full-scale facility enabled the pre-emptive solving of any possible problems as well as increasing familiarity with the system. This resulted in increased confidence in the measurements as well as quicker installation at the full-scale facility.

3.1 Ultrasonic anemometer testing

The primary concern regarding the measurement capabilities of the ultrasonic anemometers is when the flow being measured has a component in the out-of-plane direction. Tests conducted by Wauben (2005) showed that ultrasonic anemometers from three different manufacturers, including Gill, compare very well to the more traditional cup anemometer measurements. The anemometers were tested with various in-plane flow angles and velocities. However, the out-of-plane measurement limits of the anemometers were not investigated. Figure 3.1a shows the situation where the flow is in the plane of measurement and Figure 3.1b depicts the situation where the flow makes an angle of α with the plane of measurement.

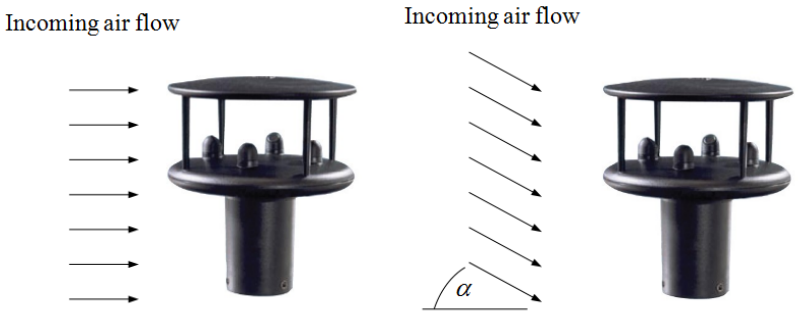

(a) In-plane flow (b) Out-of-plane flow

Figure 3.1: Ultrasonic anemometer air flow angles

When propeller anemometers experience off-axis flow, they generally measure only the component in the direction of their axis. The assumption is that a similar rule should apply to the ultrasonic anemometers where the flow magnitude is adjusted by the cosine of the angle it makes with the plane of measurement. This relationship is given in equation 3.1 where v is the flow magnitude and v_m is what is measured by the anemometer. However, this would need to be tested in a wind tunnel for various flow angles and magnitudes.

$$v_m = v \cos \alpha \tag{3.1}$$

3.1.1 Test setup and procedure

To test the output from the ultrasonic anemometers at different out-of-plane flow angles, the induced draft tunnel at the University of Stellenbosch was used. The tunnel, shown in Figure 3.2, has a centrifugal flow fan that draws air in through a rounded inlet section. Kröger (2004) describes how the air flow is determined by measuring the pressure drop across the elliptical nozzle in the wind tunnel.

During the test the anemometer was placed at the wind tunnel inlet where it was mounted within a section of steel tubing which had been welded to a piece of steel plate. This was then bolted to a second piece of steel, which was mounted in a vice. The bolted connection could be loosened and rotated to simulate any air flow angle. Figure 3.3 shows the anemometer and its bracket as it was mounted at the wind tunnel inlet.

The test was conducted by setting the anemometer at a specific angle and changing the fan's rotational speed with a variable-speed drive (VSD). For each air flow angle the electric motor was set to 10 different speeds between 5 Hz and 50 Hz. The test was repeated for flow angles increasing from 0° to 70°.

Figure 3.2: Induced draft wind tunnel used for anemometer tests

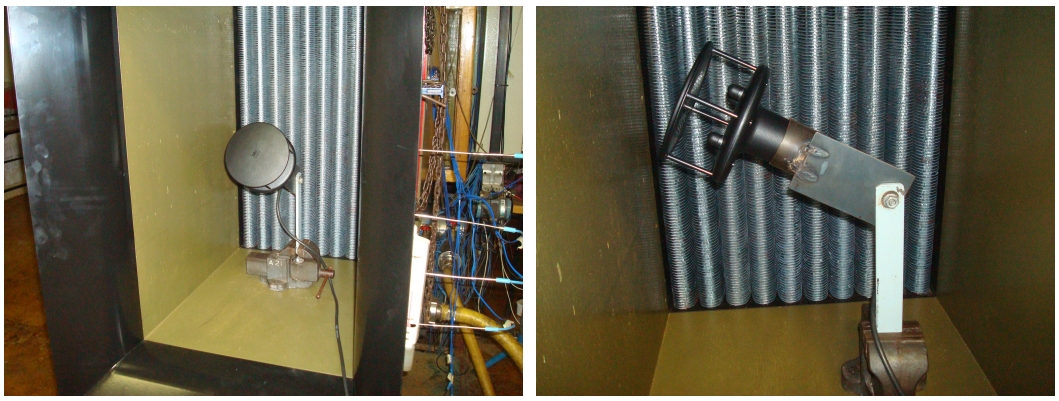

(a) Anemometer in wind tunnel (b) Anemometer bracket as seen from the side

Figure 3.3: Ultrasonic anemometer placement within wind tunnel

3.1.2 Results

The test results are split into two sections, namely the accuracy of the anemometer readings and its measurement capabilities for air flow at out-of-plane angles. The accuracy of the anemometer was tested by setting the anemometer to simulate an air flow angle of 0° and comparing its measurement to the calculated flow velocity for the tunnel. By means of an approximate calculation, it can be assumed that the anemometer occupies 5% of the inlet area. The calculated and measured air flow values correlate very well and have a maximum error of approximately 5%. Figure 3.4 shows the results of the test to determine the accuracy of the anemometer where it is set at a flow angle of 0°. The flow rate measured by the anemometer, v_m, is plotted against the calculated wind tunnel air flow velocity, v_{wt}, which is modified to incorporate the out-of-plane air flow angle, α.

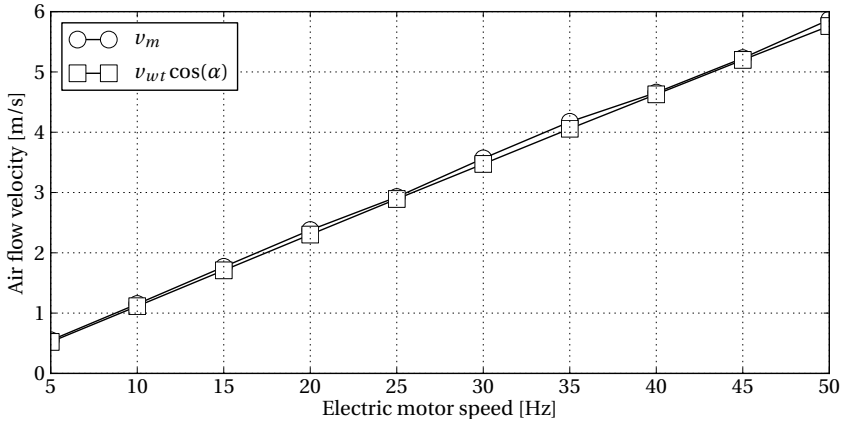

Figure 3.4: Ultrasonic anemometer accuracy test results

As the flow angle was increased by rotating the anemometer, it was found that it was able to measure well within 40° of its plane of measurement. However, at a flow angle of approximately 50° the measurements taken by the anemometer would be much lower

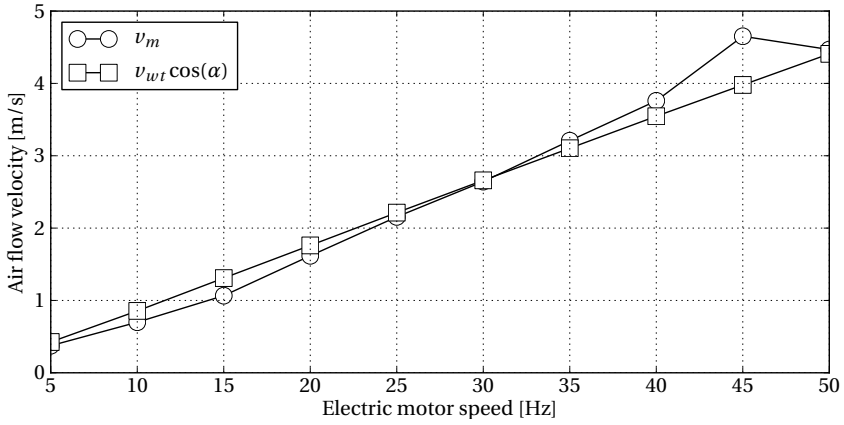

(a) Results for $\alpha = 40°$

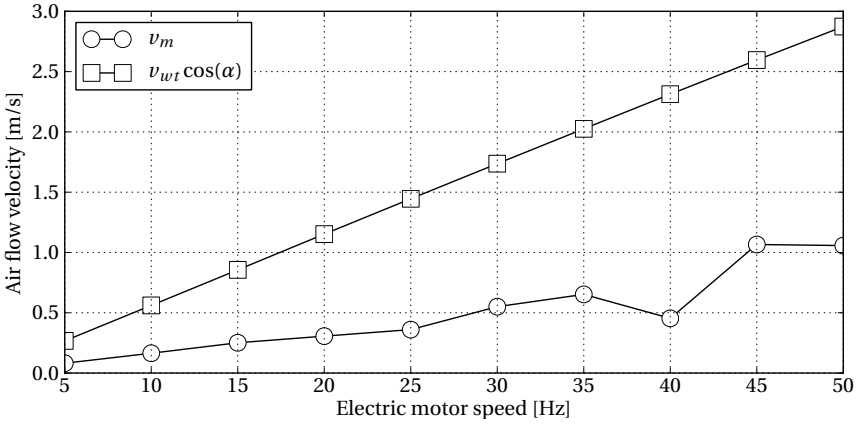

(b) Results for $\alpha = 60°$

Figure 3.5: Selected ultrasonic anemometer test results

than the calculated component of the flow in its plane. This difference increases with an increase in flow rate. The reason for this is that the flat, roof-like top of the anemometer tends to deflect the flow over the measurement probes at higher flow angles. Similar to Figure 3.4, Figure 3.5a shows the relationship between the measured and calculated, in-plane flow for a flow angle of 40°. Here one can see that the air flow velocity measured with the anemometer is still closely related to the calculated flow. Alternatively, Figure 3.5b shows how the anemometer measures a much lower in-plane flow rate at higher flow angles. The graphs for the other flow angles that were tested can be found in Appendix A.1.

A maximum measurement error of 5% is considered acceptable when considering that the anemometer is quoted by the manufacturer to have an error of ±2% at a velocity of 12 m/s. This is especially true when considering that the purpose of this investigation was not to accurately measure the magnitude of the air flow entering the fan, but instead to observe the effect that the prevailing wind has on air flow at the fan inlet.

Of greater concern than the accuracy of the anemometer is its ability to measure flow

that is not in its plane of measurement. However, the tests indicate that the anemometer can measure air flow accurately within 40° of its plane, which is more than the anemometer is expected to be subjected to when placed below the fan. It is assumed that because the ACSC is so large and that the fan being monitored is near the axis of symmetry, the flow will be mostly two-dimensional and that there will be little cross-flow across the fan inlet.

3.2 Propeller anemometer testing

The Young Model 27106 propeller anemometers are assumed to only measure the air flow velocity component in the direction of their own axis. In order to verify this the propeller anemometers were tested in the same way as the ultrasonic anemometers.

3.2.1 Test setup and procedure

The tests were conducted in the same wind tunnel as where the ultrasonic anemometers were tested. However, instead of using the 250.9 mm elliptical nozzle, the 200.8 mm one was used instead. This allowed for a higher sensitivity at lower flow rates due to the higher pressure drop over the nozzle. Also, instead of using a vise, the propeller anemometers were mounted in a laboratory stand usually used for holding test tubes. The stand allowed the anemometer to be mounted at practically any angle within the tunnel.

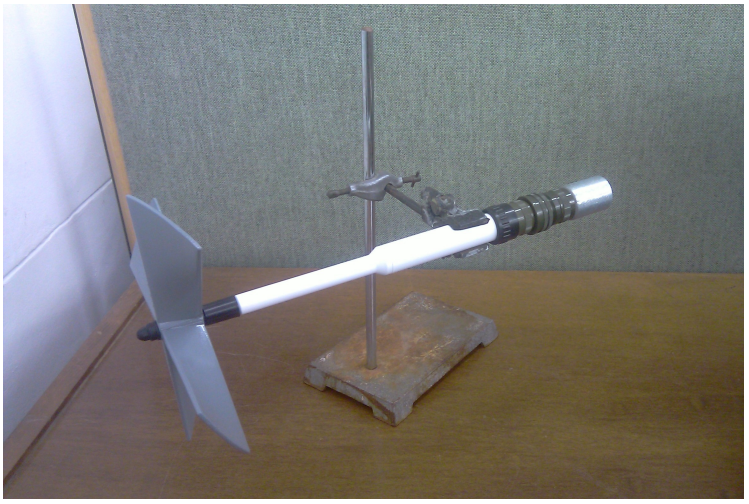

Figure 3.6: Propeller anemometer mounting for wind tunnel tests

Two tests were conducted to calibrate the anemometers. The first test was a linearity test where the anemometer was placed parallel with the direction of the flow. The speed of the fan would then be steadily increased in order to ascertain how accurately the linear relationship between output voltage and flow velocity supplied by the manufacturer can approximate the actual flow velocity. The relationship, as given by the manufacturer for the expanded polystyrene propellers, is denoted by equation 3.2 where v_m is the flow velocity measured in m/s and V_{an} is the anemometer voltage output in mV.

$$v_m = 0.01764 \times V_{an} \tag{3.2}$$

The second test consisted of setting the anemometer at angles so that the incoming flow has an off-axis flow angle ranging from 0° to 90°. The anemometer would be set at increasing angles and the flow measured at 3 different fan speeds. These speeds were 10 Hz, 25 Hz and 40 Hz.

3.2.2 Results

The results for the linearity test show that the flow rate measured by the anemometer is closely related to the calculated flow rate of the tunnel. The maximum error is approximately 5%, which for this project is acceptable. Figure 3.7a shows the results of the linearity test.

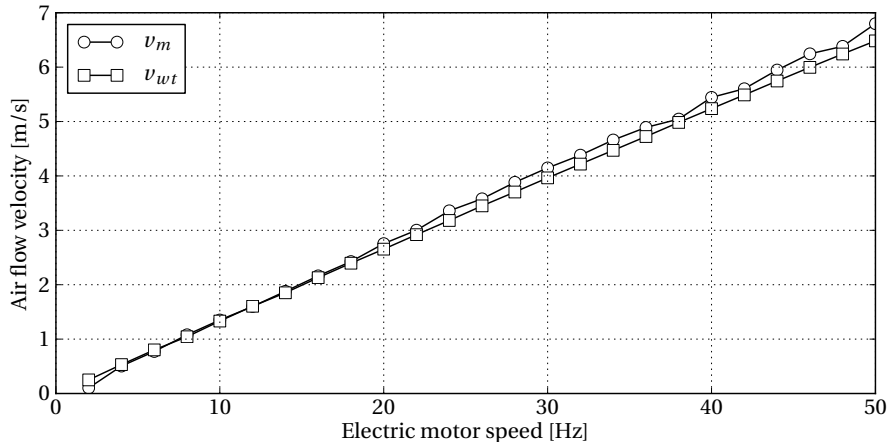

(a) Linearity test

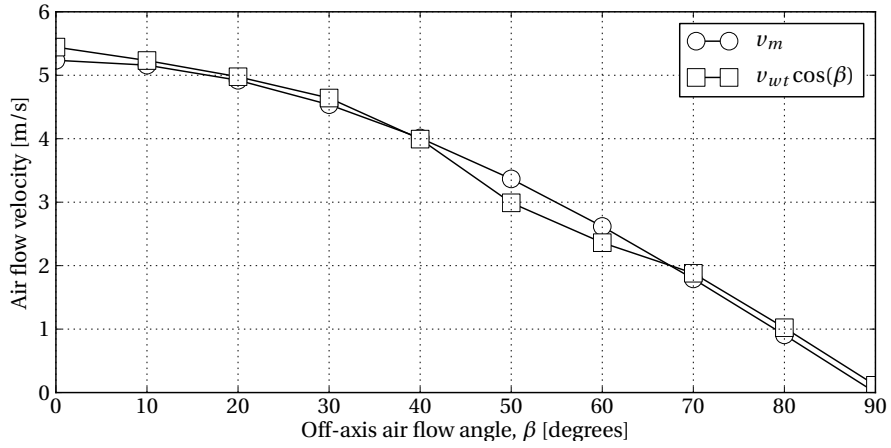

(b) Off-axis flow angles at 40 Hz

Figure 3.7: Selected propeller anemometer test results

Figure 3.7b shows the results of the off-axis flow angle test conducted at a fan speed of 40 Hz. The measured velocity is compared to the component of the tunnel's velocity in the direction of the anemometer's axis. From this it is clear that the anemometer does indeed only measure the component of the air flow velocity in the direction of its own axis. The results for the remaining fan speeds can be found in Appendix A.2.

3.3 Static fan blade tests conducted in laboratory

One of the most important measurements to be recorded was the loading profile at the blade neck as a function of the fan's rotational position. As such, it was important that there be a high level of confidence in the measurements recorded at the full-scale facility. This can be accomplished by recreating the full-scale setup in a laboratory for preparation as well as analysis and fault-finding.

For this purpose a full-scale fan blade was installed in the Structures Laboratory at the University of Stellenbosch. The primary goal of the installation was to test the capabilities and functionality of the wireless data capturing devices. As a secondary goal, it was desirable to measure the first natural frequency of the fan blade.

3.3.1 Blade mounting

To mount the blade, a frame was constructed from laser-cut pieces of 12 mm steel plate and sections of I-beam. The frame, shown in Figure 4.13, was designed to be as small as possible while still allowing the blade tip to deflect as much as possible. Swiegers (1989) built a similar, albeit larger frame in which to mount the same blade. The reason this frame was larger was because the experiments performed by Swiegers (1989) were to determine the vibrational characteristics of the fan blade and the ability of finite element methods (FEM) to model it. In order to recreate the installation at the full-scale facility as accurately as possible, the blade was mounted within the frame in the same way as it is attached to the fan hub at the power plant by using the same 30 mm U-bolts and aluminium saddles which are used as at the full-scale facility.

3.3.2 Strain gauge configuration and data capturing system

For the purpose of this test, strain gauges were attached on the top and bottom of the blade so that the bending can be measured. The strain gauges were connected in a full-bridge configuration to eliminate the effect of axial and temperature loads. The axial and temperature loads may not play a large role in the laboratory environment, but they are prominent in the full-scale dynamic tests where centrifugal forces are exerted on the blade and where the blade is exposed to the environment.

The strain gauges were connected to a MicroStrain SG-Link, which is similar in function to the MicroStrain V-Link purchased for the investigation. The SG-Link supplies the strain gauge bridge attached to it with an excitation voltage of 3 V. It then converts the sensor voltage to a 12 bit digital signal for wireless data transmission to its base station. The base station is then connected to a computer via a USB cable where the Node Commander software package is used to communicate with the SG-Link and interpret the data being transmitted.

Figure 3.8: Static fan blade mounting frame

Figure 3.9: Strain gauge attachment to static fan blade

3.3.3 Calibration and test procedure

The SG-Link has an internal 499 kΩ shunt resistor which was used to calibrate the strain gauge bridge. In order to ensure that the calibration performed through the Node Commander software was correct, a HBM calibration unit was used to simulate certain strains for comparison with the SG-Link's output. This unit is further discussed in Section 4.1.2.

Once the calibration had been completed, a simple load was placed on the tip of the blade and quickly removed. This caused the blade to vibrate freely in the flap-wise direction where strain gauge measurements were taken.

3.3.4 Data analysis and results

Figure 3.10a shows strain gauge measurements taken during a period of the blade's free vibration. It is shown that the decay in motion is exponential and as such the system can be approximated as a single degree-of-freedom mass-spring-damper system. Following the formulation provided by Meirovitch (2001), the equation of motion for the free vibration of an under damped system is given by

$$Y(t) = Ae^{-\zeta\omega_n t}\cos(\sqrt{1-\zeta^2}\omega_n t - \phi) \tag{3.3}$$

with a damped period of vibration

$$T = \frac{2\pi}{\omega_n\sqrt{1-\zeta^2}} \tag{3.4}$$

The natural frequency of the system may be obtained by calculating the Fast Fourier Transform (FFT) of the signal in the time domain. This is shown in Figure 3.10b where one can see that the natural frequency of the first bending mode, ω_n, is approximately equal to 5.4 Hz. This value is close to the 5.96 Hz that was measured by Swiegers (1989) on a similar blade more than twenty years ago.

Considering the equation of motion given by equation 3.3, the value of the i-th peak at time t_i where $\cos(\sqrt{1-\zeta^2}\omega_n t_i - \phi) = 1$ is

$$Y(t_i) = Ae^{-\zeta\omega_n t_i} \tag{3.5}$$

The ratio between two successive peaks is then

$$\frac{Y(t_i)}{Y(t_i+T)} = e^{\frac{2\pi\zeta}{\sqrt{1-\zeta^2}}} \tag{3.6}$$

or

$$\ln\frac{Y(t_i)}{Y(t_i+T)} = \frac{2\pi\zeta}{\sqrt{1-\zeta^2}} = \delta_A \tag{3.7}$$

where δ is known as the logarithmic decrement. The damping ratio, ζ, from equation 3.7 can then be rewritten in terms of the logarithmic decrement, δ_A, with

$$\zeta = \frac{\delta_A}{\sqrt{4\pi^2+\delta_A^2}} \tag{3.8}$$

From equation 3.3, one can see that the time varying envelope modulating the cosine function can be given by

$$y^*(t) = Ae^{-\zeta\omega_n t} \tag{3.9}$$

which can be rewritten in logarithmic format to obtain

$$\ln y^*(t) = \ln A - \zeta\omega_n t = \ln A - \delta_A^* t \tag{3.10}$$

where $\delta_A^* t$ is the linear slope of the exponential decay function in logarithmic space. The numerical value of $\delta_A^* t$ can be obtained by means of a linear regression curve fit on the peak data against time. From the curve fit, the damping ratio, ζ, was calculated to be equal to 4.2%.

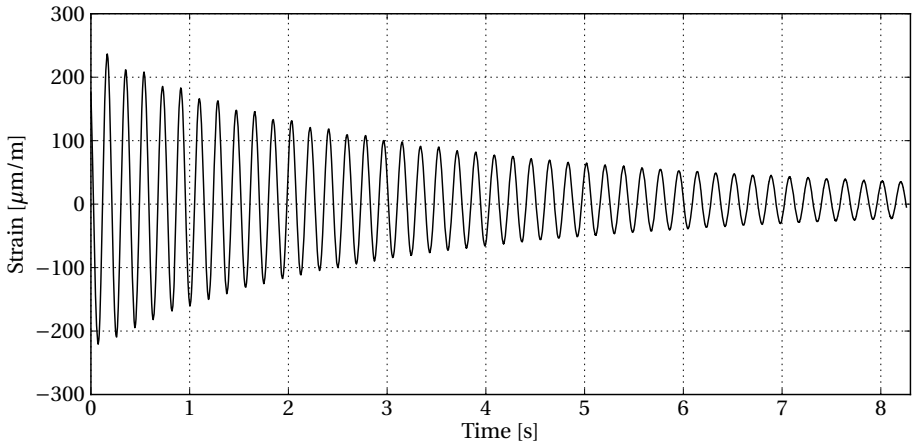

(a) Strain gauge signal

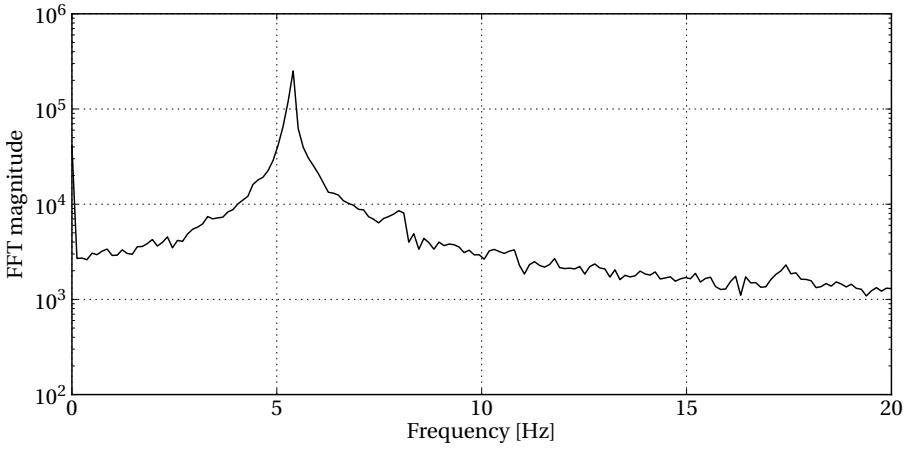

(b) FFT of signal

Figure 3.10: Static fan blade test results

3.4 Dynamic tests conducted at standard axial fan test facility

In the preparation for conducting tests at the full-scale facility, the wireless data capturing system needed to be tested on a rotating platform. For this purpose a test fan was installed at the standard axial fan test facility at the University of Stellenbosch. This facility is shown in Figure 3.11.

3.4.1 Experimental setup

A set of strain gauges was attached to a single blade on the test fan to measure bending in the flap-wise direction. The strain gauges were configured in the same full-bridge configuration as those on the static fan blade described in Section 3.3.2. The attachment of the strain gauges to the test fan is shown in Figure 3.12a.

These strain gauges were connected to the same wireless MicroStrain SG-Link bridge amplifier used during the tests on the full-scale fan blade. Due to the test fan having a relatively small hub, the SG-Link was attached to a disk located on the shaft downstream of the fan. This attachment is shown in Figure 3.12b.

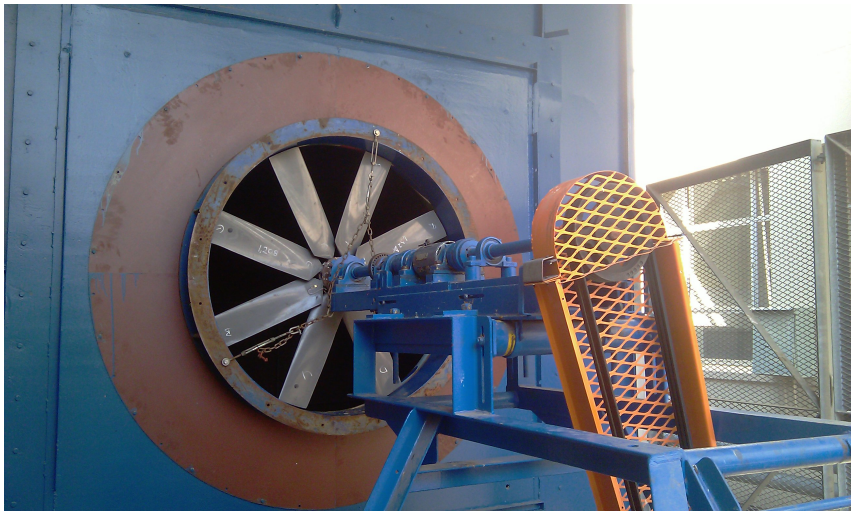

Figure 3.11: Standard axial fan test facility

3.4.2 Experimental procedure

The most significant difference between the test and the full-scale fan, apart from the size, is that the test fan is mounted vertically while the full-scale fan is mounted horizontally. In order to determine the effect of gravity on the readings, the test fan was turned slowly, by hand, so that measurements could be recorded with the blade at four rotational positions. These positions were at 0°, 90°, 180° and 270° with 0° being at the top of the fan hub and the other angles measured in a clockwise direction.

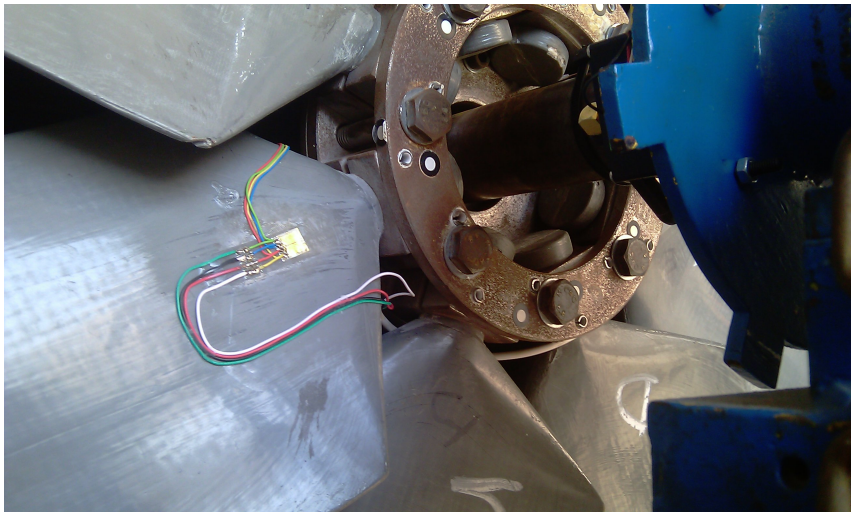

(a) Strain gauge fitment

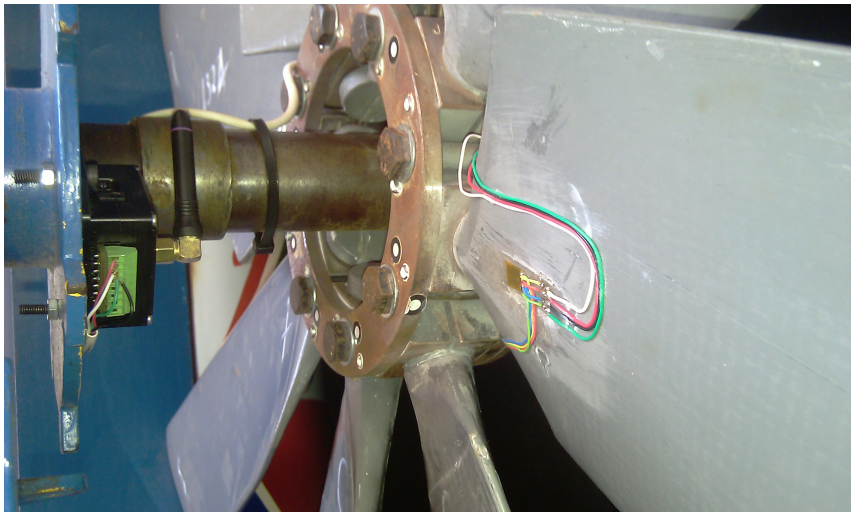

(b) MicroStrain SG-Link attachment

Figure 3.12: Strain gauge and data capturing system attachment for dynamic tests

Once data had been collected regarding the effect of gravity, the fan, along with an auxiliary fan located upstream, was switched on. An imitation fan bridge, in the form of a piece of wood, was clamped into position downstream of the fan in order to introduce a disturbance in the flow. The bridge, as shown in Figure 3.13, would cause an increase in local static pressure which would exert an additional force on the fan blade. This additional load would then be detected by the strain gauges.

Figure 3.13: Standard axial fan test facility with fan bridge installed

3.4.3 Data analysis and results

Figure 3.14 shows the results of the test to determine the effect of gravity on the strain gauge readings. The strain gauges were zeroed at the 270° position and then rotated in a clockwise direction halting momentarily at each of the four positions described in the figure. From the figure, one can see that the maximum and minimum strain is attained at 90° and 270°. This is due to the blade being under the largest bending loads at these positions. When the blade is at the 0° and 180° position the load is purely axial and is therefore rejected by the full-bridge configuration of the strain gauges.

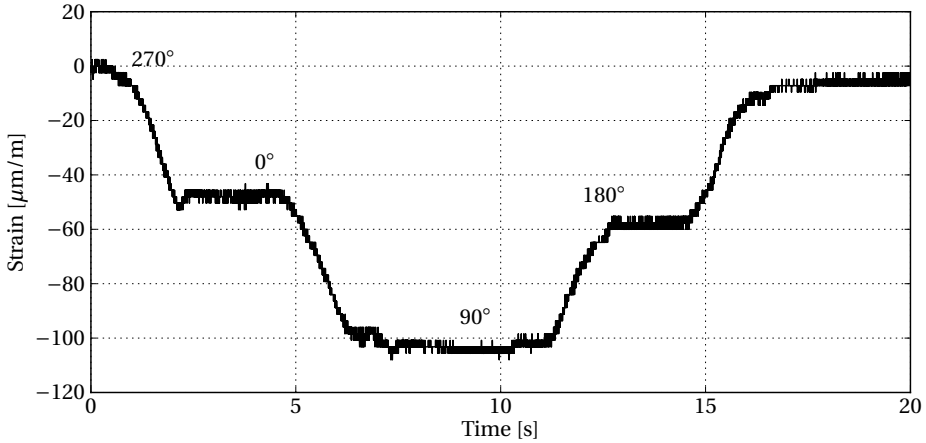

Figure 3.14: Gravity test results

Figure 3.15 shows the data recorded with the wooden fan bridge installed. One can observe the effect of gravity on the measured data as a sinusoidal variation in the signal. There is also a large negative offset due to the auxiliary fan's airflow exerting a force on the test fan. The strain gauges were connected in such a way that a negative signal depicts bending in the downstream direction. If the fan was rotating faster and working as it should, the offset in the strain measurements would be positive and not negative. However, the rotational speed of the fan had to be limited to 10 Hz to avoid any possible damage to the SG-Link.

In order to remove the effect of gravity on the readings, a sinusoidal curve was fitted to the measured data and is shown in Figure 3.15. When this curve is subtracted from the measured data, the difference between the two readings represents the data that would have been collected if the fan was mounted horizontally instead of vertically. When considering the difference between the measured data and the fitted sinusoidal curve one can see spikes in the data occurring at the same frequency as the sinusoidal curve. If the positions of the spikes are connected to the measured data it is clear that they coincide with the instances that the fan blade was at the 180° position where the wooden fan bridge was installed. This shows that the strain gauge setup is sensitive enough to detect the change in static pressure brought about by the presence of the wooden fan bridge.

In conclusion, the dynamic tests conducted with strain gauges and the MicroStrain SG-Link have shown that the wireless data capturing system performs well on a rotating platform and that the strain gauge setup is sensitive enough to detect small disturbances in air flow and fan operational characteristics. As such, the system is suitable for use at the full-scale test facility as well as any future experiments conducted at the standard test facility.

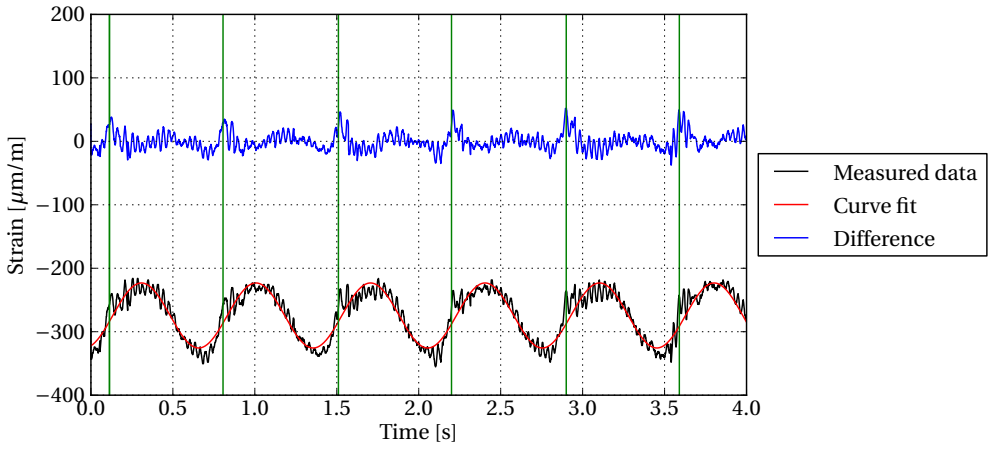

Figure 3.15: Dynamic test results

Chapter 4

Sensor installation at full-scale facility

Once all of the equipment had been tested in the laboratory, each component was installed at the full-scale facility. This chapter provides the detail regarding the installation and calibration of the equipment at the full-scale facility.

4.1 Strain gauge installation

As a result of the aerodynamic loading, stresses exist within the fan blade. These stresses are expected to vary as the fan rotates due to the change in pressure and air inflow patterns on different sides of the fan. Blade loading can easily and reliably be determined with strain gauges placed on the neck of the fan blade. A single fan blade was fitted with strain gauges in order to measure the strain on the blade during the rotation of the fan. Subsequently, this information can be used to draw conclusions regarding the required strength of the composite fan blades under windy conditions.

This approach has been used in a similar experiment by Xu *et al.* (2004). They placed strain gauges at various locations on the blade to compare experimental stress values to the results obtained in their finite element analysis of a 1.829 m diameter fan. Simms *et al.* (1999) also used strain gauges to measure the bending of the blades on a 10 m diameter wind turbine.

Similarly, the loading on the fan gearbox can be measured with strain gauges attached to the low speed shaft. These strain gauges were configured to measure bending and torsional strains. Torsional measurements on a shaft to determine the effect of rotor induced vibrations have been performed in experiments by Al-Bedoor *et al.* (2004). They were able to correlate vibration as a result of excitation at the rotor blades to a torsional response within the shaft of their model.

4.1.1 Attachment of strain gauges to the fan blade

The strain gauges used to measure strain in the cylindrical neck of the fan blade were installed between the blade's shoulder and the U-bolts attaching it to the fan hub. According to cantilever beam theory, this is the area where the maximum strain will be experienced and as such will give an indication of the cumulative effect that the aerody-

namic loading has over the entire span of the blade. Also, by placing the strain gauges on the cylindrical neck of the blade the full-bridge configuration is able to compensate for the axial strain caused by the centrifugal load.

The surface of the blade was prepared by using fine grit sanding paper to remove the paint and gel-coat so that the amber-coloured resin holding the laminate plies together, was exposed. Once these layers were sanded off, the surface was thoroughly cleaned using acetone after which the strain gauges and soldering tabs were attached to the fan blade using strain gauge cement. After the strain gauges were attached to the blade surface, the wiring between the gauges was completed and they were connected to the V-Link units. Figure 4.1 shows the attachment of the gauges to the blade as well as the wiring between the sets of gauges and each V-Link. In addition to being sealed by a layer of resin, the strain gauges were also covered in silicone for added protection.

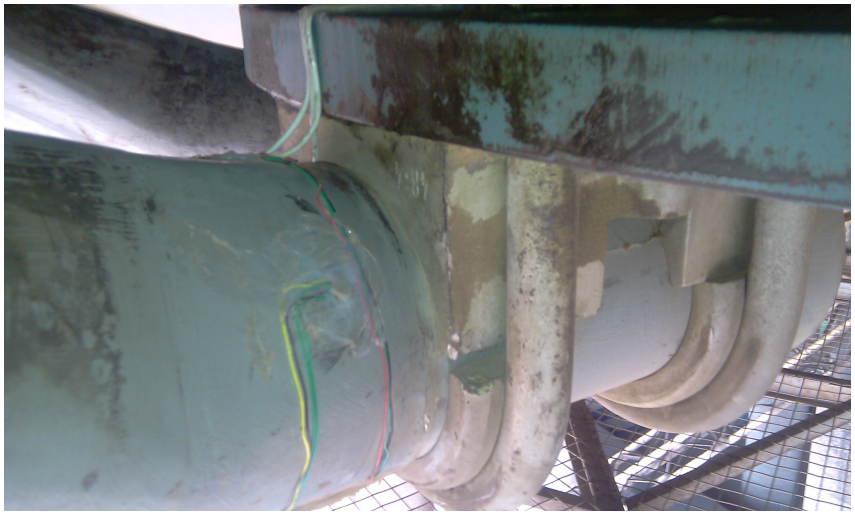

(a) Side view

(b) Bottom view

Figure 4.1: Strain gauges attached to full-scale fan blade

Once the attachment and wiring of the strain gauges had been completed, the installation was tested for any breaks in the wiring or gauges. This was done by measuring the resistance over the various terminals with a multimeter. Considering that the strain gauges each had a resistance of 350 Ω and were connected in a Wheatstone bridge configuration as depicted in Figure 1.11, the resistance across the V_{out} and V_{in} terminals should each be 350 Ω, while the measurable resistance over each individual strain gauge can be calculated to be

$$\begin{aligned} R_m &= \frac{1}{\frac{1}{350} + \frac{1}{3\times 350}} \\ &= 262.5\,\Omega \end{aligned} \tag{4.1}$$

4.1.2 Strain gauge calibration

Modern bridge amplifiers, including the MicroStrain V-Link system which was used, are able to perform shunt resistor calibrations internally. Each V-Link has a 499 kΩ resistor for this purpose. To calibrate the strain gauge bridges connected to each V-Link, the Strain Wizard calibration tool in the Node Commander software was used. The application has functions to balance the Wheatstone bridge and determine the calibration coefficients for the strain gauges. As stated in Section 2.1, the V-Link units provide a digital signal, which is converted to an analogue voltage by the base stations. The calibration coefficients then form part of an equation relating the digital signal to the strains being measured.

Figure 4.2 shows the channel configuration screen from the Node Commander software package. Starting from the left, the Programmable Gain Amplifier (PGA) settings allow the adjustment of the gain applied to the output signal from the strain gauge bridge as well as the balancing thereof. To the right one can see the unit conversion applied at software level as well as the button used to initiate the Strain Wizard function. As previously stated, the Strain Wizard is used to determine the calibration coefficients and has options to adjust the shunt resistance as well as the number of active gauges and gauge configuration. Below this is the output of the calibration coefficients, referred to as the slope and offset.

Before the hardware was installed at the full-scale test facility, the calibration functions embedded in the V-Link system was tested on a HBM calibration unit. The purpose of this test was to verify that the Strain Wizard was functioning correctly and that its default settings were being adjusted correctly. The calibration unit, shown connected to a V-Link in Figure 4.3, simulates a full- or half-bridge strain gauge configuration and can, with the turn of a knob, be adjusted to produce different strains within the simulated bridge. The strain output from the Node Commander software was compared to the strain simulated by the calibration unit for a variety of strains in order to verify the settings that were adjusted during strain gauge channel configuration. The inclusion of this final test increased the confidence in, and the understanding of the strains being measured with the V-Link system.

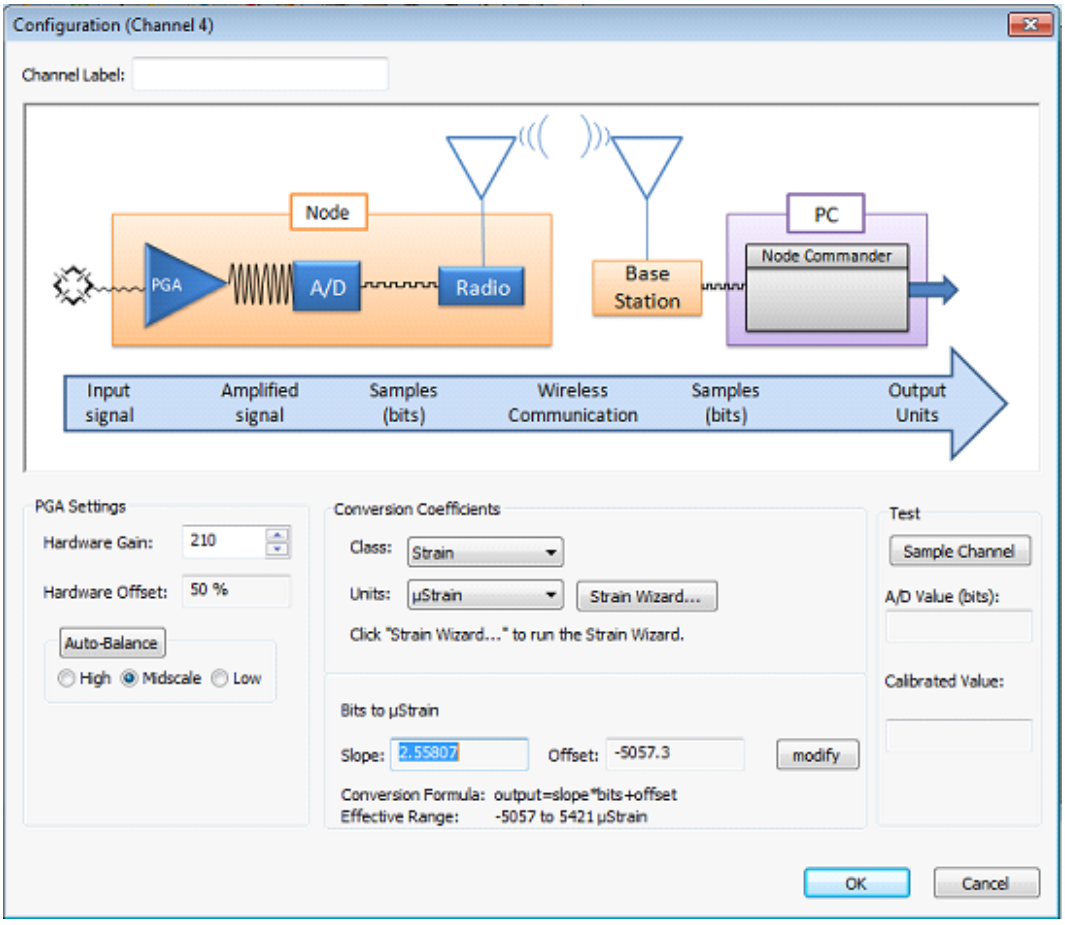

Figure 4.2: MicroStrain Node Commander channel configuration

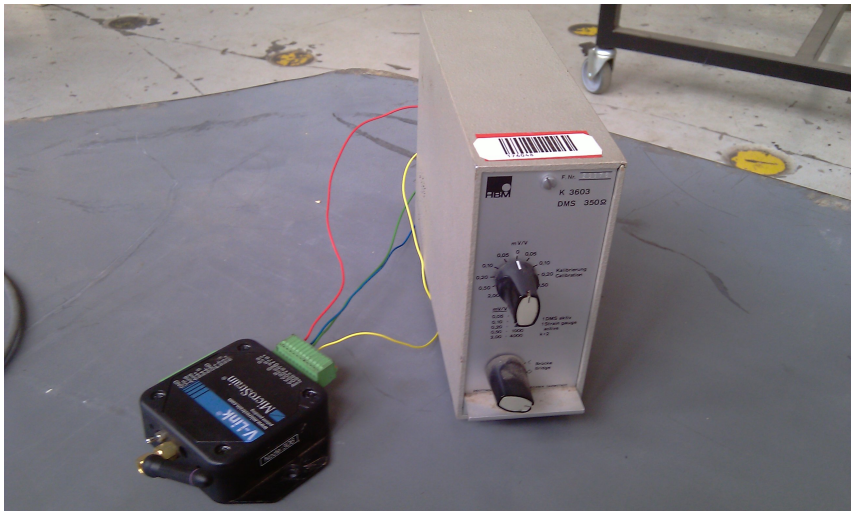

Figure 4.3: HBM calibration unit attached to V-Link

4.1.2.1 Calibration problems

After the strain gauges had been attached to the fan blade and had been wired and tested, they were calibrated using the Strain Wizard application. The correct calibration procedure was followed for each of the strain gauge bridges and the calibration coefficients were determined and recorded. However, the channel measuring bending strain in the flap-wise direction could not be calibrated. The Strain Wizard application determines the offset and slope coefficients by scaling the measured data to a low-high-low square waveform. When there is movement in the blade this scaling becomes less accurate due to the measured signal not being stable. However, for this particular channel the measured strain exceeded the upper and lower measurement bounds and as such was impossible to calibrate.

Figure 4.4a shows a screen from the Strain Wizard calibration function when attempting to calibrate the channel measuring bending strain in the flap-wise direction on the fan blade. The green line represents the measured data, which, if the strain gauges are functioning correctly, should form a square wave pattern. The dotted red and blue lines then represent the upper and lower bounds of the waveform and are used to determine the calibration coefficients. One can see that in this case the measurements were exceeding the upper limit of 4096 bits. At the time it was presumed that this was due to the vibration of the blade caused by the extremely windy conditions inside the plenum chamber brought about by the other fans. However, after recreating the setup in the laboratory by forcing the stationary fan blade to vibrate while trying to calibrate the strain gauge channel it was concluded that even though the vibration of the blade had an influence on the calibration of the strain gauges, it could not be the cause of the measurements exceeding the upper limit of the system. Figure 4.16b presents the results obtained in the laboratory where the measured strain remains unstable due to the vibration, but does not exceed the measurement limits.

A simple solution to the problem of the measurements exceeding the upper limit would be to turn down the gain on the amplifier. However, the gain was already at its lowest setting and since the other channels were calibrated fairly easily it was concluded that the fault had to be with either the strain gauges or the connectors attaching the wires to the V-Link units. After the connectors had been checked and replaced, with no success, the strain gauges were removed and replaced as well. Replacing the gauges proved to be more difficult than the initial installation due to increased wind speeds and gusts at the fan. A common occurrence was that the contact points on the strain gauges were accidentally torn off while soldering the wires to them due to the rough winds. The solution to this problem was to prepare the strain gauges in such a way that no delicate soldering would be required at the fan. Figure 4.5 shows a set of strain gauges that have been prepared on a piece of glass. Single wire strands were soldered between the strain gauges and the soldering tabs where thicker, more robust wires were connected.

Once the prepared strain gauges were attached, tested and calibrated, the fan was switched on in order to gather the first set of measurements. All of the channels were working well with the exception of the channel measuring bending strain in the flap-wise direction. The measured strain once again exceeded the upper limit and was unusable. When the fan was switched off the next day, a crack was observed across the set of gauges attached to the top of the blade. The crack can be seen in Figure 4.6 along with several other surface defects on the fan blade. Subsequently, the gauges were replaced again and

moved to an area of the fan blade which, after careful inspection, was free of any surface cracks.

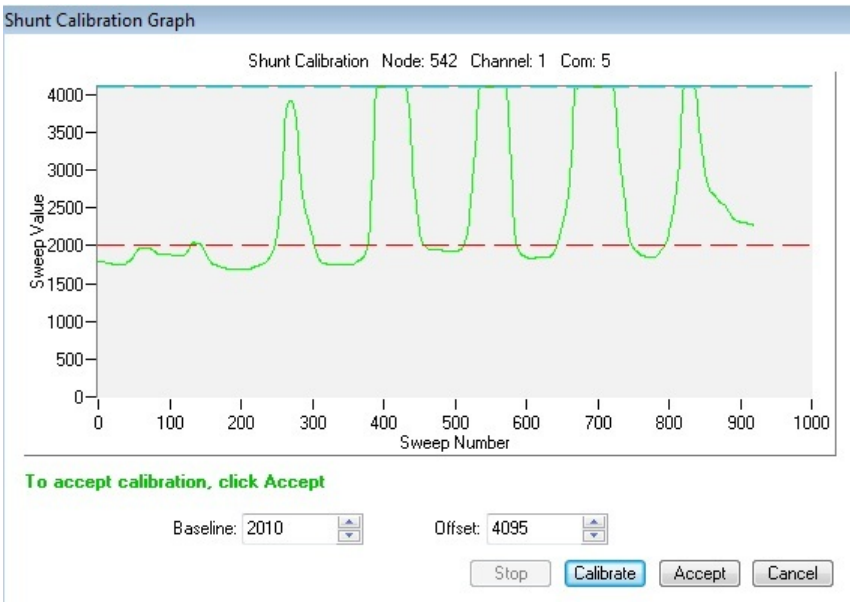

(a) Calibration attempt at facility

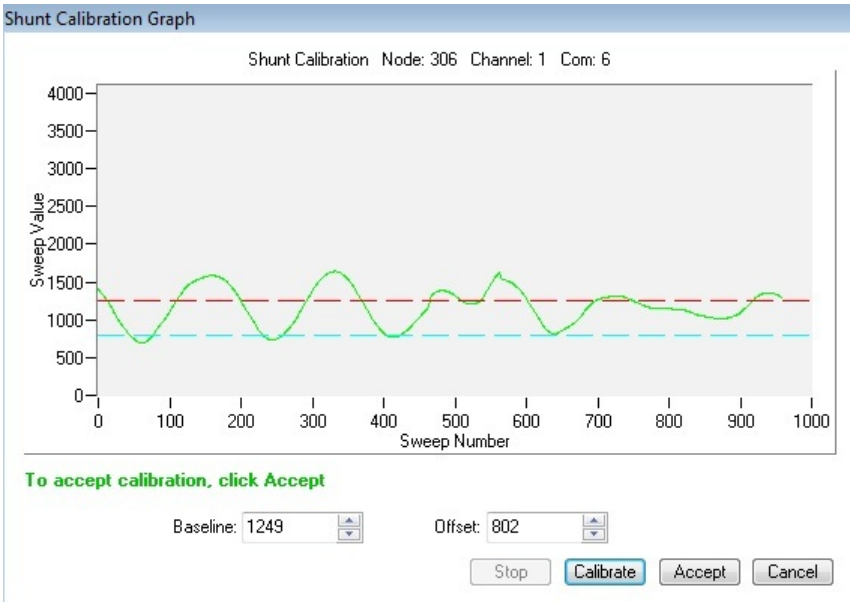

(b) Calibration in lab with forced vibration of blade

Figure 4.4: Calibration function in Node Commander

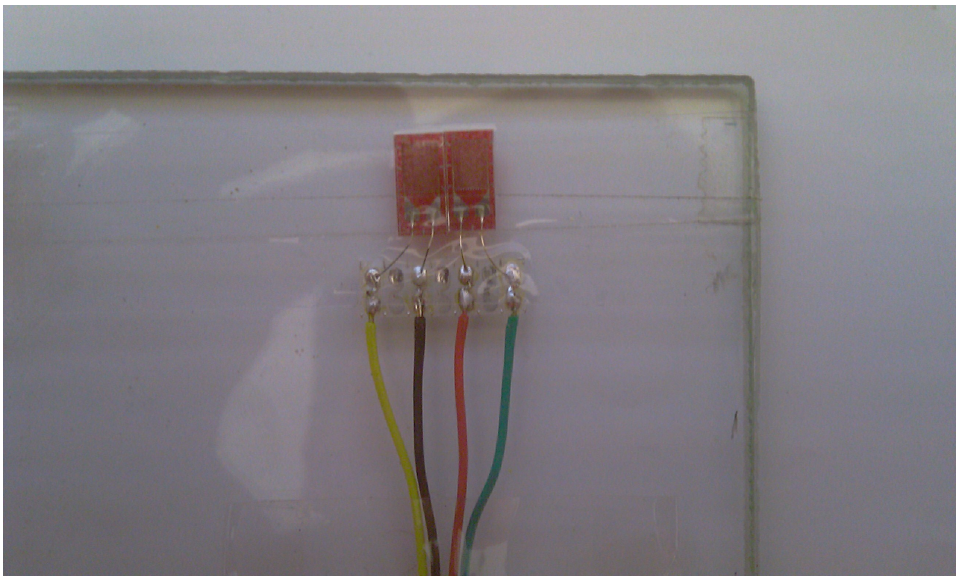

Figure 4.5: Strain gauges prepared on a piece of glass

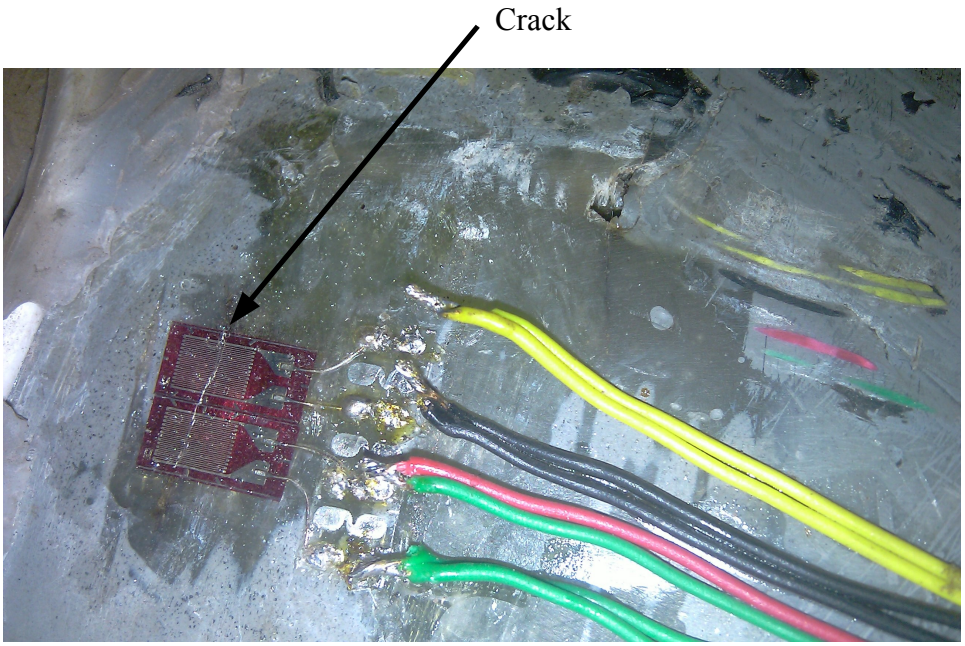

Figure 4.6: Damaged strain gauges attached to full-scale fan blade

4.1.2.2 Load calibration

When measuring strain on a metal object it is fairly simple to translate the measured strain into a load or a stress. The reason for this is that the material properties of metals are often known and are isotropic. This is not the case with composite fan blades and as such an additional calibration was required to equate the measured strain to a known load.

Normal stress, σ, is related to the strain, ϵ, with the modulus of elasticity, E, using the following relationship

$$\sigma = E\epsilon \tag{4.2}$$

For a cantilevered beam, the bending stress is related to the applied moment, M, the distance from the center of the beam, y, and the moment of inertia, I, with the following equation

$$\sigma = \frac{My}{I} \tag{4.3}$$

Combining equation 4.2 and 4.3 yields a relationship between bending strain and the applied moment

$$\epsilon = \frac{y}{EI}M \tag{4.4}$$

Considering that $\frac{y}{EI}$ is a constant based on the material properties and the geometry of the blade neck, it becomes clear that the relationship between bending strain and applied load is linear. In order to determine the $\frac{y}{EI}$ coefficient an additional calibration was performed using a load cell and a ratchet strap. The ratchet strap was placed over the blade and fastened onto the safety grid on one side and the load cell on the other, as is shown in Figure 4.7. The tension in the strap was increased and data was recorded regarding the strain in the blade neck and the applied load. The extremely windy conditions made it very difficult to work with the strap and since it was fastened to the safety grid it was decided that, to prevent damage to the grid, the load should not exceed 70 kg.

Figure 4.8 presents, schematically, the distance from the applied load to the strain gauges as well as the angular position of the flap-wise gauges relative to the vertical, which is depicted by θ. The strain gauge bridges were 90° apart and aligned with an approximate angle of $\theta = 26.5°$. The load was applied at a distance of approximately $L = 3.4\,\text{m}$ from the neck of the blade where the gauges were attached. The applied moment about the y'-axis (lag-wise direction) can then be calculated using the following equation

$$M_{y'} = 9.81FL\cos(\theta) \tag{4.5}$$

The moment about the x'-axis (flap-wise direction) is then

$$M_{x'} = 9.81FL\sin(\theta) \tag{4.6}$$

The results of the calibration are presented in Figure 4.9. The readings taken by each set of strain gauges (flap- and lag-wise) at the blade neck are shown and, by fitting a straight line through the data points, one is able to obtain two equations for the relationship between strain and load which can be applied to any future measurements.

Figure 4.7: Strain gauge load calibration at full-scale facility

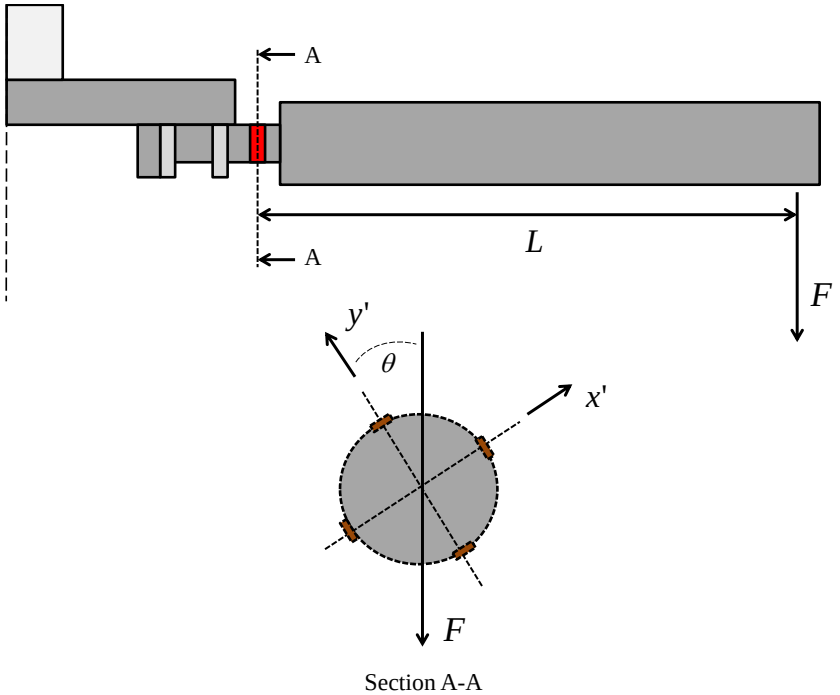

Figure 4.8: Load calibration dimensions and strain gauge orientation

Due to the difficulty of performing an accurate torque calibration at the full-scale facility, an additional torque calibration was performed in the Structures Laboratory at Stellenbosch University using the static fan blade and frame described in Section 3.3. The fan blade was turned sideways and forces were applied in two directions with cables to induce a moment about the neck of the blade. Load cells were used to measure the tension in each cable. Figure 4.10 shows the experimental set-up with cables attached to the end cap which was manufactured for the full-scale fan blade. Results for this calibration are included in Figure 4.9.

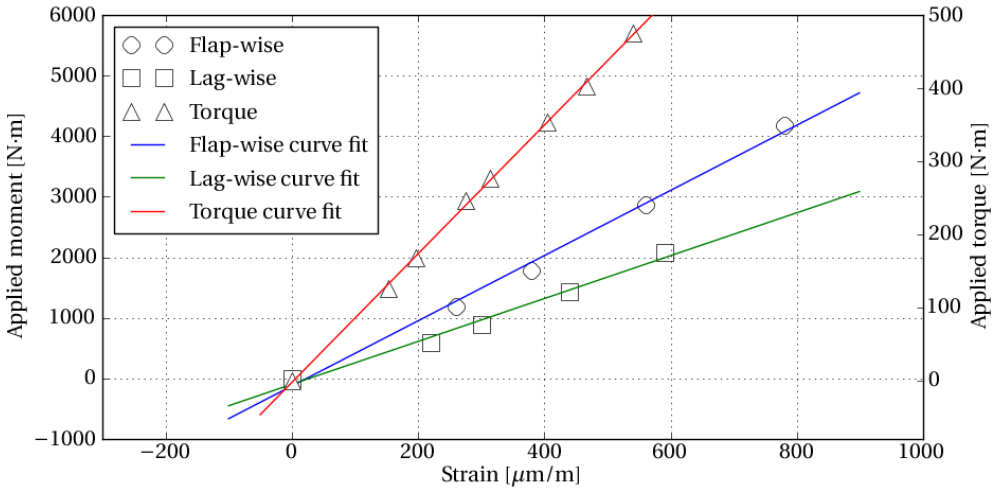

Figure 4.9: Load calibration results

Figure 4.10: Torque calibration

4.1.3 Strain gauge attachment to fan shaft

Strain gauges were attached to the fan shaft to measure bending strain in two orthogonal directions as well as torsional strain. The strain gauge attachment to the fan shaft is shown in Figure 4.11. These gauges were attached, tested and calibrated in the same way as the gauges on the blade. However, no additional load calibration was required due to the material properties of steel being known. After being tested, these gauges were also covered in silicon to protect them from being damaged.

Figure 4.11: Strain gauges attached to low-speed shaft

4.2 Fan blade position sensor installation

In order to determine the location of the blade during the rotation of the fan, a Hall-effect proximity sensor was attached to a threaded rod extending out below the bridge where the motor and gearbox is situated. The proximity sensor was positioned above the pitch circle diameter of the 30 mm bolts attaching the coupling flange to the hub of the fan. In order to produce the desired, once-per-revolution signal a hexagonal nut was attached to the top of one of these bolt heads to act as a protrusion for the proximity sensor to detect. Figure 4.12 shows how the proximity sensor was installed. The nut was attached in such a way that a signal would be produced when the fan blade reaches the peripheral side of the ACSC.

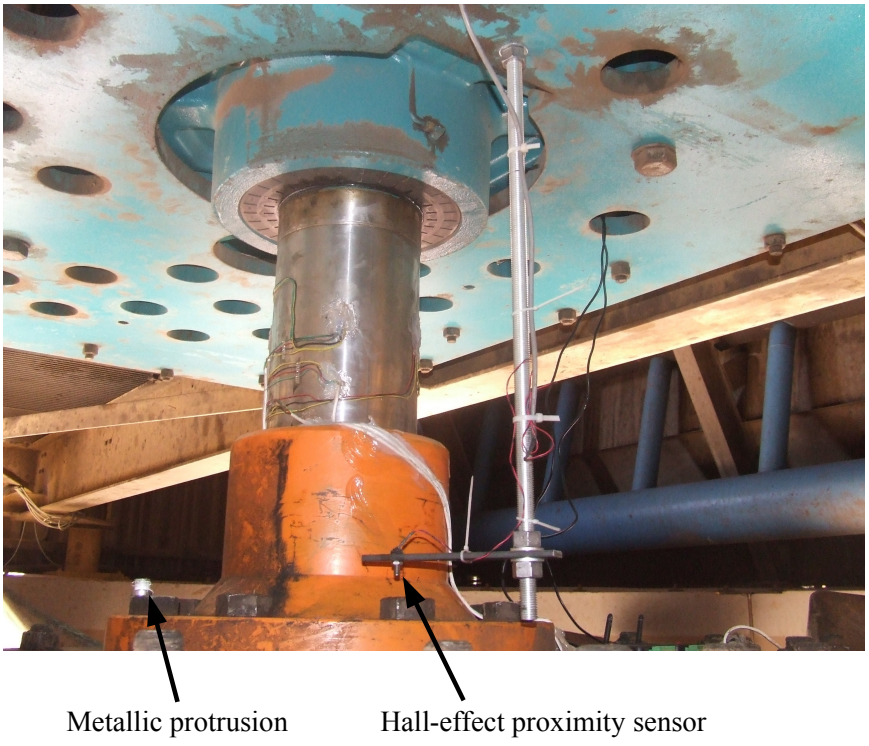

Figure 4.12: Proximity sensor installation

4.3 Sensor installation for measurement of the fan inlet air flow conditions

Measurement of the air flow profile at the fan inlet provides an indication of the degree of inflow distortion as a result of windy conditions. This incoming air flow field, measured at the safety grid below the fan, can then be used to further analyse the stresses that the blade experiences during its rotation.

4.3.1 Inlet measurement stations

To measure the inlet air flow field, 6 2-axis ultrasonic anemometers were mounted on 6 frames which were placed on the safety grid below the fan. Each frame formed the basis of a measurement station which had sensors to measure the 3-dimensional air flow velocity vector and temperature. The frames were constructed from steel square tubing and had a plastic cover within which all the wires were connected and kept protected. These stations could then be placed at different locations at the fan inlet depending on the purpose of the test being conducted and can be seen in Figure 4.13.

Figure 4.13: Measurement station placed at fan inlet

As discussed in Section 1.5.2, it was decided to use ultrasonic anemometers to measure the inlet air flow due to their high sampling rate and multi-dimensional measurement capabilities. The selected anemometer was the GILL WindSonic 2-axis ultrasonic anemometer which is shown in Figure 1.13b. It has a maximum output rate of 4 Hz and two analogue voltage output channels for wind speed and direction, respectively. The output range for the velocity channel can be adjusted between a maximum of 5 m/s and 30 m/s. Adjustment of these settings requires the connection of the anemometer to a PC via a RS232 connection as well as a 12 V power source. Once connected, the internal settings of the anemometer can be changed in the Wind software package provided by GILL. To account for wind gusts and distorted flow, the ultrasonic anemometers were set up for a maximum air flow velocity of 20 m/s. Power was provided to the ultrasonic anemometers via the data recording system by configuring custom sensor channels with the appropriate supply voltages.

Propeller anemometers were used in conjunction with the 2-axis ultrasonic anemometers to measure the out-of-plane component of the velocity vector. The selected propeller anemometers are the R.M. Young Model 27106 anemometers. As previously stated in Section 3.2, these anemometers provide a voltage output proportional to the air flow velocity. The use of the propeller anemometers enabled the system to measure the full 3-dimensional air flow velocity vector at the frame's location. The propeller anemometers were purchased in two batches with the first batch of 4 units being used for the laboratory tests. These anemometers were ordered with expanded polystyrene (EPS) propellers due to them having a very low starting threshold of 0.3 m/s as a result of their low mass. However, it was decided that the rest of the anemometers should be ordered with carbon fibre propellers as the EPS propellers were very weak and could possibly be damaged during installation.

The decision to use a combination of 2-axis ultrasonic and propeller anemometers instead of the 3-axis ultrasonic anemometers was made in order to increase the reconfigurability of the system. Propeller anemometers were already being used for the bundle outlet air flow measurements described in Section 4.4 and did not add any extra complexity to the data capturing system as no additional channels were required.

Measurement of the inlet air temperature enables the calculation of the air density, which in turn allows for the calculation of mass flow rates as well as lift and drag forces exerted on the fan blades. Measuring the inlet air temperature also makes it possible to detect when hot air recirculation is taking place. Hot air recirculation is a phenomenon where the air that is heated up by the steam in the heat exchangers gets drawn back into the fans close to the edges of the ACSC. This usually occurs when the wind is blowing and results in a decrease in the performance of the ACSC. To measure the temperature of the inlet air, 1 thermocouple was placed on each of the 6 measurement stations. As explained in Section 2.2, the data capturing system was only able to measure normalised voltage and current signals. As such, it was not possible to connect the thermocouples to the data capturing system directly. To normalise the thermocouple signals, FineTek temperature transmitters were used to provide a 4 -20 mA signal to the data capturing system for a temperature range of 0 -70 °C. These transmitters were loop powered and required a 12 V power source. A loop powered device works by transmitting the measured current along the same circuit as the power supply. The transmitters were therefore connected to the data capturing system on specially configured channels which could measure the signal and provide the required voltage.

After the frames had been assembled and all the sensor connections were tested, the frames were placed along the centreline of the safety grid below the fan in the z-direction with the ultrasonic anemometers oriented in such a way that they could measure the air flow in the yz-plane. The propeller anemometers then measured the flow in the x-direction. A photo showing the frames placed on the safety grid below the fan can be seen in Figure 4.14. Shielded cables from each of the measurement stations were fastened to the safety grid with cable ties and taken up along the side of the fan casing to the data capturing system. The cables were securely fastened to the casing with large cable ties and covered in silicone for added protection.

Figure 4.15 shows the positioning and orientation of the six pairs of ultrasonic and propeller anemometers in a top view of the selected fan within the ACSC. The surrounding fan units are not illustrated, but are represented by the light grey fill.

Figure 4.14: Positioning of measurement stations on safety grid at fan inlet

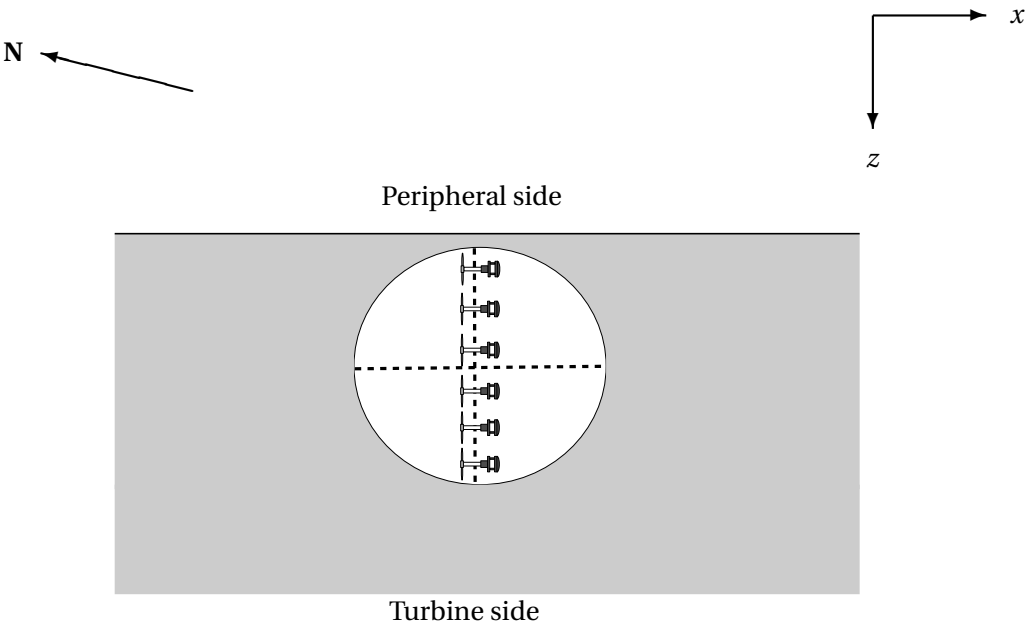

Figure 4.15: Measurement station positions and orientation

4.4 Anemometer installation for heat exchanger bundle outlet air flow velocity measurement

The cooling capability of an ACSC is proportional to the rate of air flow through the heat exchanger bundles. During windy conditions, some fan units may have lower flow rates than others due to their location within the ACSC. The purpose of the current project was to determine the effects that wind conditions have on the air flow at the fan inlet as well as how the air is distributed when passing through the heat exchanger bundles. In a previous investigation, Zapke (1997) used propeller anemometers attached to a traversing beam to measure the velocity profile at the outlet of an ACSC bundle. The beam started at the top of the inclined bundle and was moved down in order to obtain a complete air flow velocity profile at the heat exchanger bundle outlet.

One fan unit has 8 heat exchanger bundles (4 on either side of the A-frame). To determine the distribution of air flow, each heat exchanger bundle had a single propeller anemometer placed at its outlet to measure the component of air flow velocity perpendicular to the bundle. Figure 4.16a shows the anemometers attached to the outlet of each individual heat exchanger bundle. The anemometers were attached to the heat exchanger bundles with steel brackets. Hydraulic clamps were used to secure the anemometers to the brackets while the brackets were each fastened to cross-members on the bundles with two 10 mm bolts. During installation, the anemometers were positioned as close to the bundle outlets as possible to obtain an accurate measurement of the air flow velocity. The brackets and fastening mechanisms used can be seen in Figure 4.16. Shielded cables from each of the anemometers were routed to the data capturing system in the plenum chamber through a gap below the heat exchanger bundles.

(a) Positioning of anemometers along heat exchanger bundles

(b) Anemometer frame attached to heat exchanger bundle

Figure 4.16: Anemometer placement at heat exchanger bundle outlets

Chapter 5

Measurement results

Once the system had been installed, tests were conducted at the full-scale facility over a period of 8 days. Data was recorded from a weather mast located on-site as well as from the array of sensors located at the ACSC fan unit. The location of the weather mast is shown in Figure 1.4 with sensors located at a height of 40 m. An effort was made to record data during a variety of ambient weather conditions over the testing period. This chapter describes and provides analyses for the correlations between air flow and mechanical loading profiles on the fan blade and shaft. Only the measurement results relating directly to important conclusions are displayed in this chapter while the remaining results can be found in Appendix B.1, B.3 and B.4.

The 8 day measurement period was from 14/11/2011 to 22/11/2011. Measurements were not taken on 15/11/2011 because of time spent performing load calibrations on the strain gauges. Also, for the first few measurement days the weather mast located at the facility was not in working order, but was functioning again from 17/11/2011.

The sensor configuration was changed on 19/11/2011 in order to provide the additional data capturing capacity to record measurements from the anemometers located at the heat exchanger bundles. Two of the measurement stations at the fan inlet had to be disconnected to provide the required capacity. The two stations that were disconnected were the ones located closest to the fan hub. The reason why these two stations were disconnected was because measurements recorded by Van Aarde (1990) has shown that the air flow near the hub of the fan is significantly lower than air flow near the edges.

5.1 Fan inlet air flow velocities

Windy conditions cause cross-flow at the fan inlet and affects the air flow into the fan. This section presents the inlet air flow measurements that were recorded and the discussions regarding wind speed, direction and the effect thereof on air flow into the fan. The directional conventions used in this section are illustrated in Figure 1.18 and reiterated in Figure 4.15. According to this convention, the y-direction represents the vertical direction into the fan while the x-direction is parallel to the longitudinal axis of the ACSC and the z-direction is parallel to its lateral axis. In addition, the indicated locations of each measurement station is described as a distance along the z-axis with the fan casing on the peripheral side being at $z = 0$ m. Therefore, the $z = 7.870$ m location refers to the

measurement station placed closest to the turbine side of the fan casing, 7.870 m away from fan casing on the peripheral side of the fan.

Air flow into the fan is influenced by wind speed and direction. On 19/11/2011 the wind blew from the North-West until approximately 17:00 where it suddenly shifted to a an Easterly direction and increased in speed. The wind direction and speed for the day is presented in Figure 5.3 with the inlet air flow also shown. While the wind was blowing from the North-West the air flow into the fan was higher on the peripheral side of the fan than on the turbine side. After 17:00, in addition to the increase in air flow velocity on both sides of the fan, the air flow on the turbine side exceeded the air flow on the peripheral side.

A similar trend in air flow distribution can be seen when investigating the data collected on 20/11/2011 and 21/11/2011. On 20/11/2011 the wind, shown in Figure 5.4, was blowing from the North-West until 13:00 when it shifted to a Westerly direction. The corresponding air flow into the fan during the day, shown in the same figure, was higher on the peripheral side of the fan than on the turbine side. In contrast, the wind on 21/11/2011, shown in Figure 5.5, was blowing from the North-East where it resulted in higher air flow on the turbine side than on the peripheral side of the fan. As such, the distribution of air flow into the fan in the y-direction is largely dependant on the prevailing wind direction with winds from the East causing higher flow into the turbine side of the fan and winds from the West resulting in the opposite.

In addition to the bias in air flow into the fan, on days with Easterly winds the average flow velocity into the fan was higher than on days when the wind was blowing from the West with the same velocity. This can be seen in the fact that on 21/11/2011 the average air flow into the fan, shown in Figure 5.5 was between 5 m/s and 10 m/s with a Easterly wind of approximately 4 m/s while on 20/11/2011 the average air flow, shown in Figure 5.4 was only between 0 m/s and 5 m/s with a Westerly wind of the same magnitude. Similarly, on 18/11/2011 and 19/11/2011 changes in wind direction from a Westerly to an Easterly direction caused increases in air flow, shown in Figure 5.2 and Figure 5.3, into the fan.

Increased wind speed also had the effect of causing increasing air flow into the fan. On 19/11/2011 the air flow into the fan, shown in Figure 5.3, increased with the large increase in wind speed. Additionally, the wind was blowing from approximately the same direction, but at a much higher speed on 22/11/2011 than on 20/11/2011 which resulted in the air flow into the fan, shown in Figure 5.4 and Figure 5.6, being higher on 22/11/2011 than on 20/11/2011.

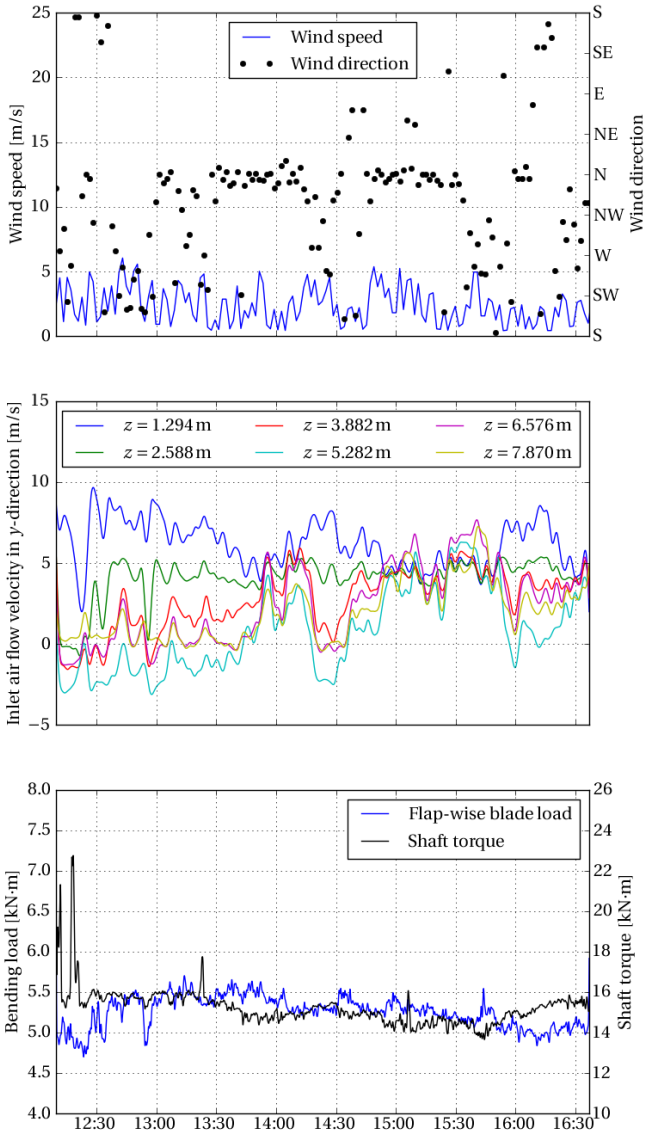

Figure 5.1: Measurements recorded on 17/11/2011

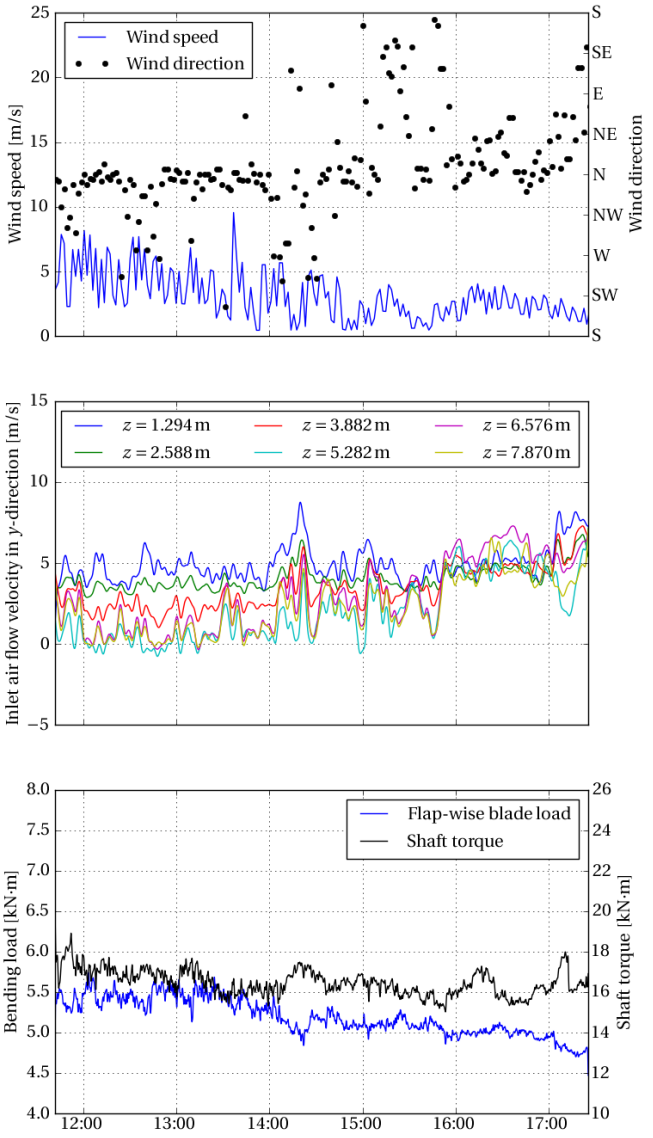

Figure 5.2: Measurements recorded on 18/11/2011

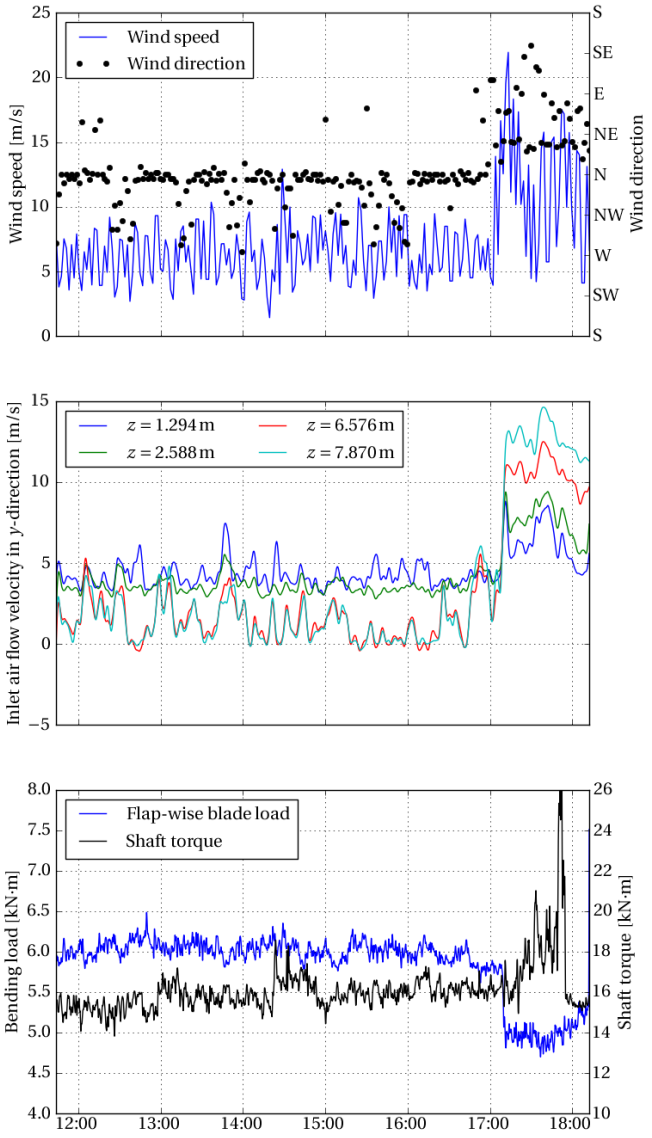

Figure 5.3: Measurements recorded on 19/11/2011

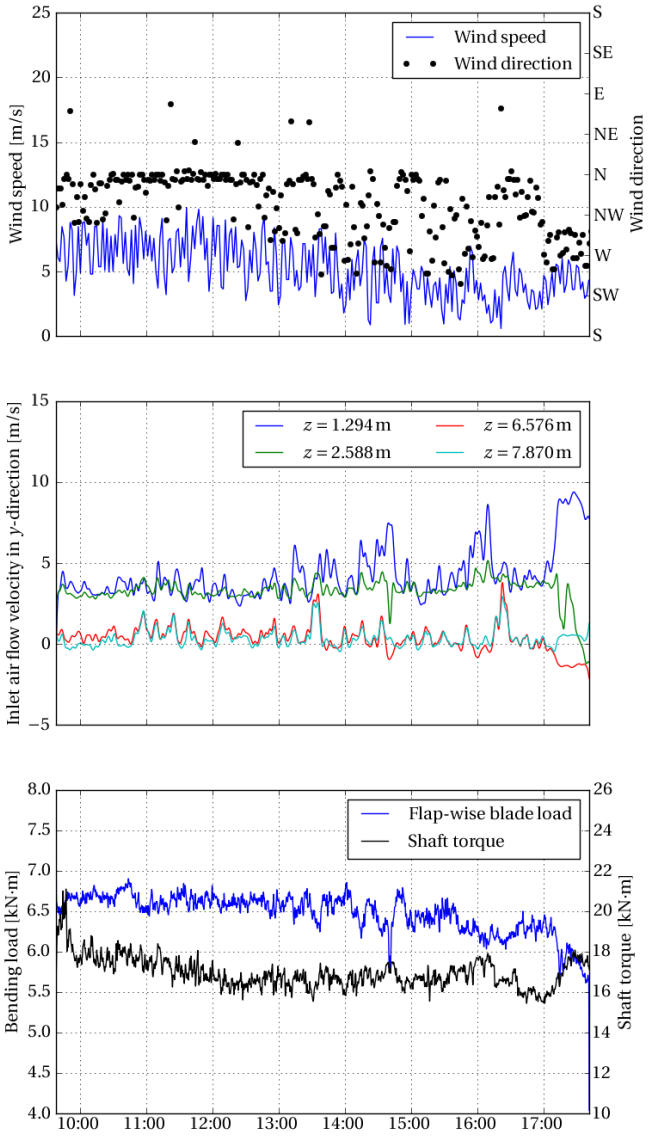

Figure 5.4: Measurements recorded on 20/11/2011

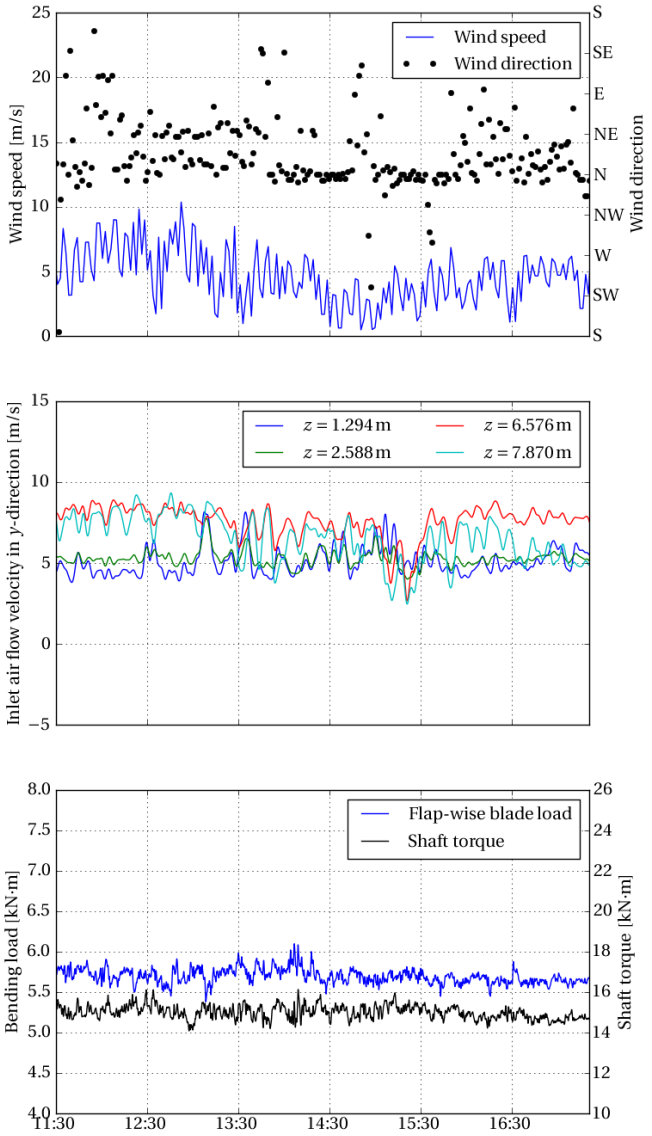

Figure 5.5: Measurements recorded on 21/11/2011

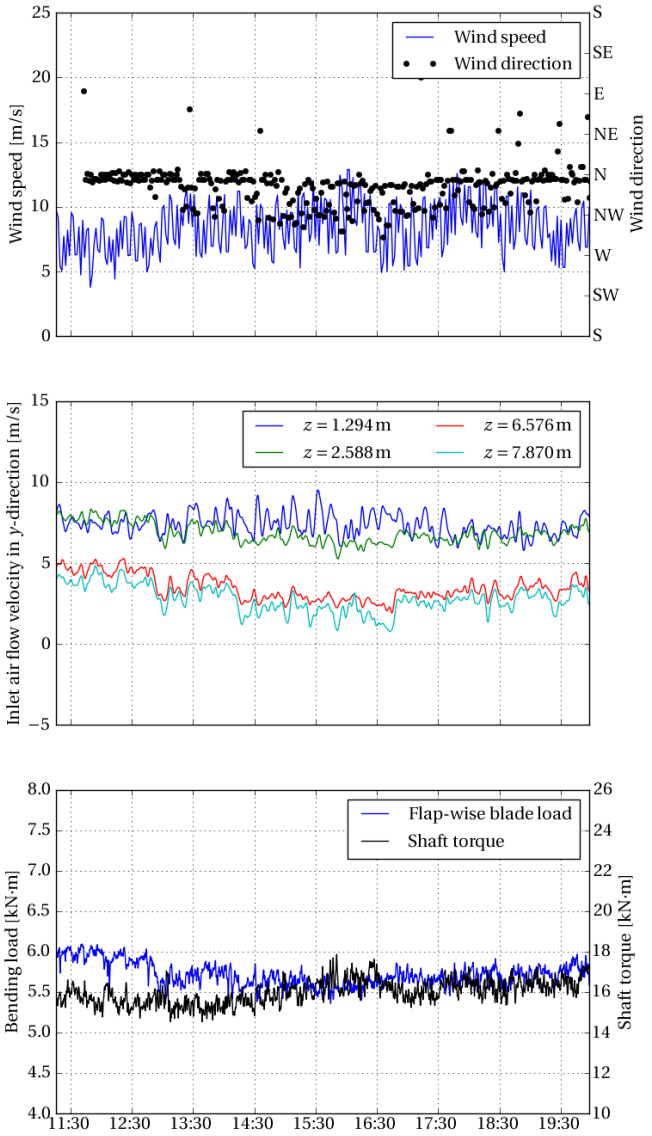

Figure 5.6: Measurements recorded on 22/11/2011

5.2 Fan inlet air flow temperatures

As described in Section 4.3, thermocouples were placed at the fan inlet to measure the temperature of the air entering the fan. Figure 5.7 shows the ambient air temperature measured on 19/11/2011 using the weather mast as well as the temperatures measured at each of the measurement stations situated at the fan inlet. The ambient temperature gradually increased to 34°C at 17:00 after which it suddenly dropped to 24°C. The measured temperatures exhibit a similar trend with a drop in temperature at 17:00. The temperatures measured at the fan inlet also showed a large number of spikes that do not follow a set pattern. These spikes can be attributed to momentary hot air recirculation as a result of the windy conditions. This assumption is further validated by the fact that the spikes occur more frequently when Westerly winds flatten the plume of hot air above the ACSC towards the peripheral side of the fan.

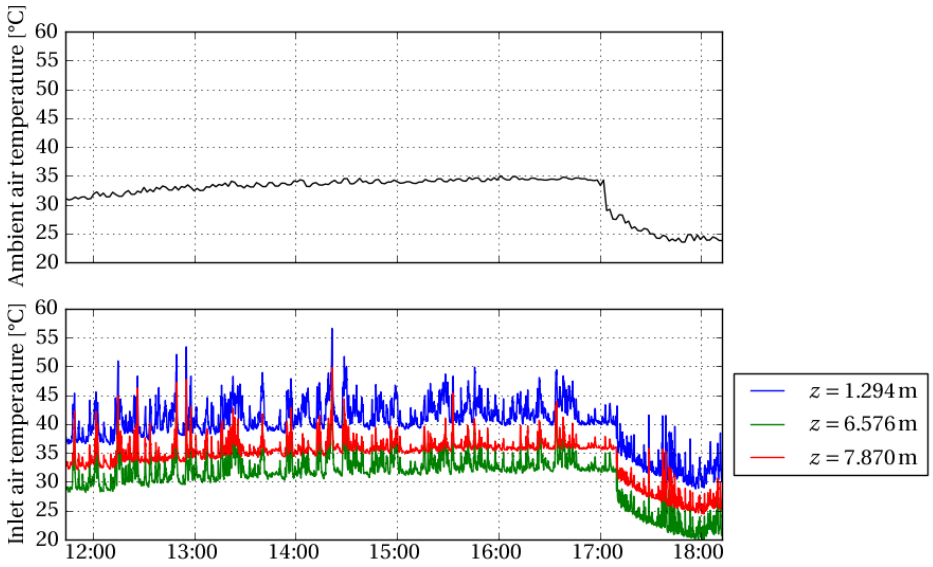

Figure 5.7: Temperature measurements recorded on 19/11/2011

Figure 5.8 shows the ambient air temperature and fan inlet air temperatures that were measured on 17/11/2011. The temperature spikes measured at the fan inlet were smaller than what was measured on 19/11/2011 which is due to the wind speed being lower on 17/11/2011 than on 19/11/2011. The wind speeds are shown in Figure 5.1 for 17/11/2011 and Figure 5.3 for 19/11/2011. As a result, it can be concluded that higher wind speeds cause increased hot air recirculation at the ACSC inlet. In addition to the increased hot air recirculation, one can see that the inlet air temperatures measured on the turbine side of the fan were lower than the temperatures measured on the peripheral side of the fan. This is also a result of the recirculation brought about by the windy conditions.

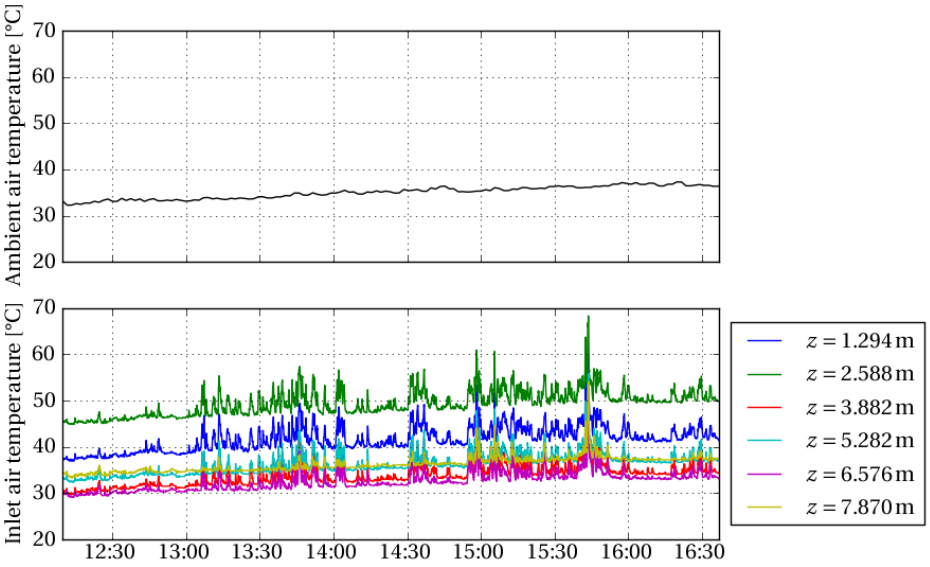

Figure 5.8: Temperature measurements recorded on 17/11/2011

5.3 Bundle outlet air flow velocities

The air flow exiting the plenum chamber through the heat exchanger bundles directly affects the performance of the ACSC. It is thus important to determine if a relationship exists between the wind conditions and the bundle outlet air flow.

On 19/11/2011 the air flow through the heat exchanger bundles were between 1 m/s and 3 m/s for most of the day with the sudden change in wind velocity and direction at 17:00, seen in Figure 5.3, causing a change in the bundle outlet air flow velocities. When the wind changed from a North-Westerly to an Easterly direction, the measured air flow velocities collapsed to approximately 2 m/s on both sides of the fan unit. Figure 5.9 shows the air flow through the Northern heat exchangers while Figure 5.10 shows the air flow through the heat exchangers on the Southern sides of the fan unit. The anemometer positions are indicated based on their distance from the peripheral side of the fan. Position 1 refers to the anemometer situated closest to the peripheral side of the fan while position 4 is closest to the turbine hall. The change in air flow through the bundles is due to their orientation and the fact that wind blowing from the East would be blowing parallel to the A-frame. As such, an Easterly wind would not cause any bias in air flow between the Southern and Northern side of the fan unit where the bundles are installed.

A second observation can be made on 20/11/2011 where, during the measurement period, the wind speed decreased from 7 m/s to 4 m/s, as can be seen in Figure 5.4. This drop in wind speed caused an increase in air flow through the bundles on both sides of the fan unit and can be seen in Figures B.25 and B.26. The assumption can therefore be made that air flow through the heat exchangers are higher on days with less wind. However, this conclusion does not tie up with the one made in Section 5.1 where higher winds caused increased air flow through the fan in the y-direction. The reason for this is that even though more air flows through the fan, the plenum chambers of 3 fans are

connected and as such the air flow between them is not isolated. In addition to this, the air flow was only measured at 4 positions on either side of the fan. Under certain circumstances the measurements recorded at these positions may not be indicative of the total air flow through the bundles.

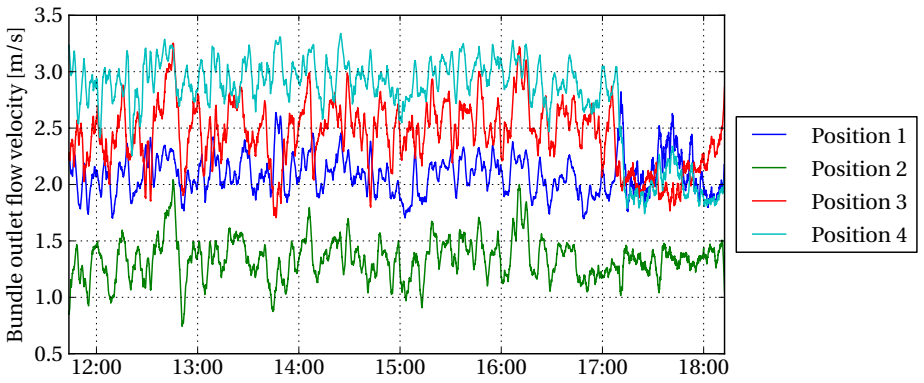

Figure 5.9: Air flow through Northern heat exchanger bundles on 19/11/2011

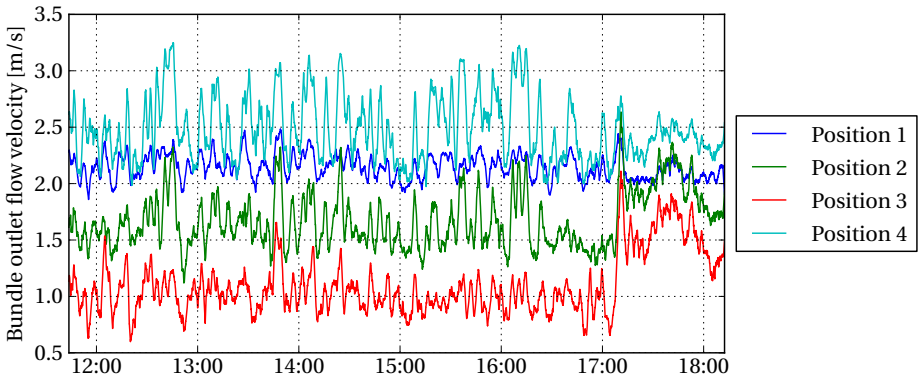

Figure 5.10: Air flow through Southern heat exchanger bundles on 19/11/2011

5.4 Fan blade loading

Fan blade loading is directly influenced by not only the volume flow rate of air through the fan but also the inflow conditions. Figure 5.11 is a graph created by Kröger (1994) which was obtained by testing a model fan and scaling the data. The graph shows the relationships between volume flow rate, fan static pressure, fan power consumption and efficiency. This data can be used to clarify any correlations between air flow and fan blade loading or fan shaft power. The graphs show that increased air flow results in decreased static pressure rise. Assuming that blade loading is proportional to fan static pressure rise, it may be concluded that increased air flow results in reduced blade loading.

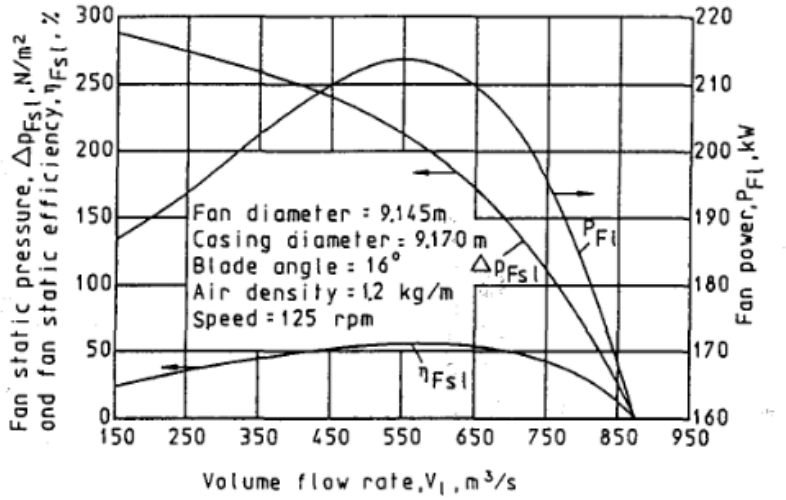

Figure 5.11: Fan performance curves described by Kröger (1994)

5.4.1 Average blade loading

Measurements taken on 19/11/2011 best represent the effect that increased air flow, shown in Figure 5.3, has on blade loading. The average loading conditions for the day are also shown in Figure 5.3 where the average loading in the flap-wise direction was 6 kN·m until approximately 17:00, after which it dropped to 5 kN·m. This drop in loading corresponds with the sudden increase in air flow at the same time. The running average of the blade loading is calculated by using a 30 s proportional scaling window. A Hamming window was used for this purpose. The air flow on 18/11/2011 exhibits a similar trend where during the course of the day the air flow through the fan gradually increased which caused a similarly gradual decrease in the average flap-wise blade loading. The air flow and blade loading on 18/11/2011 is presented in Figure 5.2.

It would appear as though the average flap-wise blade loading measured on 20/11/11 did not follow the same trend as described in the previous paragraph. The air flow through the fan on this day, as shown in Figure 5.4, remained constant while the blade loading, which can also be seen in Figure 5.4, gradually decreased. However, when considering the effect of the relatively high cross-flow in the x-direction (see Figure B.14), one can deduce that even though the air flow appeared to remain constant, it could possibly have been increasing at a location where air flow was not being measured. Cross-flow in the x-direction would shift the plane of symmetry of the inlet air flow field away from the line along which the anemometers were placed. This counter-intuitive phenomenon is also present in the data recorded on 22/11/2011. On this day the blade loading in the flap-wise direction, shown in Figure 5.6 underwent a gradual decrease until approximately 15:30 after which it started to increase again. The air flow into the fan, also shown in Figure 5.6,during this time exhibited the same trend while the cross-flow in both the x- and z-directions (Figure B.18 and Figure B.17, respectively) showed an increase until approximately 15:30, which was followed by a gradual decrease.

An approximation of the average blade loading can be calculated using the fan static pressure, p_s, to calculate the total aerodynamic force, F_t, exerted on the fan blades. Equation 5.1 presents this calculation with the outer diameter of the fan rotor $D = 9.145\,\text{m}$ and a fan static pressure of $p_s = 190\,\text{N/m}^2$. This value for static pressure has been measured in previous studies by Van Aarde (1990) and Venter (1990).

$$\begin{aligned} F_t &= p_s \times \pi \frac{D^2}{4} \\ &= 12.5\,\text{kN} \end{aligned} \tag{5.1}$$

Each of the fan blades is subjected to $\frac{1}{8}$ of the total load. As an approximation, it can be assumed that this load is applied at $\frac{2}{3}$ of the blade's length. The resultant bending load, M, experienced by each blade due to the static pressure rise over the fan is then

$$\begin{aligned} M &= \frac{F_t}{8} \times \frac{D}{2} \times \frac{2}{3} \\ &= 4.8\,\text{kN·m} \end{aligned} \tag{5.2}$$

This simple approximation of the blade loading as a result of the static pressure rise over the fan is considerably lower than the measured data. It is also lower than the value of 5723 N·m obtained numerically by (Bredell *et al.*, 2006*a*). As such it cannot be used as an accurate starting point when determining blade loading during a fan's design phase.

5.4.2 Blade loading amplitudes

Similarly to the mean blade load, the amplitude of the loading that the fan blade experiences also depends on the air flow into the fan. If the air flow is disturbed the aerodynamic forces exerted on the fan will vary depending on the blade's rotational position. This results in oscillating loading of the fan blade.

Figure 5.12 shows the bending data measured in the flap-wise direction on 18/11/2011. The loading amplitude varied between approximately 12 kN·m and -1 kN·m until 14:00 when the amplitude dropped to between 10 kN·m and 0 kN·m. This drop in blade load is

brought about by a reduction in cross-flow at the fan inlet. Figure B.9 shows the air flow measured in the z-direction on 18/11/2011. The air flow recorded at most of the measurement stations dropped to 0 m/s at 14:00 and again at 17:00. At both of these times the blade loading amplitude decreased and as such the conclusion can be made that the amplitude is a function of the cross-flow at the fan inlet in the z-direction.

Figure 5.13 shows the blade loading as measured on 20/11/2011. The loading amplitude during this time was approximately equal to the loading measured on 18/11/2011 before the drop in cross-flow. This amplitude was approximately the same over all the days that measurements were recorded.

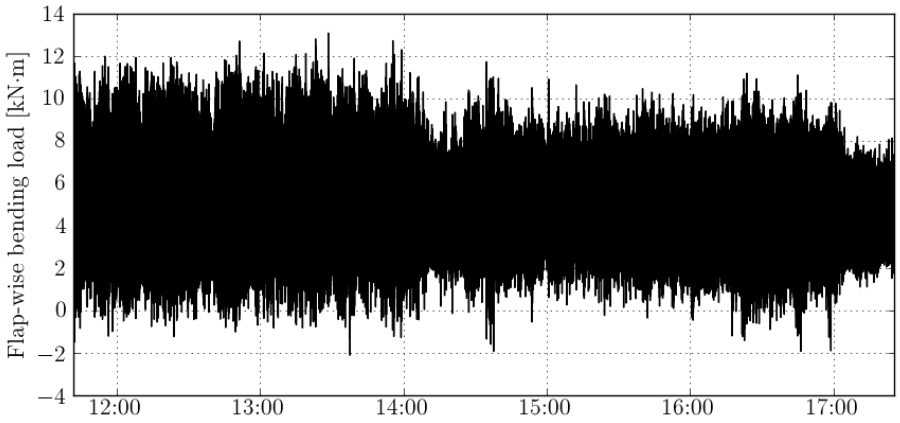

Figure 5.12: Flap-wise blade loading measured on 18/11/2011

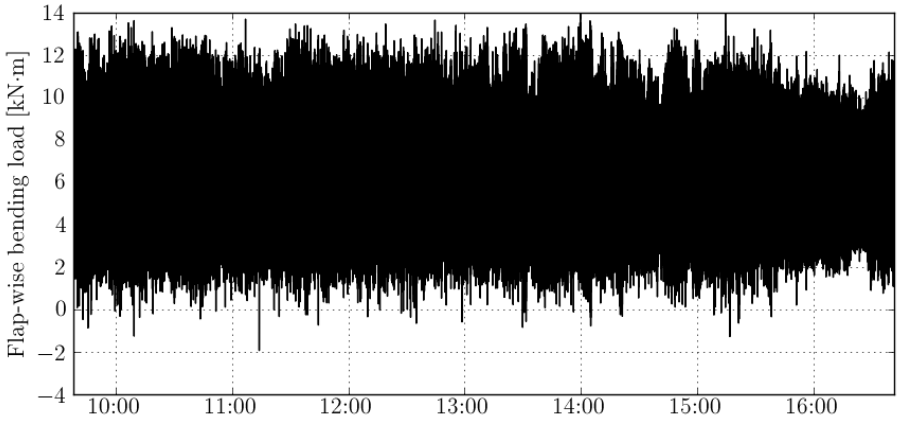

Figure 5.13: Flap-wise blade loading measured on 20/11/2011

5.4.3 Torque in blade neck

The torque exerted on the blade neck was measured with strain gauges that were calibrated in the Structures Laboratory at the University of Stellenbosch. This process is described in Section 4.1.2.2. Figure 5.14 shows the torque measured on 19/11/2011. The average torque is approximately 200 N·m with a maximum of 350 N·m. As was the case with the flap-wise blade loading discussed in Section 5.4.1, increased air flow after 17:00, shown in Figure 5.3 caused a decrease in blade loading.

The torque in the blade neck was higher on some of the other days that measurements were recorded. These measurements are presented in Appendix B.4 where one can see that the maximum torque in the blade neck is 400 N·m.

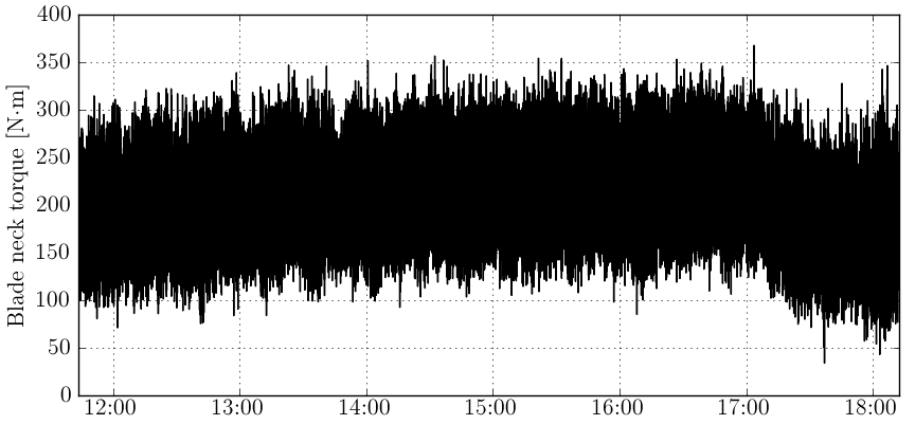

Figure 5.14: Blade neck torque measured on 19/11/2011

5.5 Gearbox loading

Similar to the effect of air flow on blade loading, Figure 5.11 shows that, if the fan is operating near maximum efficiency, increased air flow results in decreased fan power consumption. This lower power consumption means that there is less torque exerted on the fan shaft. However, if the air flow rate through the fan is lower than what is required to operate at maximum efficiency, any increase in air flow will cause an increase in shaft power and torque.

5.5.1 Shaft torque

Conversion from the measured torsional strain to shaft torque can be accomplished using the relationship between shear strain, γ, and shear stress, τ, with the torsional rigidity, G, of steel being 79.3 GPa according to Budynas and Nisbett (2008).

$$\tau = \gamma \times G \tag{5.3}$$

The torsional stress in the shaft is related to torque, Q, and the polar moment of inertia, J, with the following equation

$$\tau = \frac{Q\frac{d}{2}}{J} \tag{5.4}$$

where the polar moment of inertia is related to the diameter of the shaft, d,

$$J = \frac{\pi d^4}{32} \tag{5.5}$$

These equations can be combined to provide a relationship between the shaft torque, Q, and the measured shear strain, γ.

$$Q = \frac{\pi \gamma G d^3}{16} \tag{5.6}$$

Figure 5.2 shows the torsional moment exerted on the fan shaft on 18/11/2011. The approximate torque for the duration of the day was 16 000 N/m with sudden increases after 14:00 and 17:00. The air flow into the fan is shown in Figure 5.2 where one can see that the increased torque occurred at the same time as the air flow into the fan increased. Shaft torque measured on 19/11/2011 is presented in Figure 5.3 and shows an increase after 17:00. This increase in torque also coincided with the increase in air flow discussed in Section 5.1 and presented in Figure 5.3.

An approximation for the torque on the shaft can be determined using the fan shaft power and its rotational speed. Equation 5.7 provides a relationship between shaft torque, Q, shaft power, P, and rotational speed, N. The shaft power, P, of 200 kW was obtained from Figure 5.11. This value was chosen because it corresponds with a static pressure rise of approximately 190 Pa measured by Van Aarde (1990). The rotational speed, N, was measured to be 120 rpm instead of the theoretical value of 125 rpm shown in Figure 5.11. This minor discrepancy will have very little effect when considering the approximate nature and the purpose of the calculation being performed.

$$\begin{aligned} Q &= \frac{60000 \times P}{2\pi \times N} \\ &= \frac{60000 \times 200\,\text{kW}}{2\pi \times 120\,\text{rpm}} \\ &= 15.9\,\text{kN·m} \end{aligned} \tag{5.7}$$

This calculated torque of 15.9 kN·m is approximately equal to the average measured torque and as such the results obtained through this approximation are verified.

5.5.2 Shaft bending stresses

Bending stress, σ, is related to strain, ϵ, with the modulus of elasticity, E, by equation 5.8. For all of the calculations performed, the modulus of elasticity of $E = 207\,\text{GPa}$ was used according to Budynas and Nisbett (2008).

$$\sigma = E\epsilon \tag{5.8}$$

Figure 5.15 shows the bending stress experienced by the fan shaft in one of the two measured directions on 19/11/2011. The reason why only one of the two sets of data was plotted was because of the fact that when the data is viewed over a long time period, the recorded measurements appear to be exactly the same. The first observation regarding the measured stress is that there is a positive offset of approximately 30 MPa, which means that there is an imbalance in the fan rotor exerting a constant bending load on the fan shaft. The second observation is that the loading is not steady, but oscillates about the offset. The amplitude of oscillation also undergoes a sudden increase at 17:00, which coincides with the increase in air flow measured on the day. Fan rotors are generally balanced according the guidelines set forth by ISO 1940-1 (2003). However, over long periods of operation and maintenance slight imbalances could emerge.

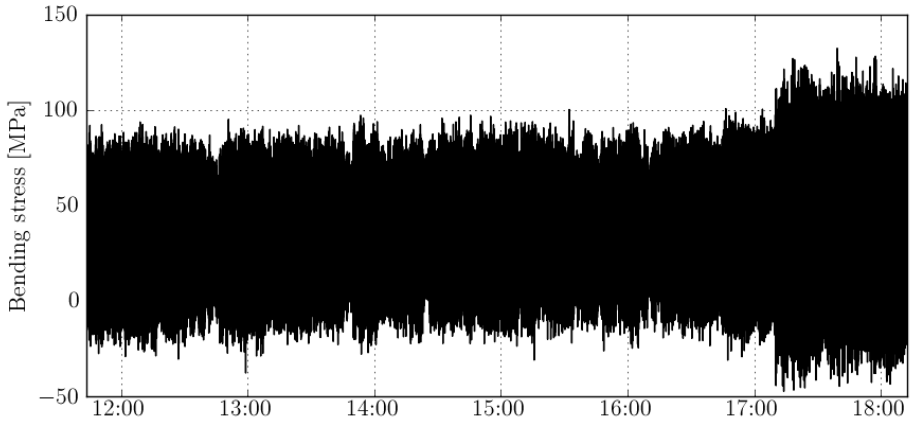

Figure 5.15: Shaft bending stress measured on 19/11/2011

The increase in the amplitude of oscillation of the shaft bending stress due to the increase in air flow leads to the conclusion that the cyclical bending load is as a result of the variation in aerodynamic loading exerted on the fan blades as they rotate. These cyclical loading patterns are further investigated as a function of the shaft's rotational position in Section 5.6.

5.6 Dynamic analysis of fan blade and gearbox loading

As the fan rotates, each fan blade experiences varying aerodynamic loading as a function of its position. Figure 5.16 shows the selected peripheral fan in a top view of the ACSC. The surrounding fan units are not illustrated, but are represented by the grey fill. Four blade azimuth positions are indicated on the figure with 0° at the edge of the ACSC and the angles measured in a clockwise direction. As in Figure 1.18, the x- and z-directions are shown as well as the orientation of the ACSC relative to North.

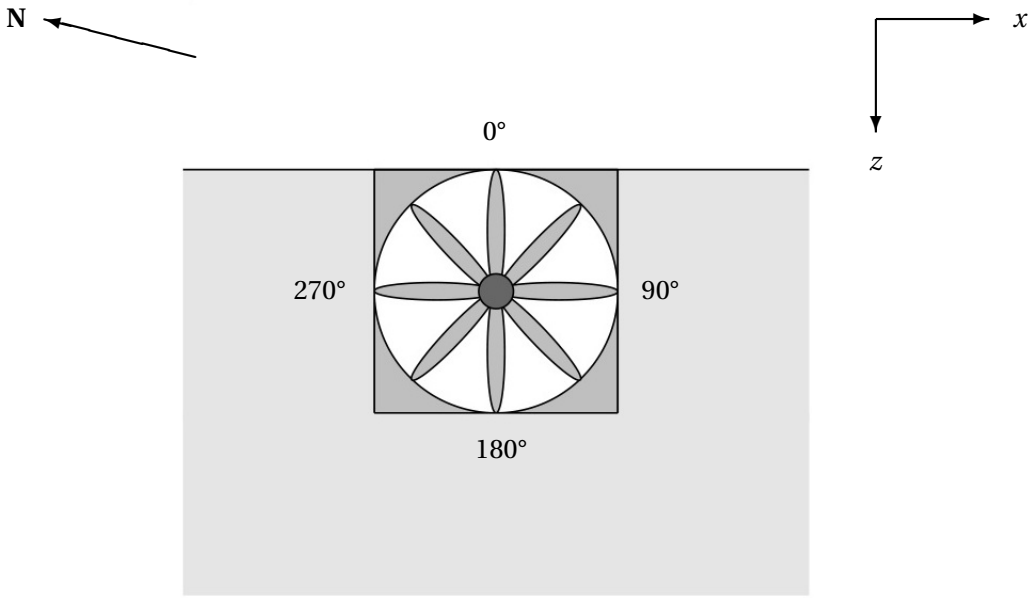

Figure 5.16: Fan blade positions

The data presented in Figure 5.17 is a combination of the measured blade loading in the flap-wise direction and the blade's rotational position that was recorded over a 2 s period on 19/11/2011. Each solid vertical line represents a point in time that a pulse was generated by the position sensor due to the fan blade passing the 0° position. From the recorded data it can be seen that the blade loading is cyclical. During each revolution, the fan blade experiences a peak bending load at the 0° position with two other peaks at appearing 90° and 225°. The fan rotates in a clockwise direction and it is expected that the loading between 0° and 180° should be lower than the loading between 180° and 360°. This is because the cross-flow at the fan inlet is generally in the positive z-direction. While the blade is between 0° and 180°, it is moving in the same direction as the air flow and when the blade is between 180° and 360° it is moving against the air flow. When the blade is moving against the air flow, there is a higher angle of attack over the blade which causes higher blade loading. This effect is shown in the measured data where it can be seen that the average blade loading increases as the blade completes a revolution.

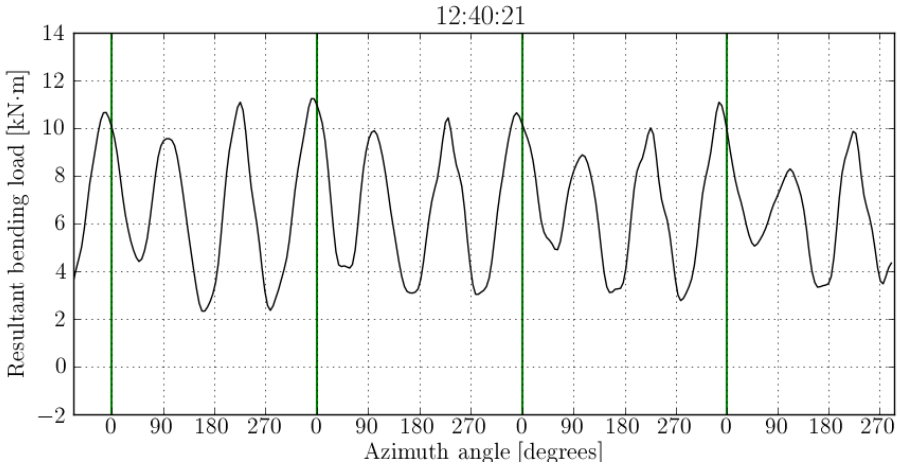

Figure 5.17: Fan blade loading as a function of its position recorded on 19/11/2011

Figure 5.18 shows an FFT of the blade loading data recorded on 19/11/2011. The dominant frequencies are 2 Hz, 4 Hz and 6 Hz. The 2 Hz frequency is approximately equal to the rotational frequency of the fan, Ω, while the frequency at 4 Hz is the frequency at which the blade passes underneath the fan bridge. The frequency at 2 Hz can be attributed to the aforementioned once-per-revolution load variation exerted on the fan blade as it rotates. The frequency at 6 Hz can be attributed to the blade's natural frequency, ω_n, of approximately 5.4 Hz. A higher natural frequency is measured while the blade is rotating due to centrifugal stiffening. When considering the measured data, it can be seen that the dominant vibration is as a result of the blade oscillating at its own natural frequency.

According to the standards set forth in ISO 13706 (2001), the natural frequency of the fan or fan components are not allowed to be within 10% of the blade passing frequency. On an 8 bladed fan running at approximately 2 Hz the blade passing frequency is equal to 16 Hz and as such there is no danger.

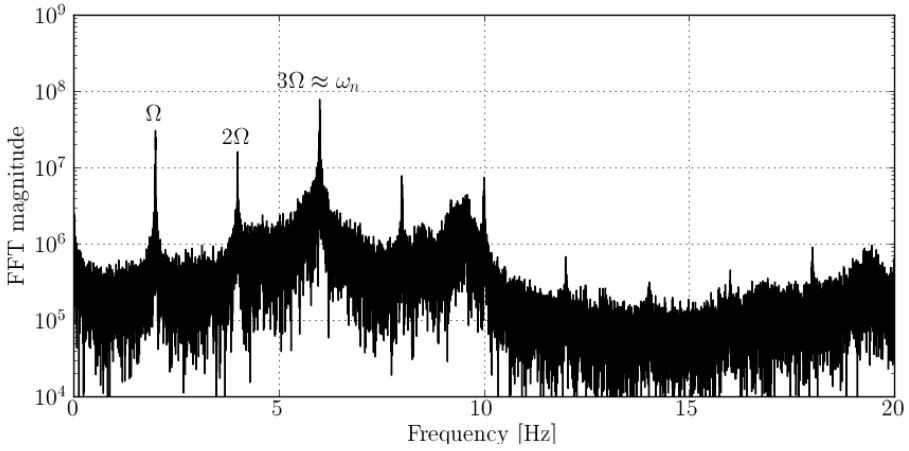

Figure 5.18: FFT of flap-wise fan blade loading recorded on 19/11/2011

The bending stress exerted on the fan shaft which was measured on 18/11/2011 is shown in Figure 5.19. The pulses generated by the position sensor have been included to provide an indication of fan shaft position for the stress measurements. The stresses measured by both orthogonally positioned strain gauge bridges are shown and it is clear that they both exhibit the same pattern. Each strain gauge channel shows stress oscillations with a frequency of approximately 2 Hz. This, and the fact that the peaks of the two separate channels are lagging each other by 90°, indicates that there is a once-per-revolution bending load exerted on the shaft.

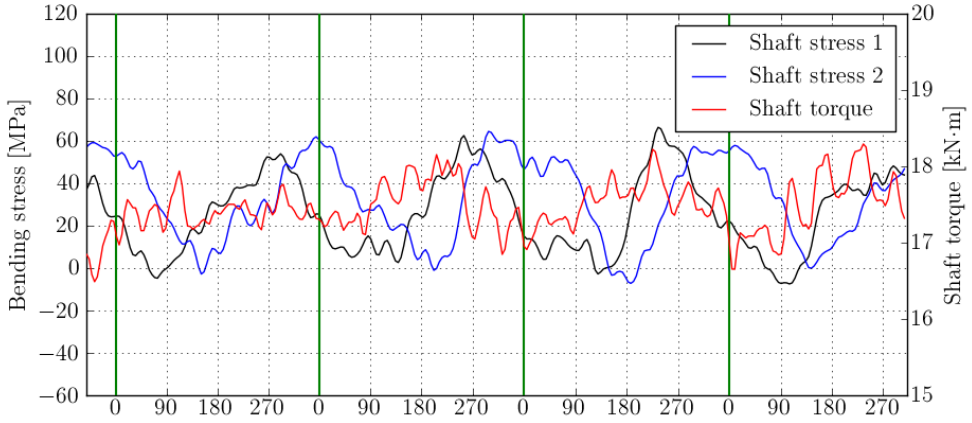

Figure 5.19: Shaft stresses and torque recorded on 18/11/2011 as a function of fan blade position

Figure 5.20 shows an FFT of the shaft bending stress measurements taken on 19/11/2011. As expected, the dominant frequency is the fan rotational frequency of 2 Hz. This frequency analysis reiterates the fact that the dominant bending load exerted on the fan shaft is due to a once-per-revolution force.

In addition to the bending stresses exerted on the fan shaft, Figure 5.19 also presents the shaft torque measured on 18/11/2011. The shaft torque also oscillates at approximately 2 Hz with a higher-order vibration superimposed on the primary loading curve.

Figure 5.21 shows an FFT of the shaft torque measured on 18/11/2011. As with the shaft bending stress, there is only one dominant frequency at the approximate fan rotational frequency of 2 Hz.

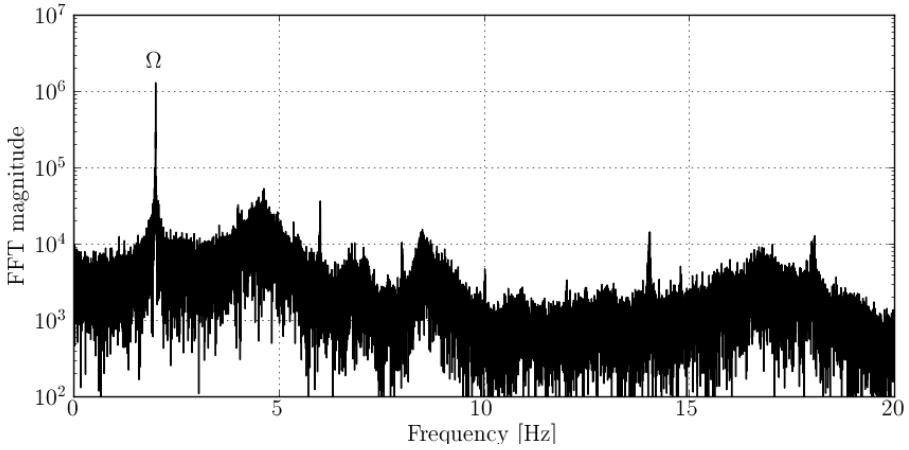

Figure 5.20: FFT of shaft bending stresses measured on 18/11/2011

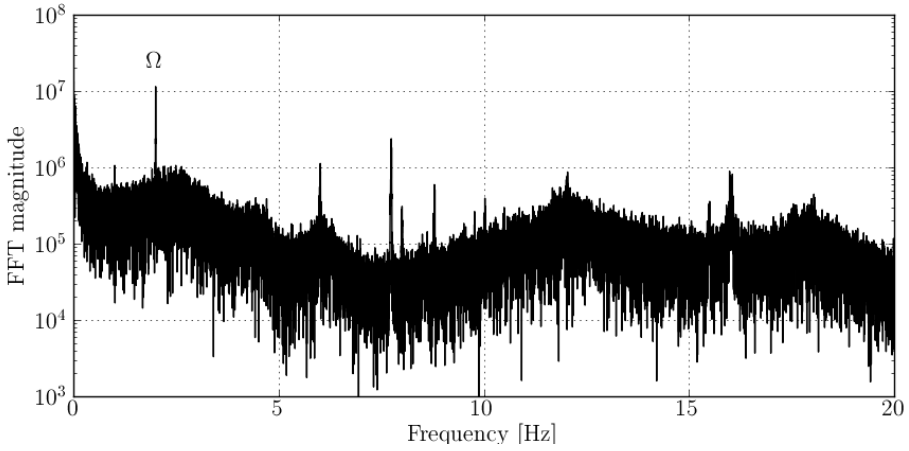

Figure 5.21: FFT of shaft torque measured on 18/11/2011

5.7 Start-up analysis

Every time the fan is started after being shut down for maintenance or testing, large forces are exerted on the fan blades and shaft. Figure 5.22 shows the shaft torque (top) and rotor speed (bottom) measured on 21/11/2011. After the large initial torque spike of approximately 40 kN·m, the torsion on the shaft dropped to its normal operating magnitude of approximately 13 kN·m. It can be seen that the fan speed increases rapidly after being started and reaches its operating speed of 120 rpm after approximately 4.5 s.

Each point on the bottom graph, which depicts the fan's rotational speed, represents the average speed during one complete rotation of the fan rotor. As described in Section 5.6, the solid vertical lines on the torque graph indicate the times at which the fan

blade being monitored passed the 0° position. This data was used to determine the fan rotor's average rotational speed during each complete revolution. The large initial spike in torque and the subsequent vibration is damped out in approximately 1 s. A second increase in shaft torque can be seen at the point where the fan reaches its operating speed. Figure 5.23 depicts the torque vs. speed curve of a typical induction motor which shows that the second torque peak in the measured data corresponds with the peak in torque experienced by the motor as it approaches zero slip between the stator and rotor at synchronous speed. The acceleration is caused by the difference in the motor and fan torque with the system settling at the point where the two torque curves intersect. At this point the motor can no longer accelerate because it does not have sufficient torque to overcome the load requirements.

Start-up loading was also recorded on 22/11/2011 and exhibits the same trend as was seen on 21/11/2011. The start-up data for 22/11/2011 is shown in Figure B.60.

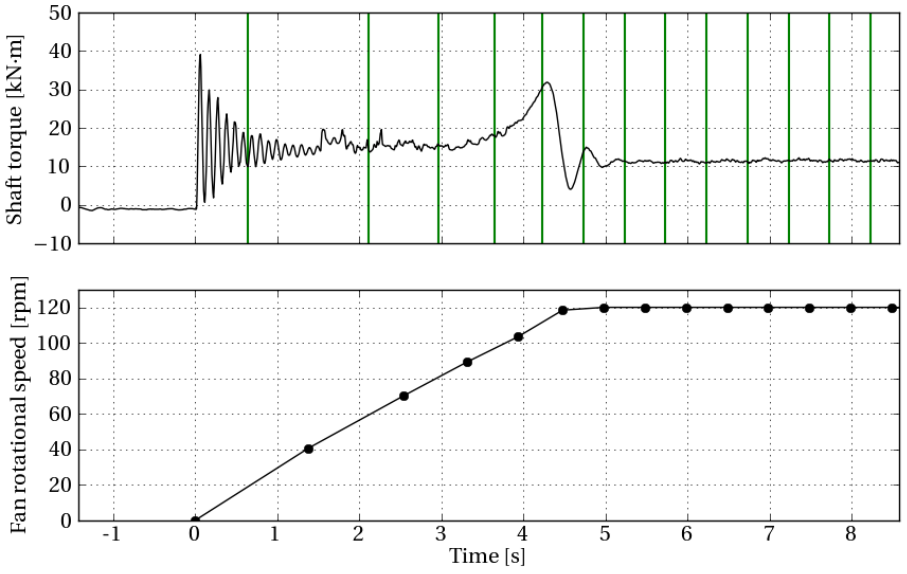

Figure 5.22: Shaft torque during fan start-up on 21/11/2011

5.8 Extraction of aerodynamic loading from measured data

Work done by Bredell *et al.* (2006*a*) has shown that cross-flow at the fan inlet causes a variation in the aerodynamic load exerted on the fan blade as it rotates. These results were previously mentioned in Section 1.4 and is shown in Figure 5.24. A CFD model was used in conjunction with the lift and drag characteristics of the fan blade to determine, numerically, the resultant bending moment exerted on it as a function of its azimuth position. It was found that the fan blade experiences an increase in blade loading of approximately 20% as it approaches the windward side of the fan.

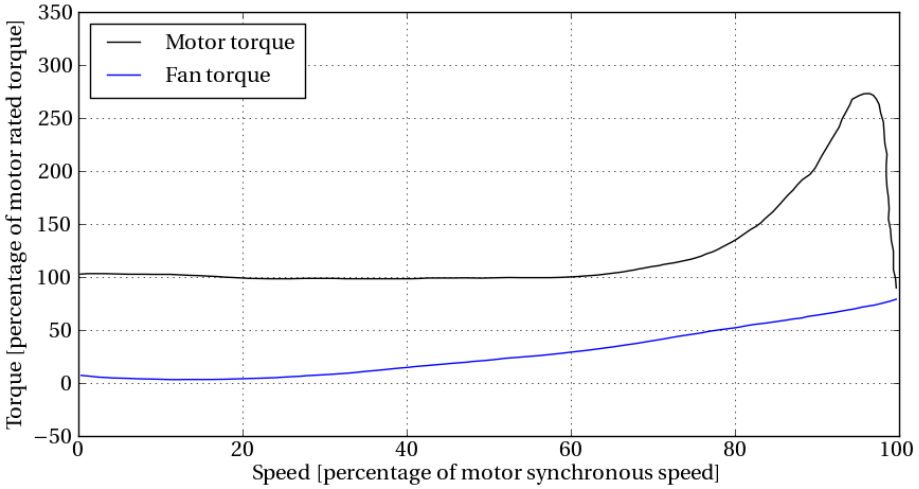

Figure 5.23: Typical torque vs. speed curve for a three phase induction motor and fan

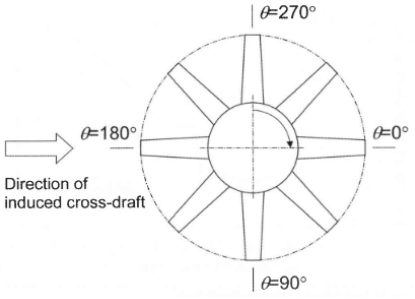

(a) Azimuth angle describing rotational position of blade

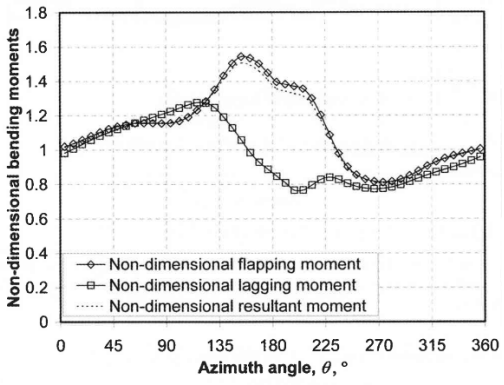

(b) Bending moments exerted on blade at a high platform height

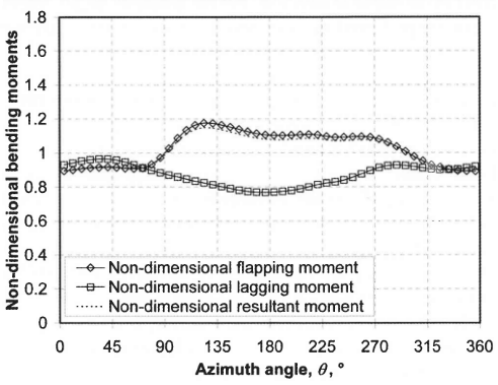

(c) Bending moments exerted on blade at a low platform height

Figure 5.24: Fan blade loading as a function of its position as researched by Bredell *et al.* (2006*a*)

It was decided to determine whether any correlations exist between the numerical work conducted by Bredell *et al.* (2006*a*) and the current experimental work. To do this, the approximate aerodynamic loading exerted on the fan blade was extracted from the total measured loading. In its simplest form, the total bending load exerted on the blade, $M(t)$, consists of a sinusoidal function representing the free vibration of the blade, superimposed on an additional function, $H(t)$, which represents the aerodynamic loading. This relationship is presented in equation 5.9. This procedure theoretically has the same effect as incorporating a band-rejection filter, but can be explained in physical terms instead.

$$M(t) = A\sin(\omega_n t + \phi) + H(t) \tag{5.9}$$

Figure 5.25 presents the total resultant blade loading measured at approximately 12:40 on 19/11/2011. The azimuth positions on the x-axis of the graph coincide with those described by Figure 5.16. A sinusoidal curve was fitted to the data and can also be seen in this figure. Subtracting the sinusoidal curve from the measured data, but retaining the offset, yields the aerodynamic load exerted on the fan blade as a function of its rotational position. The resultant aerodynamic load obtained in this way is comparable to the results obtained by Bredell *et al.* (2006*a*), which is shown in Figure 5.24. However, the aerodynamic load extracted from the measured data exhibits an additional blade loading peak when compared to the numerical results. The first peak is at the 0° position, which is at the windward/peripheral side of the fan. The second peak appears close to the 180° position, which is where the blade passes beneath the fan bridge for the second time (the first time being at 0°). As discussed in Section 3.4, one expects an increase in aerodynamic loading due to the high pressure zone located between the bridge and fan. The results obtained by Bredell *et al.* (2006*a*) do not exhibit the second peak, because the influence of the fan bridge was not considered.

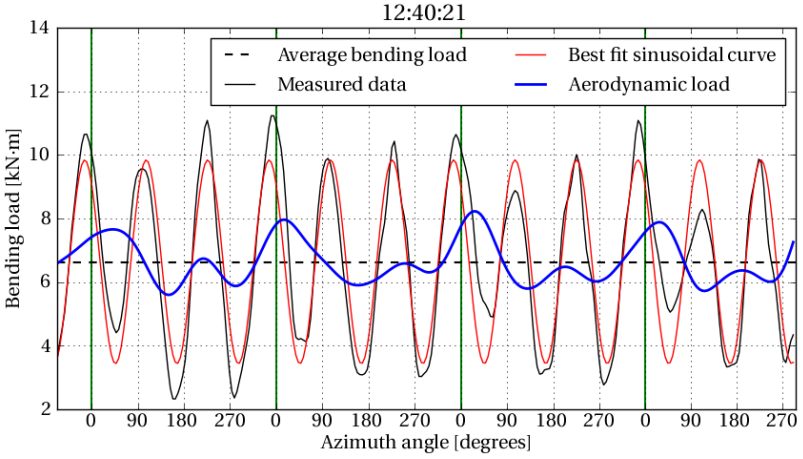

Figure 5.25: Extraction of aerodynamic loading from the measurements of 19/11/2011

The aerodynamic loading exerted on the fan blade was also extracted for the measurements recorded on 22/11/2011. This information is shown in Figure 5.26. The air flow velocities into the fan on 22/11/2011 and 19/11/2011 can be seen in Figure 5.6 and

Figure 5.3, respectively. One can see that, as described in Section 5.1, the average aerodynamic load on the blade is lower on 22/11/2011 than on 19/11/2011 due to the increased air flow through the fan. In addition to the difference in magnitude, the loading patterns also vary. On 22/11/2011 the peaks of the aerodynamic loading are not as pronounced as on 19/11/11. The reason for this is that the air flow measured in the z-direction on 22/11/11, shown in Figure B.17, was higher than the same air flow velocities measured on 19/11/11 and shown in Figure B.11. This finding correlates with the results obtained by Bredell *et al.* (2006*a*) when lowering the fan platform height of the numerical model. By lowering the platform height, the cross-flow is increased due to the smaller cross-sectional area underneath the ACSC. Figure 5.24c shows how the peak aerodynamic load has a flatter shape when compared to the results obtained at a higher platform height.

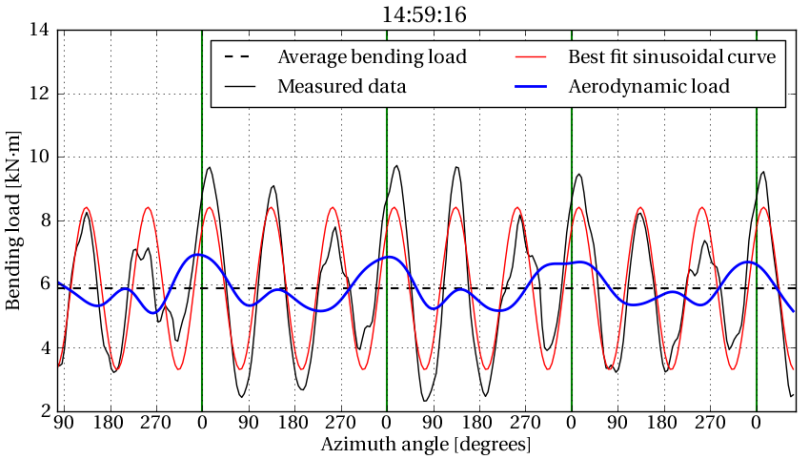

Figure 5.26: Extraction of aerodynamic loading from the measurements of 22/11/2011

Chapter 6

Conclusion and recommendations

The objective of this study was to develop a system that could simultaneously measure the inlet air flow and mechanical loading on the fan rotor and gearbox. The system would then be used to record measurements for a variety of wind conditions. These measurements could then be used to determine and analyse relationships between wind conditions, air flow, and the fan blade and gearbox loading.

6.1 Data capturing system

Data had to be captured from the rotating fan assembly as well as the stationary sensors positioned on the safety grid below the fan. Measurements taken on the rotating fan were captured by two wireless MicroStrain V-Link units while the rest of the measurements were captured by two HBM QuantumX MX1601 units. The data was recorded and synchronised by a single HBM QuantumX CX22W data recorder, which was accessed via a laptop connected to the system wirelessly. This system performed well, and successfully captured data over the 8 day measurement period.

6.2 Measurements recorded

Measurements were recorded from an array of sensors and weather mast located on-site over a period of 8 days in November 2011. A number of relationships between the wind conditions, air flow, and fan blade and gearbox loading were identified and discussed in Chapter 5.

6.2.1 Air flow at fan inlet

Ultrasonic and propeller anemometers were installed below the fan, on top of the safety grid. This array of sensors was used to measure the air flow at the fan inlet while a number of propeller anemometers were used to measure the air flow at the heat exchanger bundle outlets. This combination of sensors was tested before installation at the full-scale facility, and provided all of the required measurements.

It was found that the air flow through the fan was closely related to the wind speed and direction in the following ways:

1. Winds blowing from the West caused higher air flow through the peripheral side of the fan while winds blowing from the East resulted in higher air flow on the turbine side of the fan.

2. Air flow through the fan was higher on days where the wind was blowing from the East than on days that the wind was blowing from the West.

It was difficult to compare the measurements recorded during this project to those recorded by Van Aarde (1990), because his measurements were not taken at the same location within the ACSC. In addition to this, the weather conditions obtained during the two experiments that were conducted at the edge of the ACSC were not the same as those recorded for this project. However, the measurements recorded by Van Aarde (1990) also showed that the air flow into the fan was higher on days that the wind was blowing from the East.

6.2.2 Fan blade loading

Strain gauges were used to determine the fan blade and shaft loading. The adverse conditions at the fan caused a number of difficulties during gauge installation. The strain gauges would often tear when soldering wires onto the delicate gauge tabs due to the high wind speeds. This problem was solved by thoroughly preparing the gauges on a piece of glass before installation at the ACSC. By preparing the gauges beforehand, no delicate soldering work had to be performed at the fan. It is recommended that a similar approach be followed for any further studies.

The blade bending load was measured in the flap- and lag-wise directions. Average blade loading was calculated for each of the 8 measurement days where it was found to vary between 5 kN·m and 6.5 kN·m, depending on the inlet air flow conditions. Higher air flow velocities in the axial direction of the fan resulted in lower flap-wise bending loads. The reason for this is that the fan static pressure, which can be assumed to be proportional to the flap-wise blade loading, decreases with increasing air flow through the fan.

Through analyses of the fan blade's vibration, it was discovered that the blade loading is cyclical and that it vibrates at its own natural frequency of approximately 6 Hz. A second dominant loading frequency was found at the rotational frequency of the fan, which is a result of the blade experiencing changes in aerodynamic loading as it rotates.

The blade loading amplitudes remained between 0 kN·m and 14 kN·m for all of the measurement days. However, a reduction in cross-flow at the fan inlet caused the blade loading amplitudes to decrease. This is due to the variation in the angle of attack over the fan blade decreasing with a reduction in cross-flow velocity.

6.2.3 Forces exerted on the gearbox

Torsional loading on the low-speed shaft was approximately equal to the torque calculated from the fan shaft power. Start-up torque was approximately 150% higher than the steady-state torque. If the fan is stopped and started often, this large torsional load may lead to fatigue damage and eventual shaft failure.

In addition to this, the bending stresses and torque exerted on the fan shaft was found to be cyclical and at the same frequency as the rotational frequency of the fan. These cyclical loads could lead to bearing wear or fatigue damage to the shaft itself. A probable cause of a cyclical load is an unbalanced force, such as an unbalanced fan rotor or varying aerodynamic loading.

6.3 Recommendations for future work

6.3.1 Experimental technique

In order to draw definitive conclusions regarding the effect that wind has on the air flow at the fan inlet, further measurements need to be recorded over a much longer period of time. Recording measurements over a period of several months would allow for a much greater variety in ambient conditions but also the opportunity to ascertain whether inlet flow conditions are repeated with similar wind patterns.

6.3.2 Measurement equipment

Shortcomings regarding the measurement equipment also had an influence on the measurements that were taken. Fan inlet conditions could only be measured at 6 locations. For a more definitive result a much finer measurement resolution is required. However, a larger number of sensors not only increases the cost of the measurement system, but would also require more data acquisition hardware. As such, experiments with more sensors would have to be performed in future projects.

6.3.3 Data capturing system

The data capturing system was able to record measurements autonomously for as many hours as the V-Link batteries remained charged. The V-Link units, once fully charged, could capture measurements for approximately 8-10 hours. As such, the batteries had to be charged on a daily basis, which required that the fan be switched off. This was an inconvenience and is not always practically possible. The V-Link units were ordered with additional battery capacity in an optional enclosure shown in Figure 6.1. However, these were not available before the measurement period and could not be used during this investigation. An alternative solution would be to use slip-rings to transfer power to the V-link units while still using the wireless capabilities for data transmission.

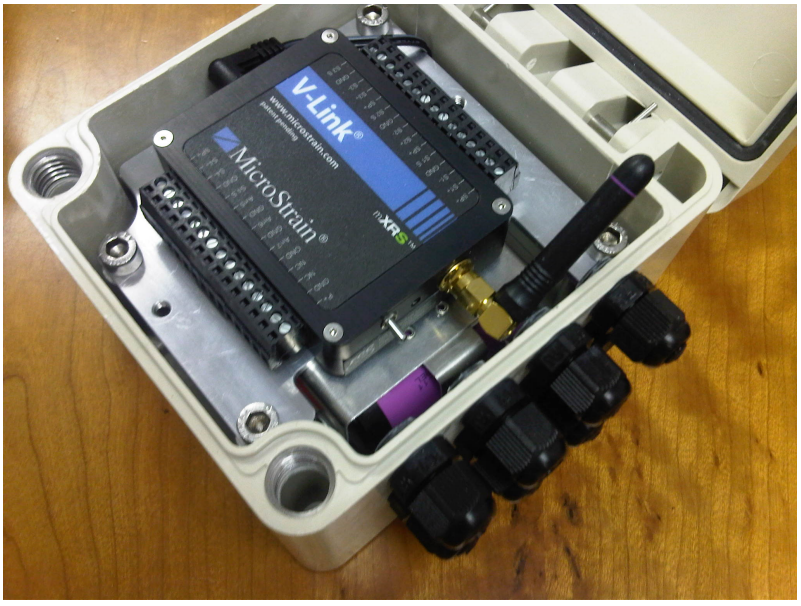

Figure 6.1: V-Link with optional enclosure and additional batteries

6.3.4 Vibration measurements

The purpose of the current investigation was to develop a system that could measure fan blade and shaft loading. However, ISO 13706 (2001) provides limits for the maximum allowable vibration displacement and velocity of structural members and shaft bearings, respectively. The maximum allowable displacement for structural members is 0.15 mm, peak to peak, while the vibrational velocity measured on the bearings perpendicular to the fan shaft centreline must not exceed 6.3 mm/s. It is also specified that the wind speed during testing is not to exceed 5 m/s. To perform these measurements accelerometers would need to be installed and as such was not part of the current study, but should be considered when performing any future work.

6.3.5 Numerical analysis of fan blade loading and vibration

Finally, further numerical work is warranted considering that the numerical investigation conducted by Bredell *et al.* (2006*a*) provided an accurate representation of the aerodynamic loading extracted from the measured data. Future numerical work could possibly include the effect of the fan bridge and be coupled with a multi-body dynamics simulation in order to determine the effect that aerodynamic loading has on the vibration of the fan blades. The measured data in this investigation would then provide validation of any numerical models.

References

Al-Bedoor, B., Al-Nassar, Y., Ghouti, L., Adewusi, S. and Abdlsamad, M. (2004). Shaft lateral and torsional vibration responses to blade(s) random vibration excitation. *The Arabian Journal for Science and Engineering*, vol. 29, pp. 39–67.

Bredell, J., Kröger, D. and Thiart, G. (2006*a*). Numerical investigation into aerodynamic blade loading in large axial flow fans operating under distorted inflow conditions. *R & D Journal, of the South African Institution of Mechanical Engineering*, vol. 22, pp. 11–17.

Bredell, J., Kröger, D. and Thiart, G. (2006*b*). Numerical investigation of fan performance in a forced draft air-cooled steam condenser. *Applied Thermal Engineering*, vol. 26, pp. 846–852.

Budynas, R.G. and Nisbett, J.K. (2008). *Shigley's Mechanical Engineering Design*. 8th edn. McGraw-Hill, New York.

Duvenhage, K., Vermeulen, J. and C.J. Meyer, D.K. (1996). Flow distortions at the fan inlet of forced-draught air-cooled heat exchangers. *Applied Thermal Engineering*, vol. 16, pp. 741–752.

Hotchkiss, P., Meyer, C. and von Backström, T. (2006). Numerical investigation into the effect of cross-flow on the performance of axial flow fans in forced draught air-cooled heat exchangers. *Applied Thermal Engineering*, vol. 26, pp. 200–208.

ISO 13706 (2001). Petroleum, petrochemical and natural gas industries – air-cooled heat exchangers.

ISO 1940-1 (2003). Mechanical vibration – balance quality requirements for rotors in a constant (rigid) state – part 1: Specification and verification of balance tolerances.

Kröger, D. (1994). Fan performance in air-cooled steam condensers. *Heat Recovery Systems & CHP*, vol. 4, pp. 391–399.

Kröger, D.G. (2004). *Air-cooled Heat Exchangers and Cooling Towers*. Penwell Corp., Tulsa.

Meirovitch, L. (2001). *Fundementals of Vibrations*. McGraw-Hill, New York.

Meyer, C. (2005). Numerical investigation of the effect of inlet flow distortions on forced draught air-cooled heat exchanger performance. *Applied Thermal Engineering*, vol. 25, pp. 1634–1649.

Meyer, C. and Kröger, D. (2001). Numerical investigation of the flow field in the vicinity of an axial flow fan. *International Journal for Numerical Methods in Fluids*, vol. 36, pp. 947–969.

Pierce, W.T. (2008). *Evaluation and performance prediction of a wind turbine blade*. Master's thesis, Department of Mechanical and Mechatronic Engineering, University of Stellenbosch, South Africa.

Salta, C. and Kröger, D. (1995). Effect of inlet flow distortions on fan performance in forced draught air-cooled heat exchangers. *Heat Recovery Systems & CHP*, vol. 15, pp. 555–561.

Simms, D., Hand, M., Fingersh, L. and Jager, D. (1999). Unsteady aerodynamics experiment phases II-IV test configurations and available data campaigns. Tech. Rep., National Renewable Energy Laboratory.

Stinnes, W. (1998). *The Performance of Axial Fans Subjected to Forced Cross-Flow at Inlet*. Master's thesis, Department of Mechanical and Mechatronic Engineering, University of Stellenbosch, South Africa.

Stinnes, W. and Von Backström, T. (2002). Effect of cross-flow on the performance of air-cooled heat exchanger fans. *Applied Thermal Engineering*, vol. 22, pp. 1403–1415.

Swiegers, J. (1989). *Structural optimisation of a composite material fan blade using the finite element method*. Master's thesis, Department of Mechanical and Mechatronic Engineering, University of Stellenbosch, South Africa.

Thiart, G. (1990). *A Numerical Procedure for Predicting the Effects of Distorted Inflow Conditions on the Performance of Axial Flow Fans*. Ph.D. thesis, Department of Mechanical and Mechatronic Engineering, University of Stellenbosch, South Africa.

Thiart, G. and Von Backström, T. (1993). Numerical simulation of the flow field near an axial flow fan operating under distorted inflow conditions. *Journal of Wind Engineering and Industrial Aerodynamics*, vol. 45, pp. 189–214.

Van Aarde, D. (1990). *Vloeiverliese deur 'n A-raam vinbuisbundel in 'n lugverkoelde kondensator*. Master's thesis, Department of Mechanical and Mechatronic Engineering, University of Stellenbosch, South Africa.

Van der Spek, H. (2003). Vibration control: New fan blade tip reduces pulsation. In: *Cooling Technology Institute Annual Conference*.

Van der Spuy, S.J., Von Backström, T.W. and Kröger, D.G. (2009). An evaluation of simplified methods to model the perormance of axial flow fan arrays. *R & D Journal, of the South African Institution of Mechanical Engineering*, vol. 26, pp. 12–20.

Van Rooyen, J. (2007). *Performance trends of an air-cooled steam condenser under windy conditions*. Master's thesis, Department of Mechanical and Mechatronic Engineering, University of Stellenbosch, South Africa.

Venter, S. (1990). *The Effectiveness of Axial Flow Fans in A-Frame Plenums.* Ph.D. thesis, Department of Mechanical and Mechatronic Engineering, University of Stellenbosch, South Africa.

Wauben, W.M. (2005). Wind tunnel and field tests of three 2d sonic anemometers. Tech. Rep., Royal Netherlands Meteorological Institute.

Xu, C., Amano, R.S. and Lee, E.K. (2004). Investigation of an axial fan - blade stress and vibration due to aerodynamic pressure field and centrifugal effects. *JSME: International Journal*, vol. 47, pp. 75–90.

Zapke, A. (1997). *Characteristics of gas-liquid counterflow in inclined ducts with particular reference to reflux condensers.* Ph.D. thesis, Department of Mechanical and Mechatronic Engineering, University of Stellenbosch, South Africa.

Appendix A

Anemometer test results

This chapter provides the graphs for the ultrasonic and propeller anemometer test results that were not included in Section 3.1 and Section 3.2. Discussions of the results obtained are also provided.

A.1 Ultrasonic anemometer test results

In order to determine the out-of-plane air flow velocity measurement limits of the ultrasonic anemometers being used for this investigation, a single anemometer was placed in a wind tunnel and set at a specific angle with respect to the horizontal. By adjusting the angle of the anemometer, the incoming air flow angle, α, was increased from 0° to 70° in increments of 10°. For each air flow angle the fan speed was increased from 5 Hz to 50 Hz in 5 Hz increments. This procedure is documented in Section 3.1 and the figures in this section present the air flow velocity measured by the ultrasonic anemometer for each combination of air flow angle and fan rotational speed. The test results indicated that the anemometers are capable of measuring the air flow velocity up to an out-of-plane flow angle of approximately $\alpha = 40°$.

Figure A.1, Figure A.2 and Figure A.3 shows the results obtained with the anemometer orientated in such a way to create an out-of-plane flow angle of $\alpha = 10°$, $\alpha = 20°$ and $\alpha = 30°$, respectively. These graphs show that, for low out-of-plane air flow angles, the anemometer measures only the component of air flow in its plane of measurement.

Figure A.1 and Figure A.1 shows the results obtained when the ultrasonic anemometer was set at an angle of $\alpha = 50°$ and $\alpha = 70°$. These graphs indicate that when the out-of-plane air flow angle exceeds the threshold of approximately $\alpha = 40°$, the air flow velocity measured by the ultrasonic anemometer is significantly lower than the component of air flow velocity in the plane of measurement. The reason for this is that the air becomes obstructed by the dome above the measurement probes.

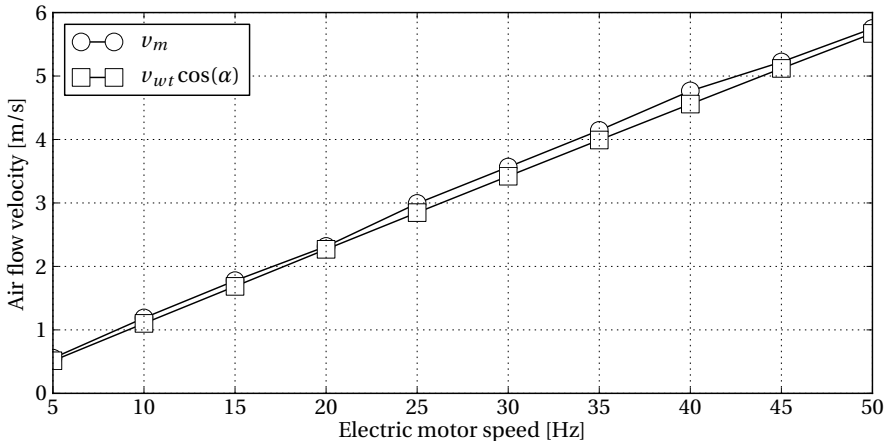

Figure A.1: Ultrasonic anemometer test results for $\alpha = 10°$

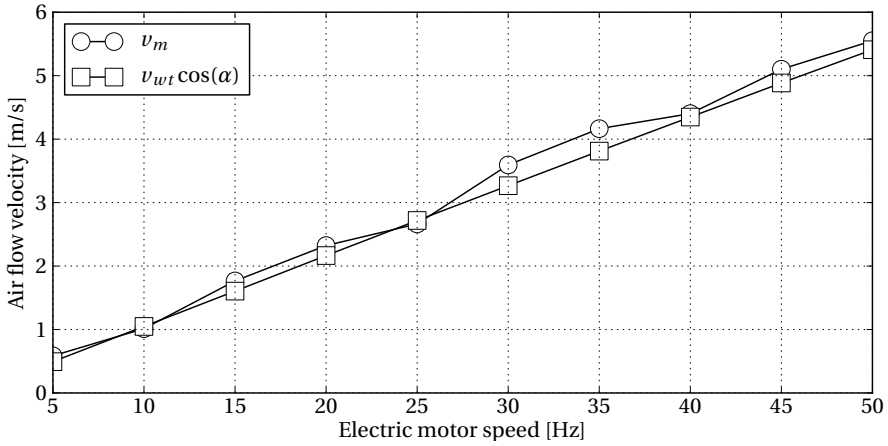

Figure A.2: Ultrasonic anemometer test results for $\alpha = 20°$

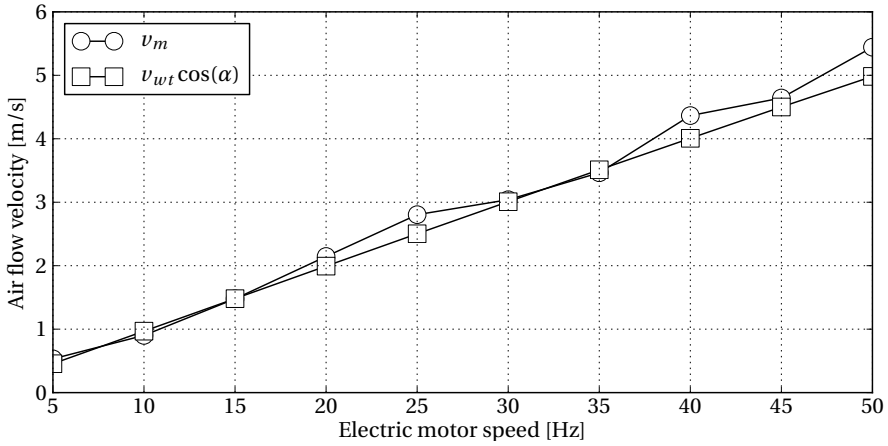

Figure A.3: Ultrasonic anemometer test results for $\alpha = 30°$

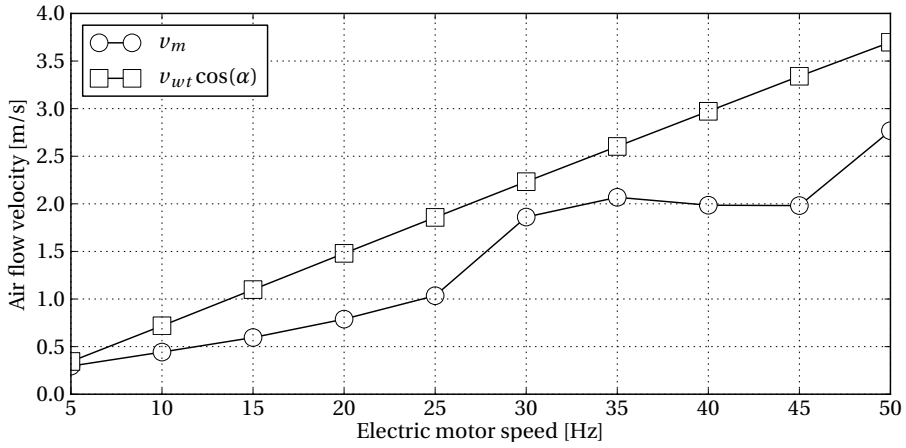

Figure A.4: Ultrasonic anemometer test results for $\alpha = 50°$

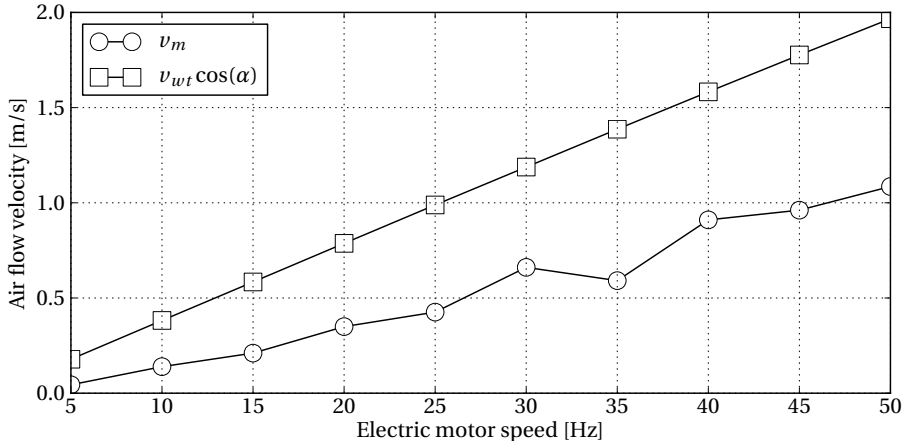

Figure A.5: Ultrasonic anemometer test results for $\alpha = 70°$

A.2 Propeller anemometer test results

As described in Section 3.2, a R.M. Young propeller anemometer was tested in order to determine its output when subjected to air flow that is not parallel to its axis of measurement. The anemometer was placed within a wind tunnel, in a bracket which could be used to adjust the angle of its measurement axis. By changing the orientation of the anemometer, the inlet air flow angle, β, is altered. With the anemometer in the wind tunnel, three separate tests were conducted with the fan speed set at 10 Hz, 25 Hz and 40 Hz. The anemometer was the set at angles ranging from $\beta = 0°$ to $\beta = 90°$ in increments of 10° and its output recorded.

Figure A.6 shows the results for the test where the fan speed was set to 10 Hz while Figure A.7 presents the results obtained at a fan speed of 25 Hz. The results for a fan speed of 40 Hz can be found in Figure 3.7b. From these results it was concluded that the anemometer only measures the component of air flow that is parallel to its own axis.

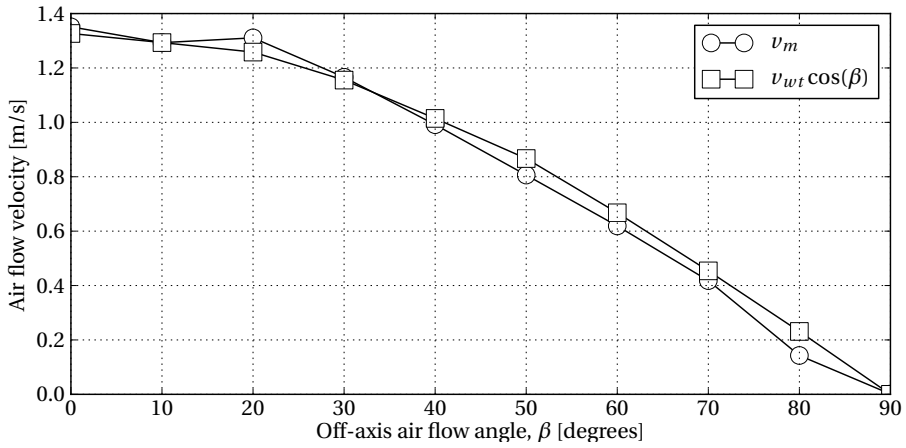

Figure A.6: Propeller anemometer test results for off-axis flow angles at 10 Hz

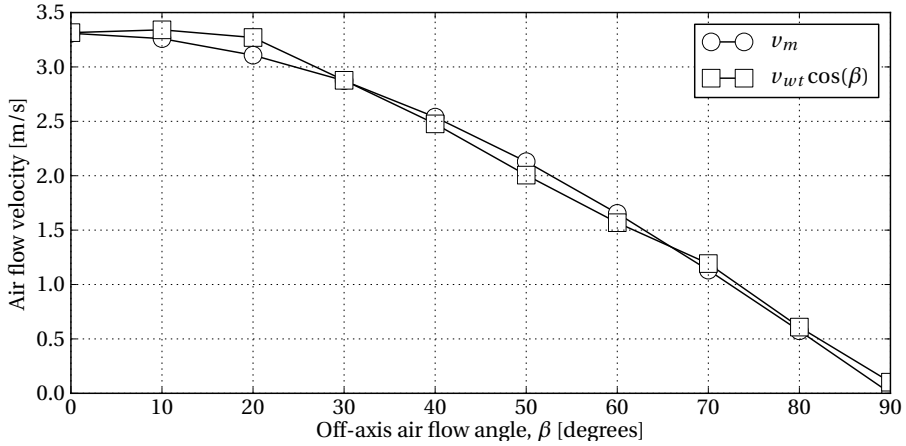

Figure A.7: Propeller anemometer test results for off-axis flow angles at 25 Hz

Appendix B

Measurement results

The measurements recorded over the period of 8 days between 14/11/2011 and 22/11/2011 are discussed in Chapter 5. This section displays the remaining sets of data which were not included in the main document, and provides explanations of the observations made.

B.1 Inlet air flow velocities

This section presents the inlet air flow measurements that were recorded for the 8 day measurement period. The directional conventions used in this section are illustrated in Figure 1.18 and reiterated in Figure 4.15. According to this convention, the y-direction represents the vertical direction into the fan while the x-direction is parallel to the longitudinal axis of the ACSC and the z-direction is parallel to its lateral axis. In addition, the indicated locations of each measurement station is described as a distance along the z-axis with the fan casing on the peripheral side being at $z = 0$ m. Therefore, the $z = 7.870$ m location refers to the measurement station placed closest to the turbine side of the fan casing, 7.870 m away from fan casing on the peripheral side of the fan.

Figure B.1 shows the air flow velocities that were measured in the y-direction on 14/11/2011. The average air flow velocity on this day was approximately 10 m/s with various drops to 0 m/s. Figure B.2 and Figure B.3 present the cross-flow velocities measured at the fan inlet in the z- and x-directions on 14/11/2011. The air flow velocities in the z-direction varied between 4 m/s and 1 m/s with drops at the same times as the drops in velocities in the y-direction. These drops in velocity coincide with sudden increases in the air flow velocity in the x-direction, which throughout the day varied between -1 m/s and 3 m/s.

Figure B.4 shows the air flow velocity in the y-direction measured on 16/11/2011. The velocity in this direction remained between -1 m/s and 6 m/s with higher air flow velocities measured on the peripheral side of the fan. The air flow velocities in the z-direction, shown in Figure B.5, varied between -4 m/s and 4 m/s while the velocities measured in the x-direction, which can be seen in Figure B.6, were between -2 m/s and 4 m/s.

The air flow velocities measured in the y-direction on the remaining days can be seen in Section 5.1. The cross-flow velocities in the z- and x-directions measured on 17/11/2011 are presented in Figure B.7 and Figure B.8, respectively. The air flow velocities in the z-direction were between -2 m/s and 4 m/s while the velocities measured in the x-direction varied between -2 m/s and 2 m/s.

Cross-flow velocities measured on 18/11/2011 are shown in Figure B.9 and Figure B.10. The cross-flow velocities in the z-direction varied between -4 m/s and 4 m/s while the cross-flow velocities in the x-direction were between -2 m/s and 4 m/s with a gradual decrease to 2 m/s during the course of the day.

On 19/11/2011, the cross-flow velocities measured at the fan inlet were between -4 m/s and 4 m/s in the z-direction (see Figure B.11) and between -2 m/s and 4 m/s in the x-direction (see Figure B.12). However, the cross-flow in the x-direction underwent a sudden decrease after 17:00 to approximately 0 m/s due to the increased wind conditions from the East, shown in Figure 5.3.

Figure B.13 shows the cross-flow velocities in the z-direction that was measured on 20/11/11 which was between -4 m/s and 2 m/s. However, at 17:00 the air flow velocities increased to 6 m/s. The air flow velocities in the x-direction on this day are shown in Figure B.14 where one can see that it varied between -2 m/s and 4 m/s.

The cross-flow velocities that were measured in the z-direction on 21/11/2011 are shown in Figure B.15 and were between -2 m/s and 4 m/s. Figure B.16 presents the air flow velocities in the x-direction which varied between -2 m/s and 0 m/s.

The cross-flow velocities that were measured in the z-direction on 22/11/2011 can be seen in Figure B.17 while the air flow velocities in the x-direction are shown in Figure B.18. The velocities in the z-direction reached a maximum of 6 m/s at approximately 15:00 after which it decreased to 4 m/s. Similarly, the maximum cross-flow velocity in the x-direction was measured to be 4 m/s at 15:00 after which it reduced to 2 m/s.

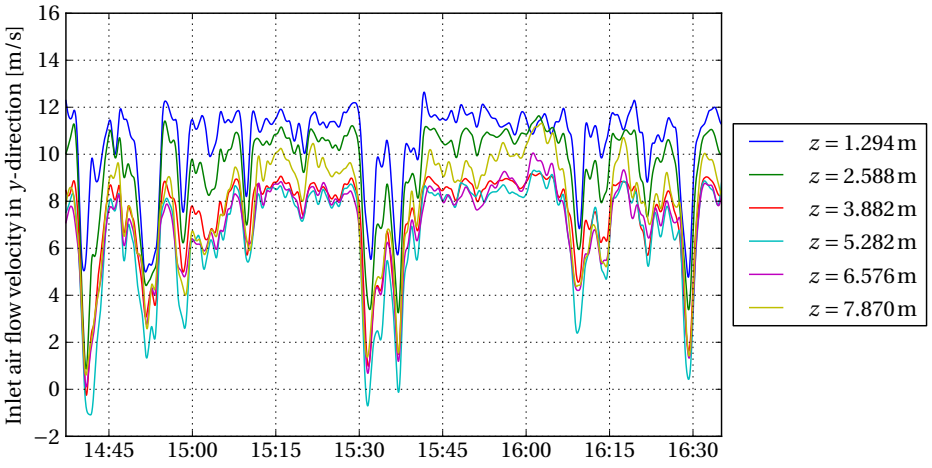

Figure B.1: Inlet air flow velocities measured in y-direction on 14/11/2011

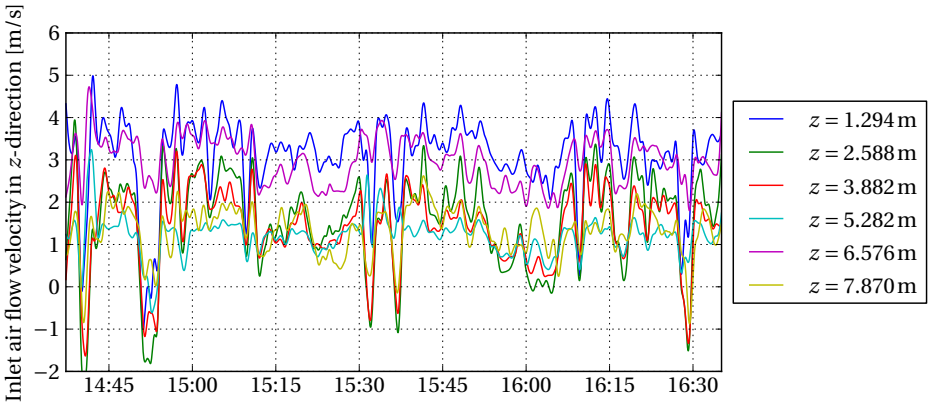

Figure B.2: Inlet air flow velocities measured in z-direction on 14/11/2011

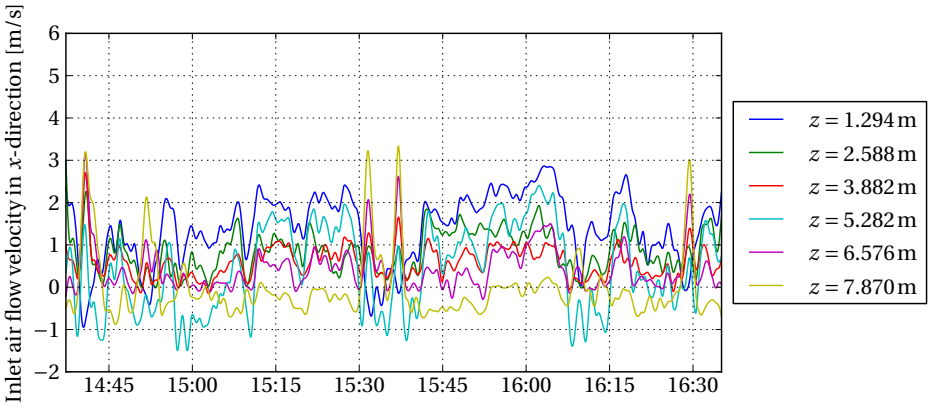

Figure B.3: Inlet air flow velocities measured in x-direction on 14/11/2011

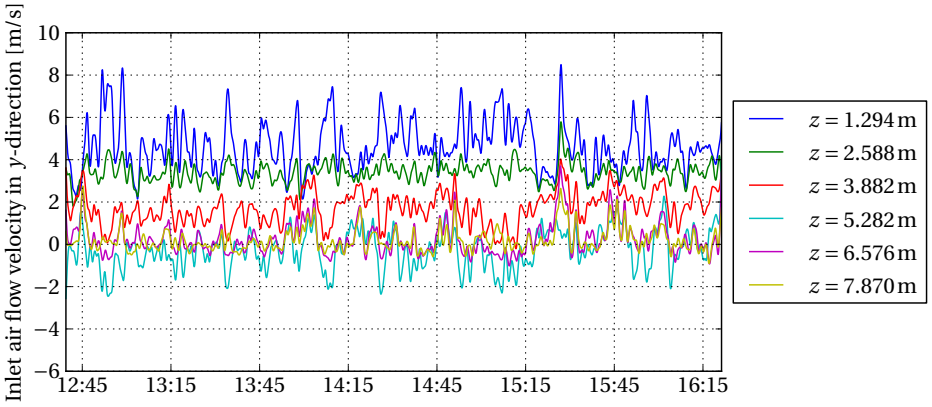

Figure B.4: Inlet air flow velocities measured in y-direction on 16/11/2011

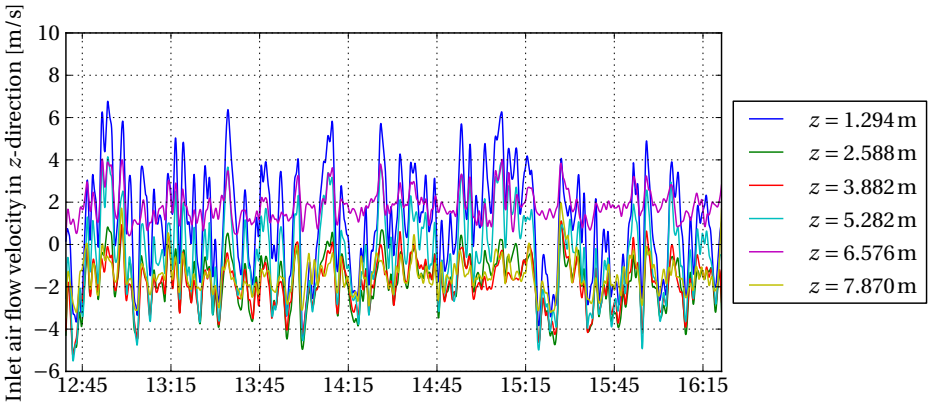

Figure B.5: Inlet air flow velocities measured in z-direction on 16/11/2011

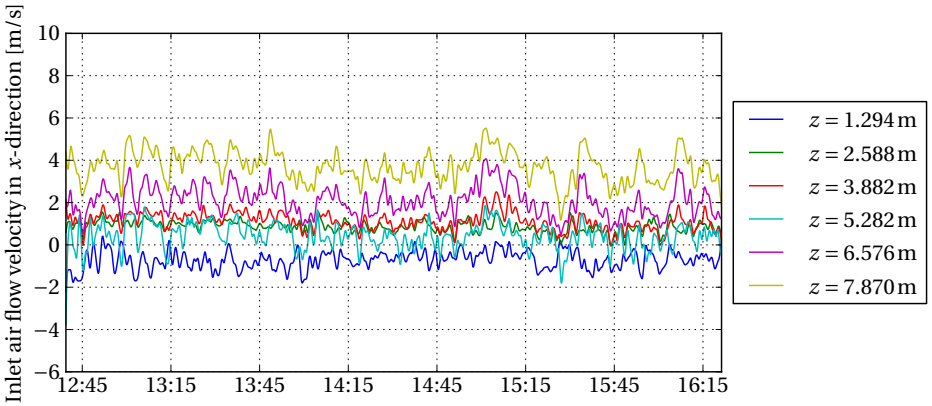

Figure B.6: Inlet air flow velocities measured in x-direction on 16/11/2011

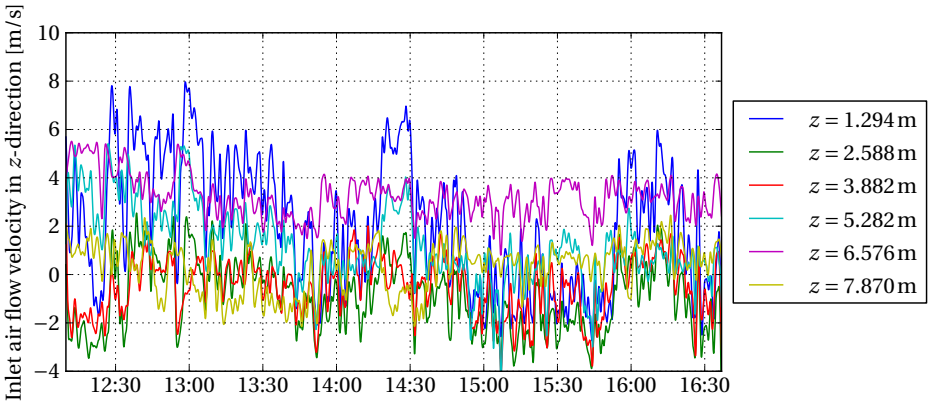

Figure B.7: Inlet air flow velocities measured in z-direction on 17/11/2011

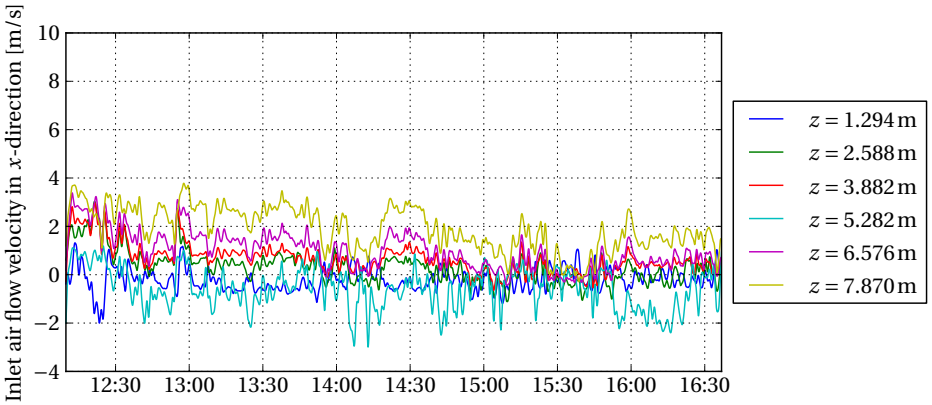

Figure B.8: Inlet air flow velocities measured in x-direction on 17/11/2011

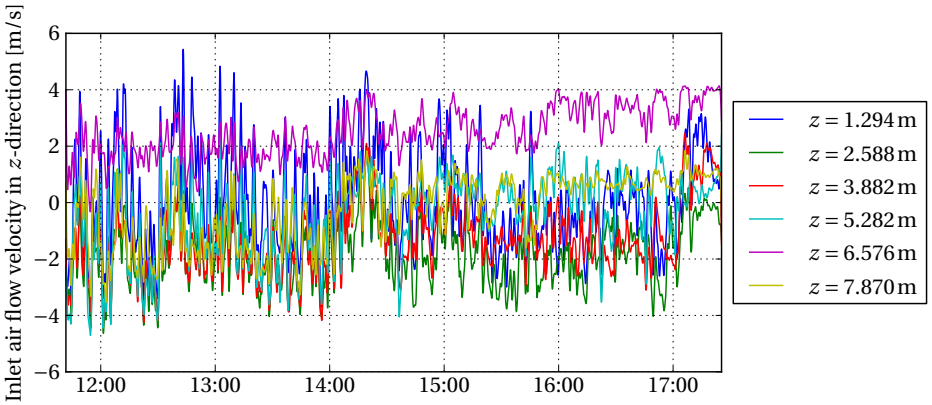

Figure B.9: Inlet air flow velocities measured in z-direction on 18/11/2011

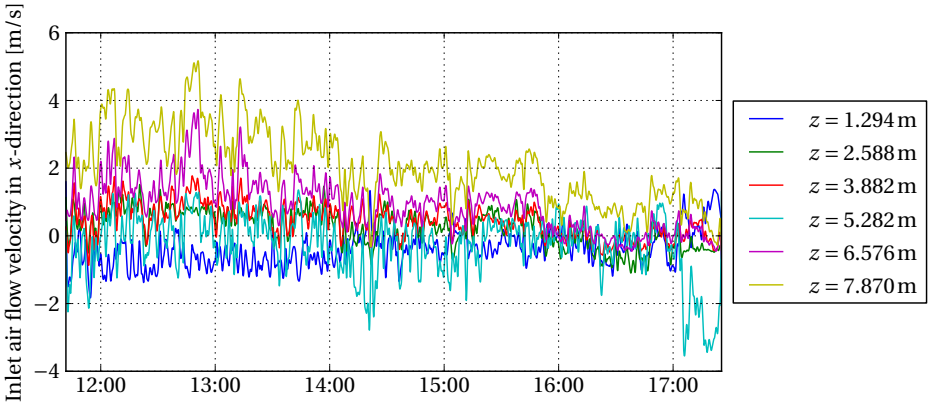

Figure B.10: Inlet air flow velocities measured in x-direction on 18/11/2011

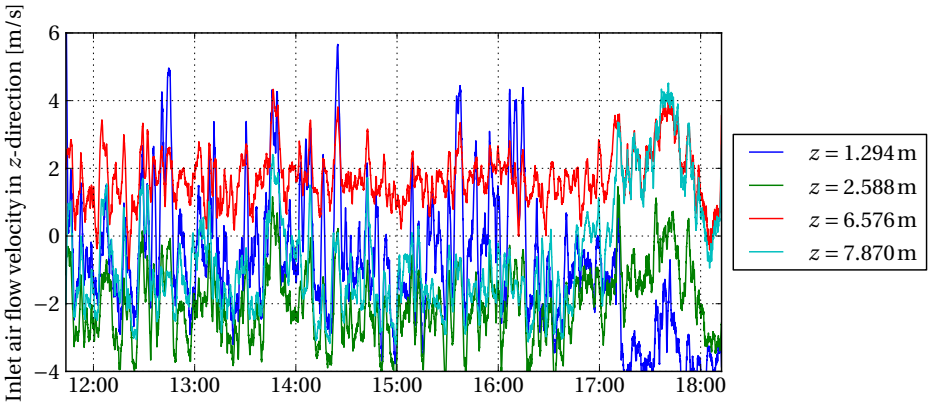

Figure B.11: Inlet air flow velocities measured in z-direction on 19/11/2011

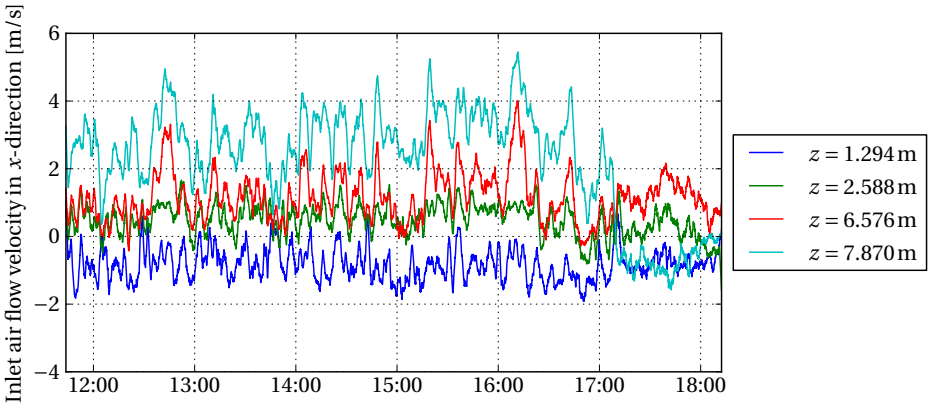

Figure B.12: Inlet air flow velocities measured in x-direction on 19/11/2011

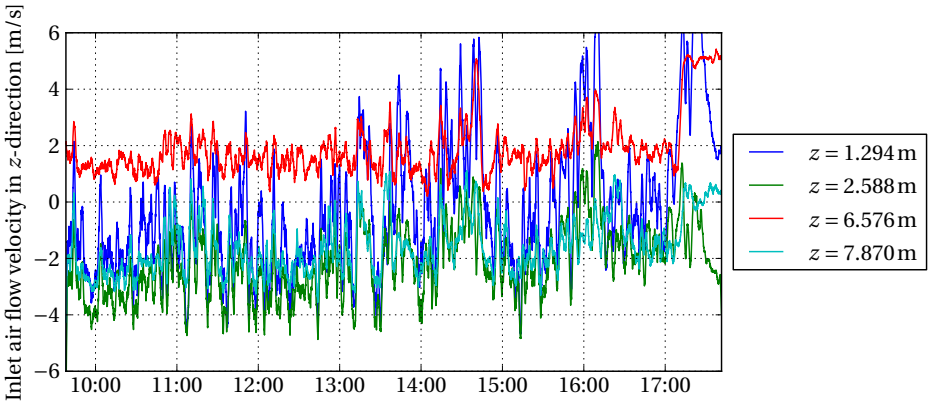

Figure B.13: Inlet air flow velocities measured in z-direction on 20/11/2011

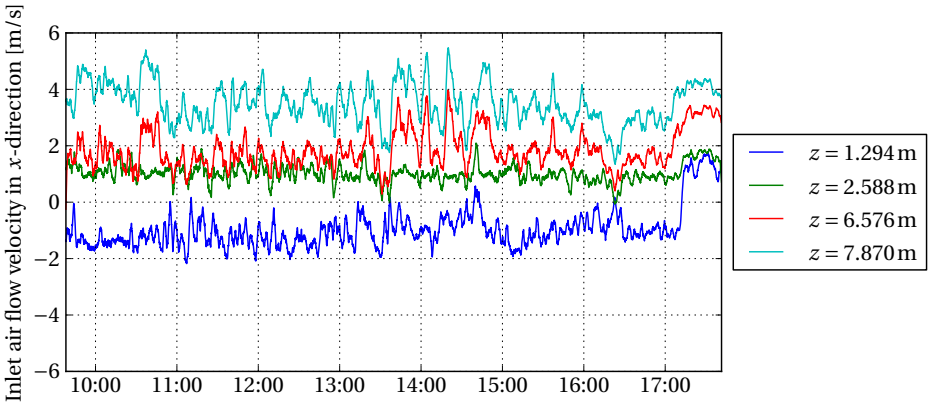

Figure B.14: Inlet air flow velocities measured in x-direction on 20/11/2011

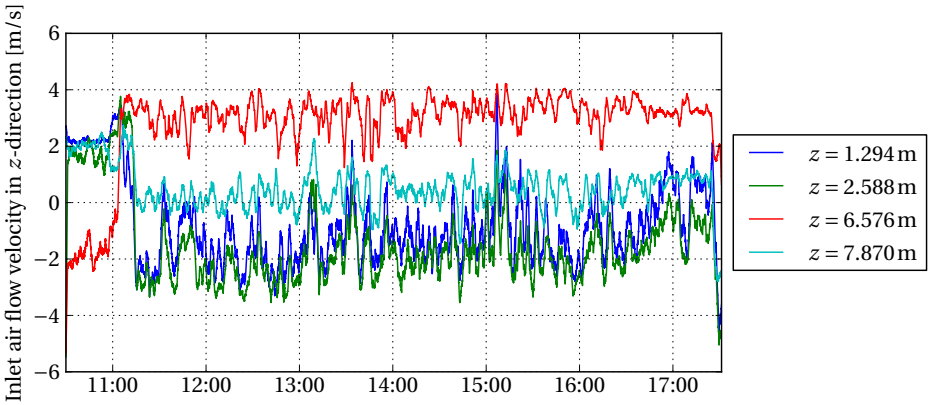

Figure B.15: Inlet air flow velocities measured in z-direction on 21/11/2011

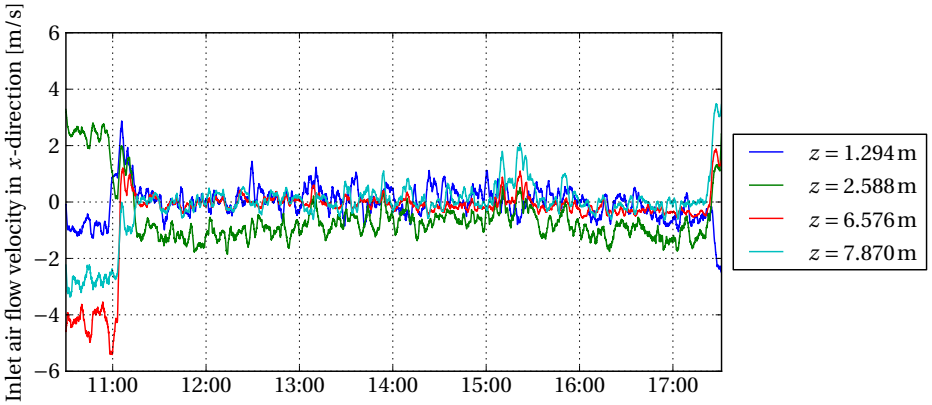

Figure B.16: Inlet air flow velocities measured in x-direction on 21/11/2011

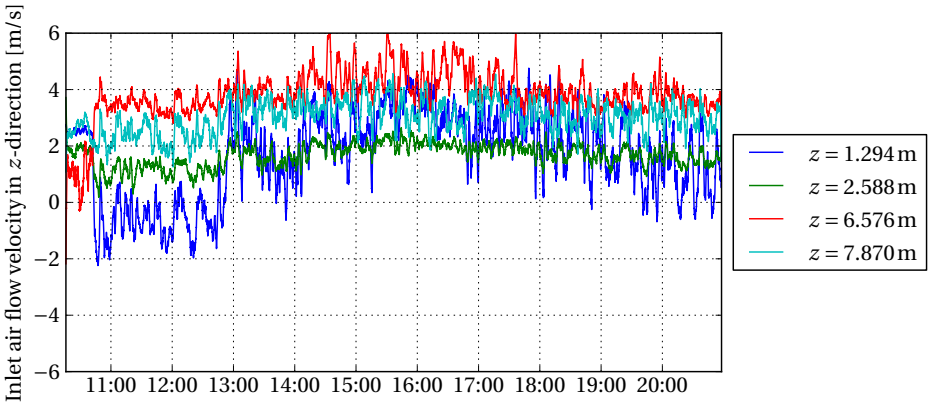

Figure B.17: Inlet air flow velocities measured in z-direction on 22/11/2011

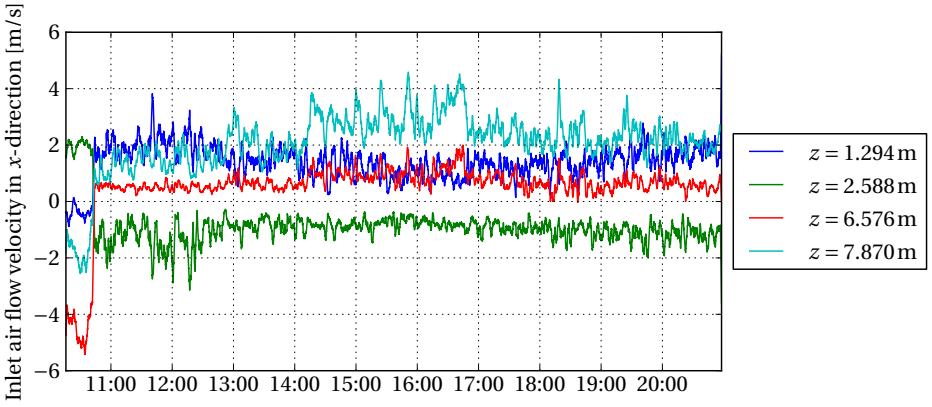

Figure B.18: Inlet air flow velocities measured in x-direction on 22/11/2011

B.2 Inlet air flow temperatures

The inlet air flow temperatures were measured with thermocouples attached to the measurement stations placed at the fan inlet. These measurement stations are described in Section 5.1. The current section displays the temperature measurements recorded by these thermocouples with the temperature measurements gathered from the weather mast located approximately 700 m North-West of the ACSC.

On 14/11/2011 and 16/11/2011 the weather mast was not yet functioning and as such there are no ambient temperature measurements available for these days. On 14/11/2011 the temperatures, which can be seen in Figure B.19, were between 35°C and 40°C with various short temperature spikes reaching approximately 48°C. Of note is the fact that the temperatures measured on the peripheral side of the fan were higher than those measured on the turbine side. The measurements recorded on 16/11/2011, shown in

Figure B.20, exhibit the same trends over a wider temperature range of between 30°C and 45°C with spikes of up to 50°C.

As the weather mast was again functioning from 17/11/2011, ambient temperatures could be included in the temperature measurements for the remaining days that measurements were recorded. On 18/11/2011 the measured temperatures, shown in Figure B.21, were between 30°C and 50°C with the ambient temperature climbing from 29°C to 35°C during the course of the day. The measured temperatures exhibited a similar increase.

The temperatures measured on 20/11/2011, shown in Figure B.22, followed the increase in ambient temperature from 24°C to 30°. Once again the temperatures measured on the peripheral side of the fan were higher than those measured on the turbine side.

On 21/11/2011 the inlet air flow temperatures were measured to be between 25°C and 40°while the ambient air temperature increased from 28°C to 31°. The temperatures measured on 21/11/2011 is presented in Figure B.23.

The inlet air flow temperatures that were measured on 22/11/2011 and shown in Figure B.24 decreased from a maximum of 40°C at 10:30 to 35°at 18:30. This decrease is due to decrease in ambient temperature from 25°C to 20°over the same time period.

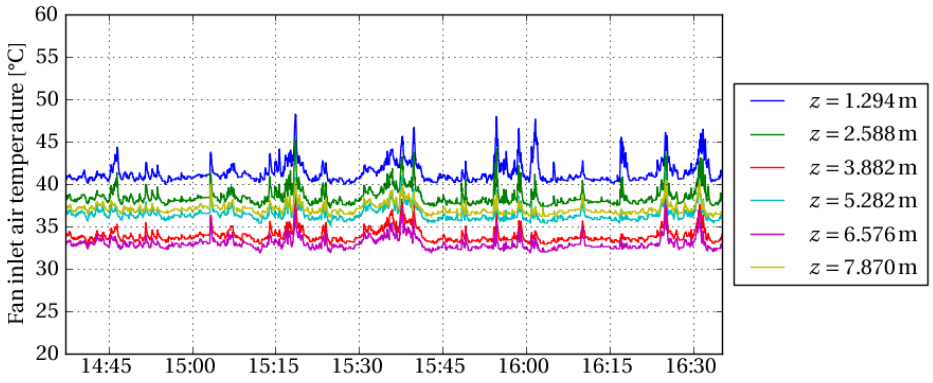

Figure B.19: Temperature measurements recorded on 14/11/2011

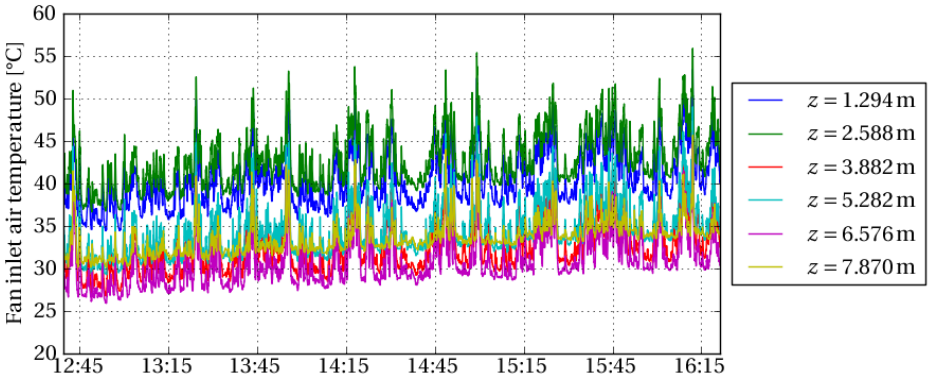

Figure B.20: Temperature measurements recorded on 16/11/2011

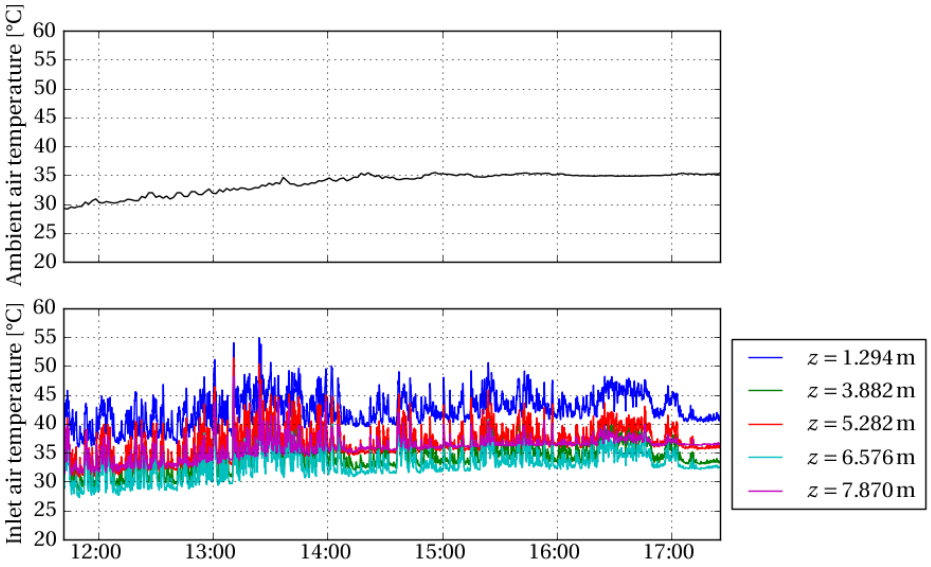

Figure B.21: Temperature measurements recorded on 18/11/2011

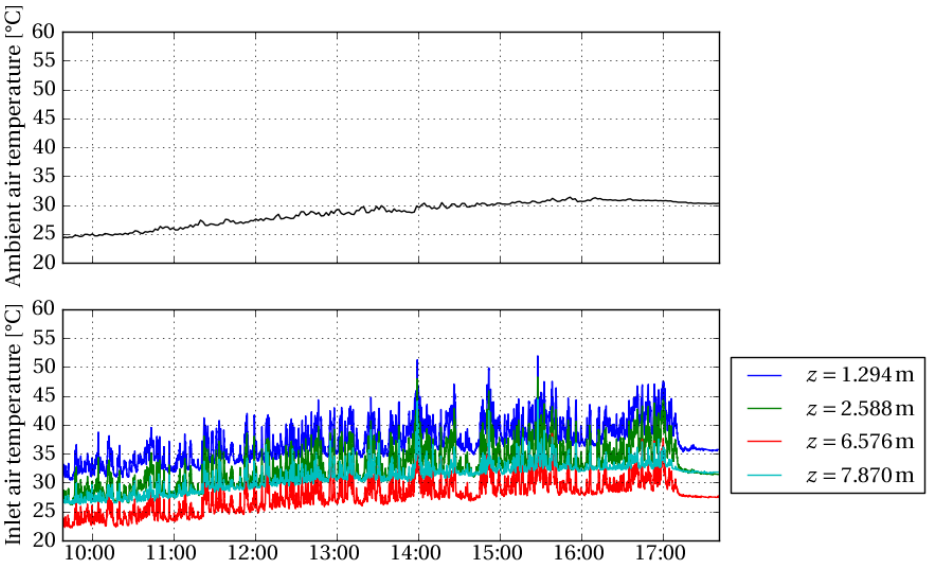

Figure B.22: Temperature measurements recorded on 20/11/2011

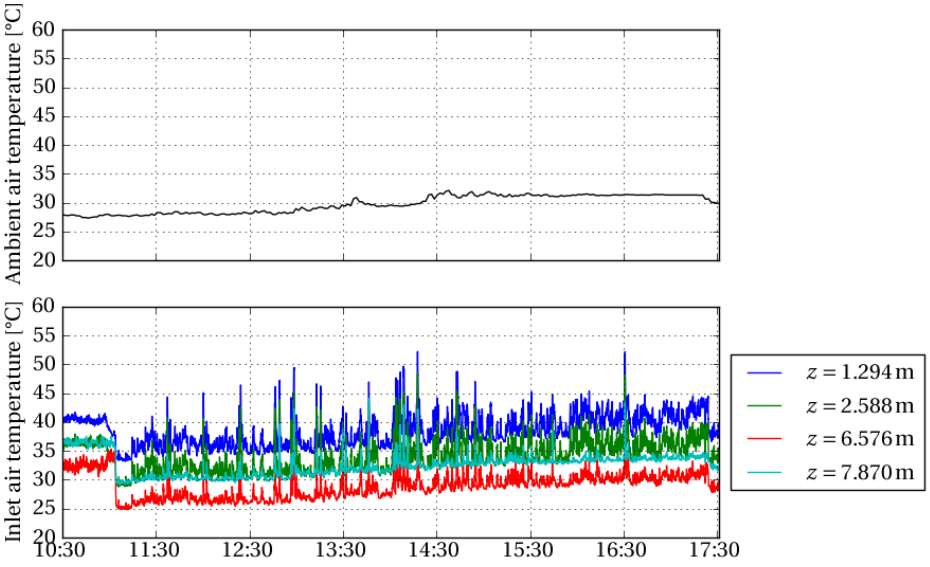

Figure B.23: Temperature measurements recorded on 21/11/2011

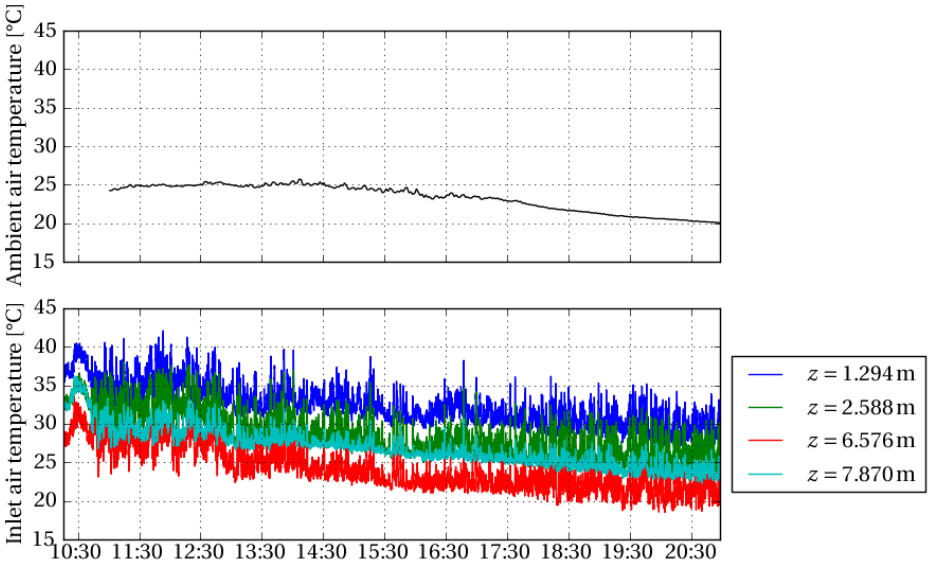

Figure B.24: Temperature measurements recorded on 22/11/2011

B.3 Bundle outlet air flow velocities

The following graphs show the air flow measured at the heat exchanger bundle outlets. Measurements were taken on the Northern and Southern sides of the A-frame configuration from 19/11/11 to 22/11/11. The position of each anemometer is indicated from the peripheral side of the fan. Position 1 refers to the anemometer placed closest to the peripheral side of the fan while position 4 is the anemometer placed on the turbine side of the fan.

On 20/11/2011 the air flow velocities measured at the heat exchanger bundle outlet were between 1 m/s and 3 m/s on the Northern and Southern sides of the fan unit. The velocities measured on 20/11/2011 for the Northern and Southern heat exchanger bundles are shown in Figure B.25 and Figure B.26, respectively.

Bundle outlet air flow velocities as measured on 21/11/2011 are shown in Figure B.27 and Figure B.28 for the Northern and Southern heat exchangers, respectively. The air flow velocities were between 1 m/s and 3 m/s on both sides of the fan unit.

Figure B.29 and Figure B.30 show the bundle outlet air flow velocities for the Northern and Southern heat exchanger bundles measured on 22/11/2011. The air flow velocities measured at the outlet the Northern bundles were between 1 m/s and 3 m/s while the velocities measured at the Southern bundles were between 2 m/s and 3 m/s.

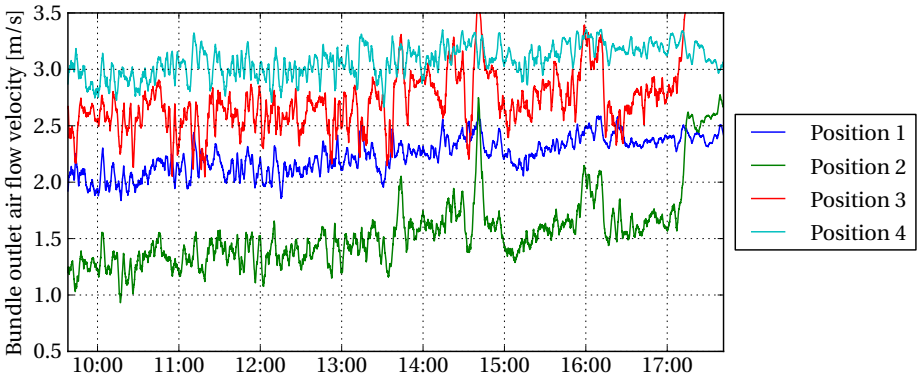

Figure B.25: Air flow through Northern heat exchanger bundles on 20/11/2011

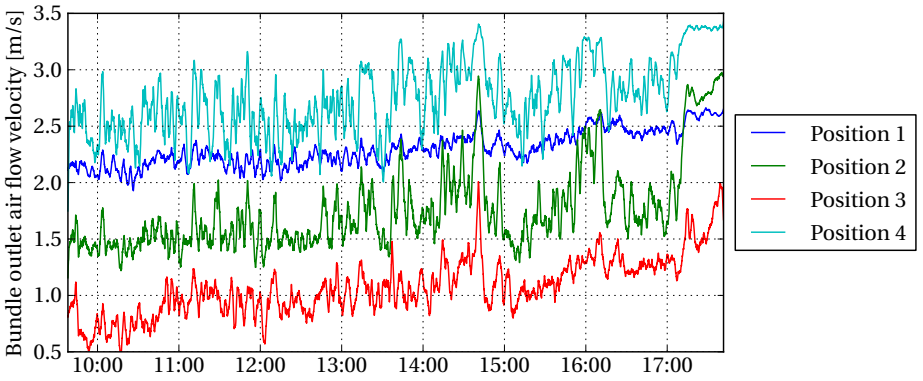

Figure B.26: Air flow through Southern heat exchanger bundles on 20/11/2011

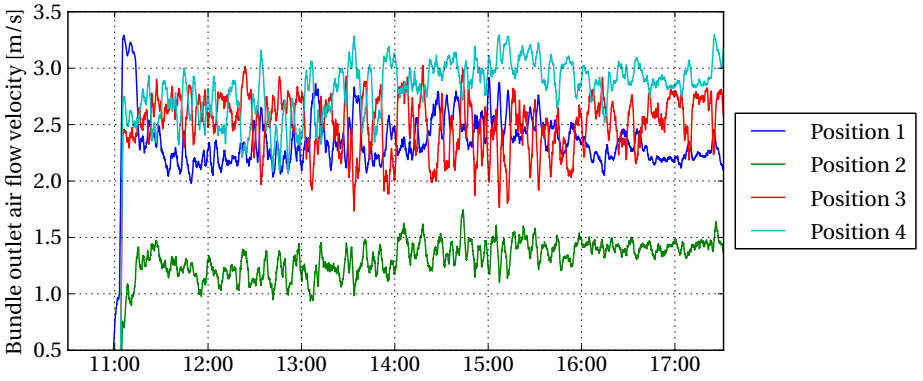

Figure B.27: Air flow through Northern heat exchanger bundles on 21/11/2011

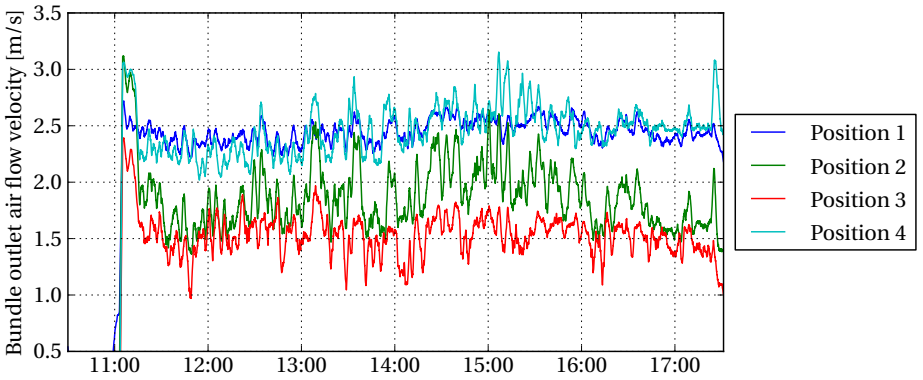

Figure B.28: Air flow through Southern heat exchanger bundles on 21/11/2011

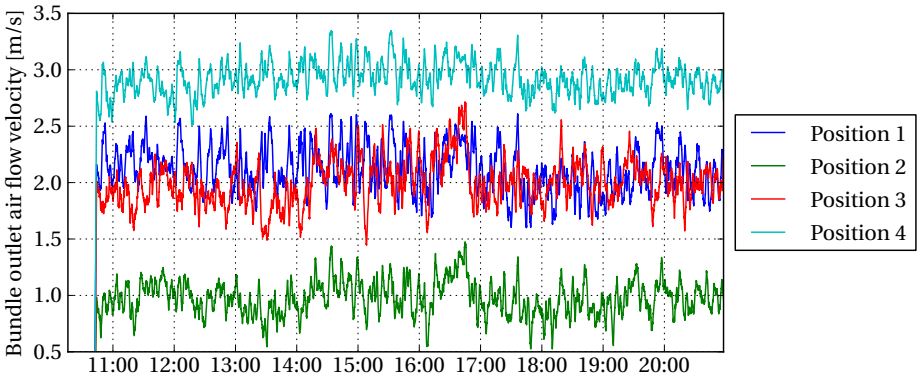

Figure B.29: Air flow through Northern heat exchanger bundles on 22/11/2011

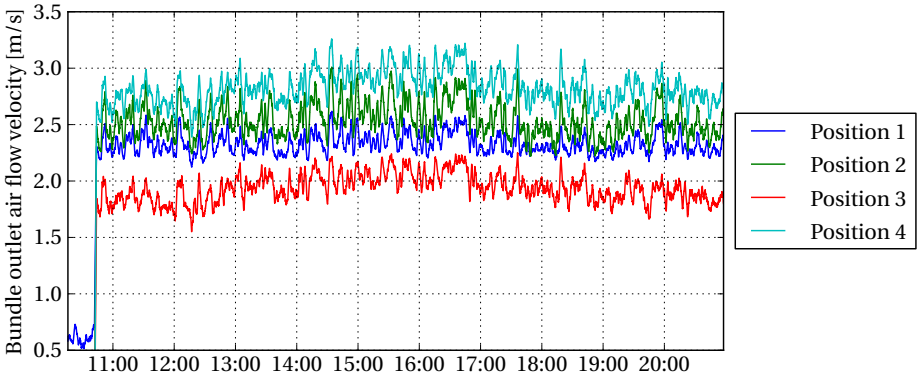

Figure B.30: Air flow through Southern heat exchanger bundles on 22/11/2011

B.4 Blade loading

Fan blade loading was measured in the flap- and lag-wise direction with strain gauges. Torque was also measured in the blade neck. Figure B.31 shows the bending measured in the flap-wise direction on 14/11/2011 while Figure B.32 and Figure B.33 shows the lag-wise bending and the torque, respectively. The flap-wise bending remained between 0 kN·m and 10 kN·m and the maximum torque measured was approximately 350 N·m.

Blade loading measured on 16/11/2011 is shown in Figure B.34, Figure B.35 and Figure B.36. The flap-wise blade loading reached a maximum of approximately 13.5 kN·m while the lag-wise bending load attained a maximum value of 4 kN·m.

The flap-wise bending load measured on 17/11/2011 is shown in Figure B.37 where it can be seen that the maximum load was approximately 12 kN·m. The lag-wise bending load is presented in Figure B.38 and the torque in Figure B.39.

Blade loading measured on 18/11/2011 is shown in Figure B.40 and Figure B.41. The lag-wise bending load obtained a maximum of approximately 5 kN·m while the maximum torque measured in the blade neck was 400 N·m.

The flap-wise bending load measured on 19/11/2011 is shown in Figure B.43 and reaches a maximum value of approximately 14 kN·m. The blade loading in the lag-wise direction is shown in Figure 5.14 and reaches a maximum value of approximately 6 kN·m.

Figure B.44 shows the lag-wise bending measured on 20/11/2011. The maximum lag-wise bending load measured on this day was approximately 5 kN·m. The torque measured at the blade neck is shown in Figure B.45 and attains a maximum value of approximately 350 N·m.

The flap-wise bending load measured on 21/11/2011 is presented in Figure B.46 where it is shown to obtain a maximum value of approximately 13 kN·m. The lag-wise bending load is shown in Figure B.47 and the blade neck torque can be seen in Figure B.48. The maximum measured lag-wise bending load was approximately 5 kN·m while the torque in the blade neck reached a maximum value of 350 N·m.

Blade loading measured on 22/11/2011 is shown in Figure B.34, Figure B.35 and Figure B.36. The flap-wise blade load reached a maximum of approximately 12 kN·m while the lag-wise bending load attained a maximum value of 4 kN·m while the blade neck torque was between 100 N·m and 350 N·m.

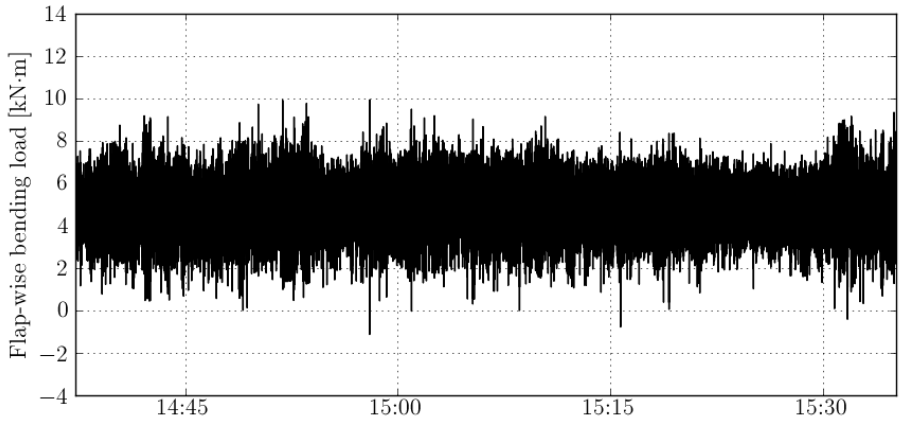

Figure B.31: Flap-wise bending load measured on 14/11/2011

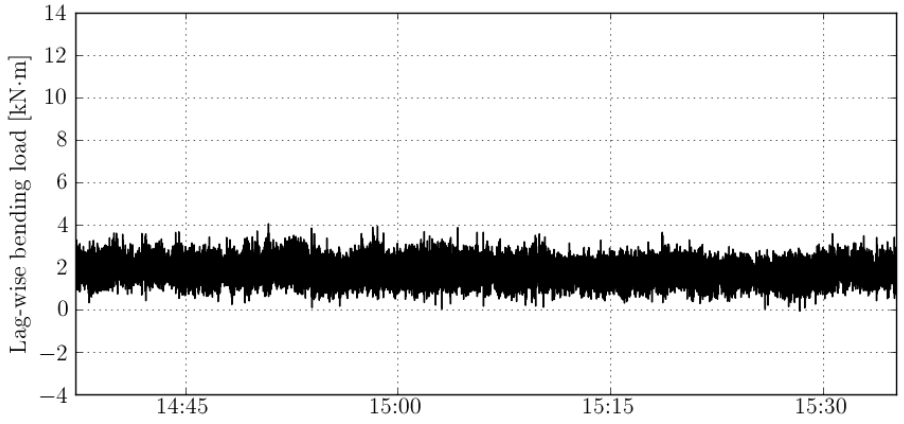

Figure B.32: Lag-wise bending load measured on 14/11/2011

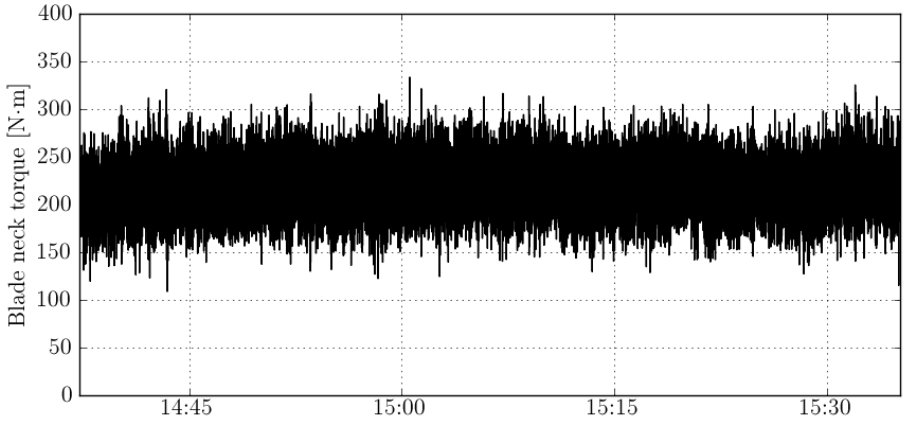

Figure B.33: Blade neck torque measured on 14/11/2011

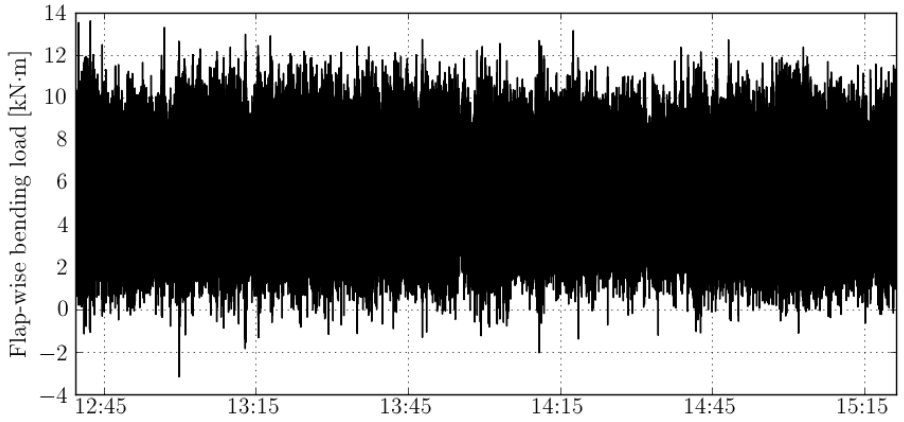

Figure B.34: Flap-wise bending load measured on 16/11/2011

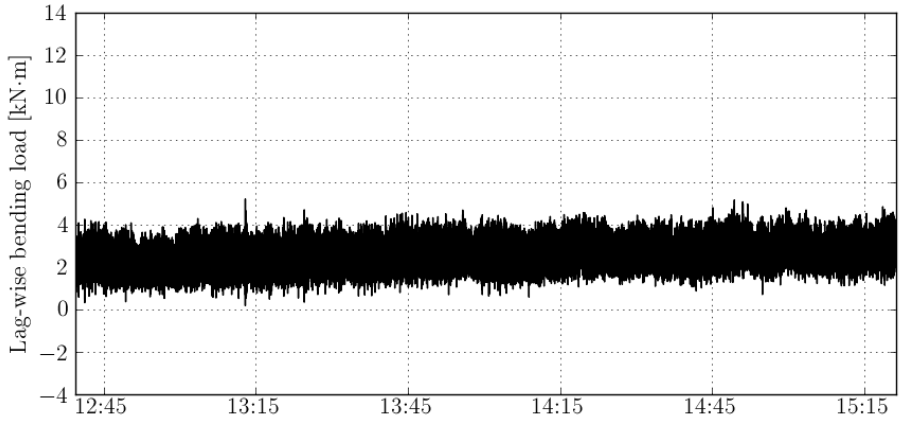

Figure B.35: Lag-wise bending load measured on 16/11/2011

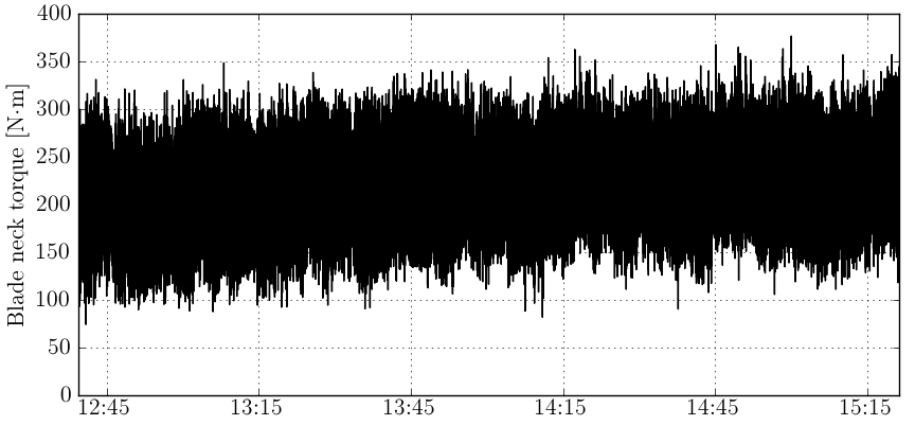

Figure B.36: Blade neck torque measured on 16/11/2011

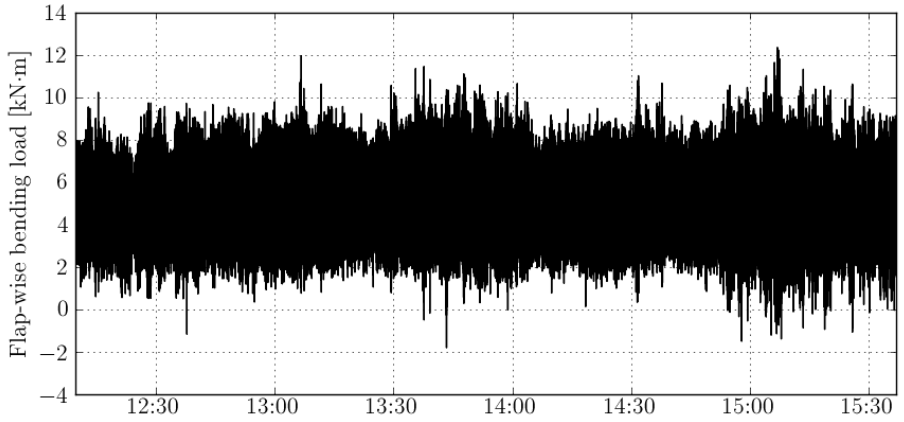

Figure B.37: Flap-wise bending load measured on 17/11/2011

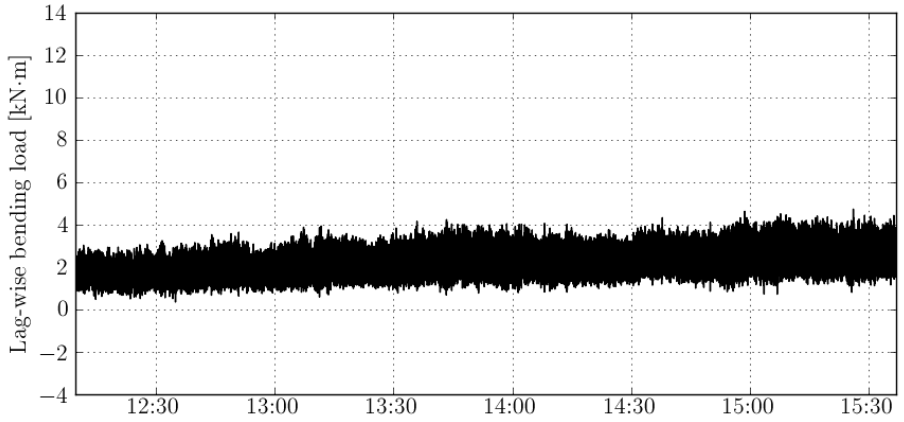

Figure B.38: Lag-wise bending load measured on 17/11/2011

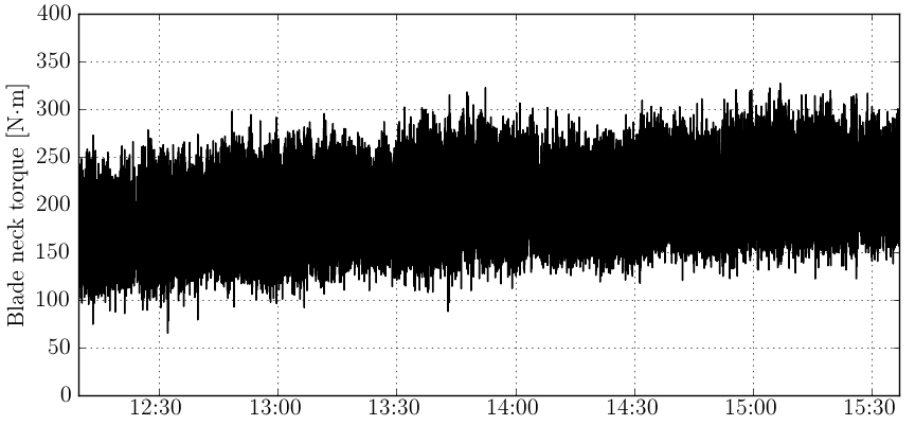

Figure B.39: Blade neck torque measured on 17/11/2011

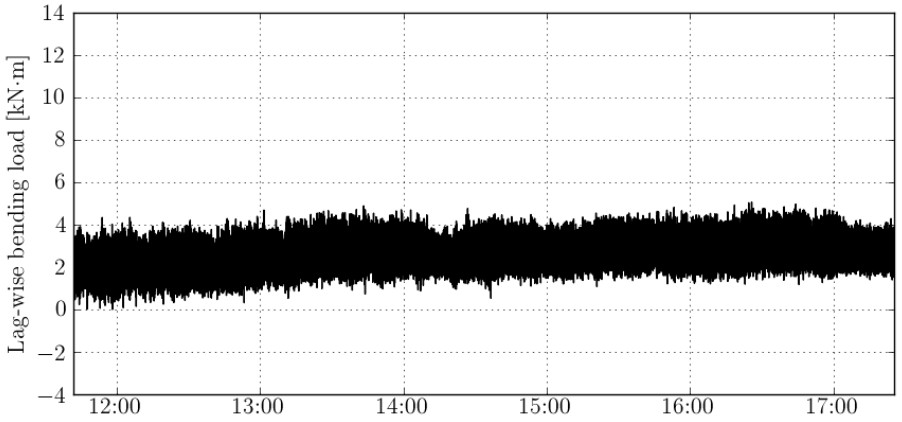

Figure B.40: Lag-wise bending load measured on 18/11/2011

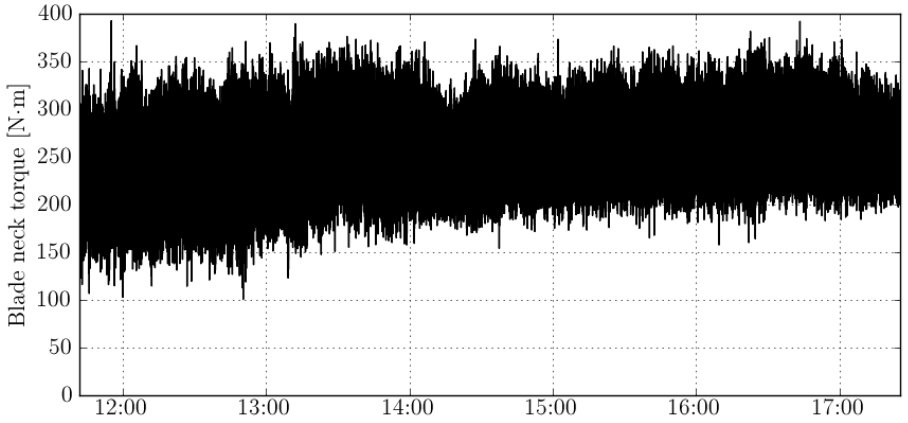

Figure B.41: Blade neck torque measured on 18/11/2011

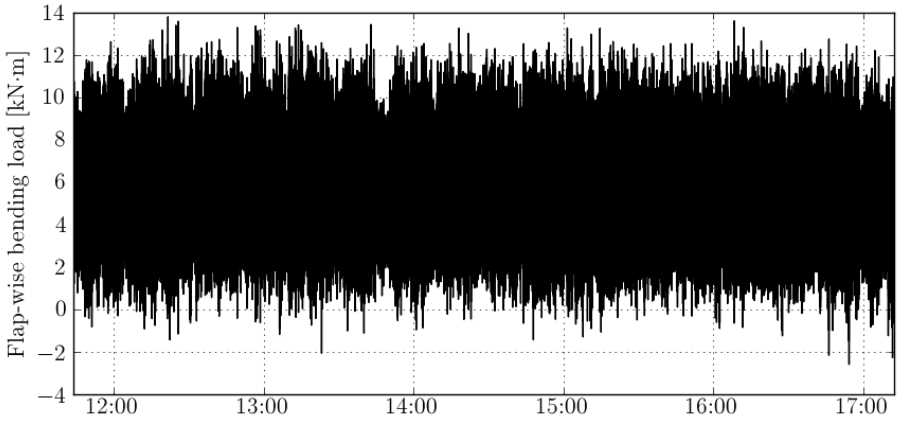

Figure B.42: Flap-wise bending load measured on 19/11/2011

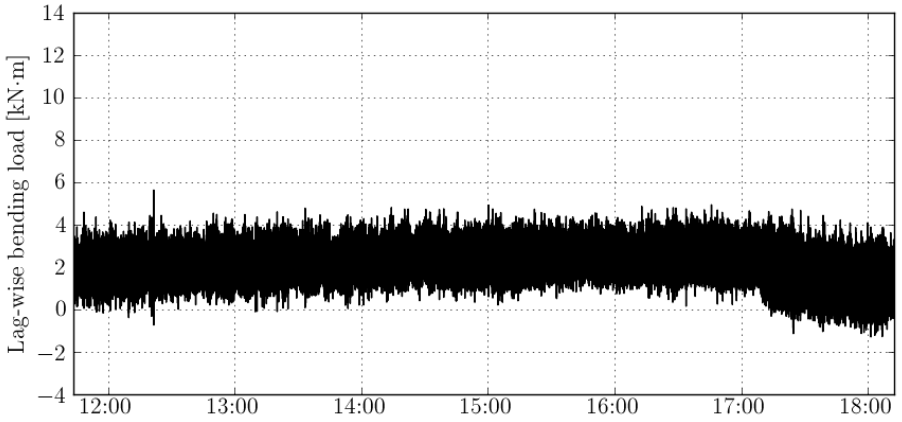

Figure B.43: Lag-wise bending load measured on 19/11/2011

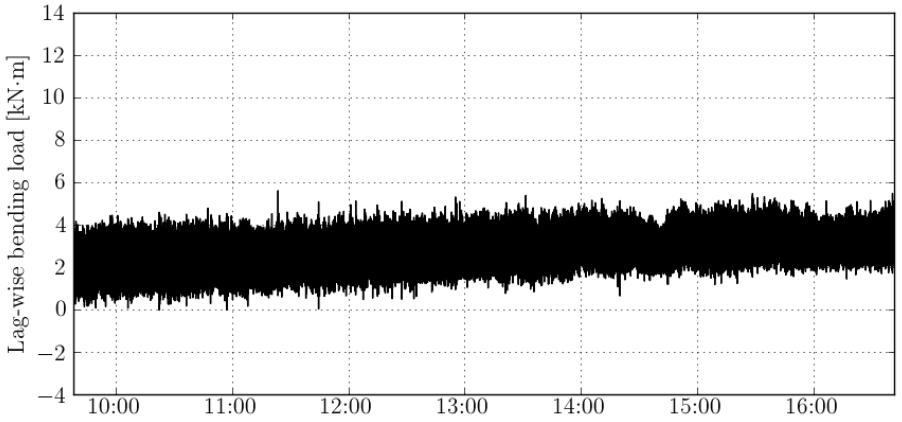

Figure B.44: Lag-wise bending load measured on 20/11/2011

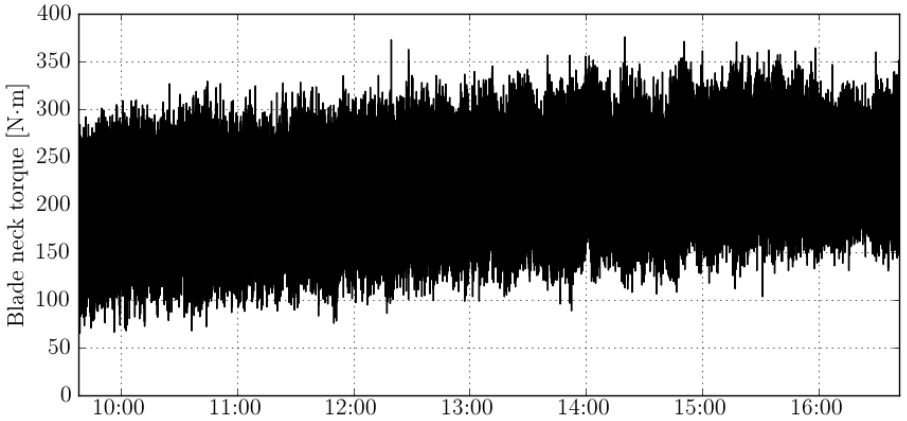

Figure B.45: Blade neck torque measured on 20/11/2011

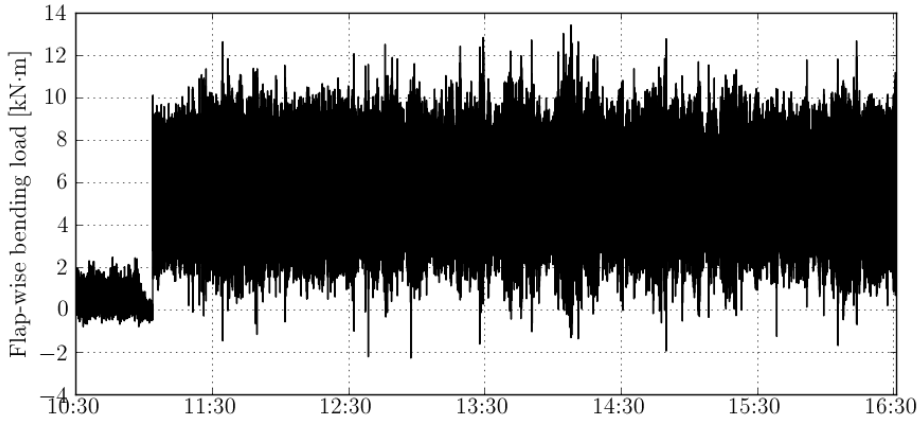

Figure B.46: Flap-wise bending load measured on 21/11/2011

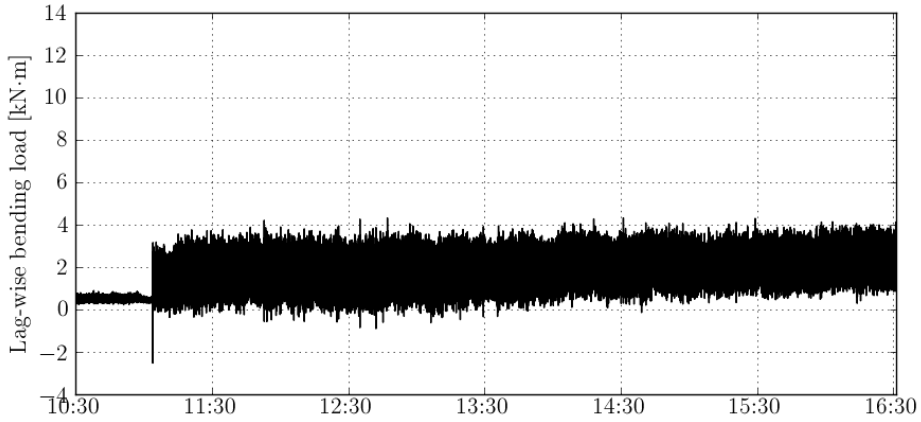

Figure B.47: Lag-wise bending load measured on 21/11/2011

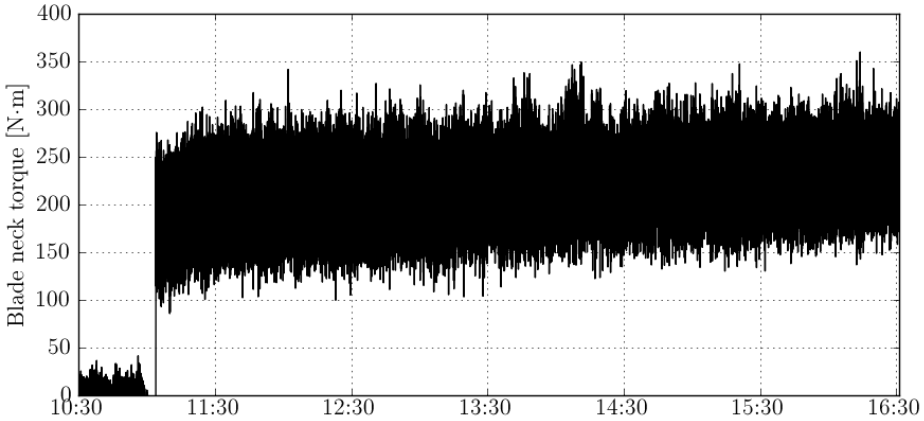

Figure B.48: Blade neck torque measured on 21/11/2011

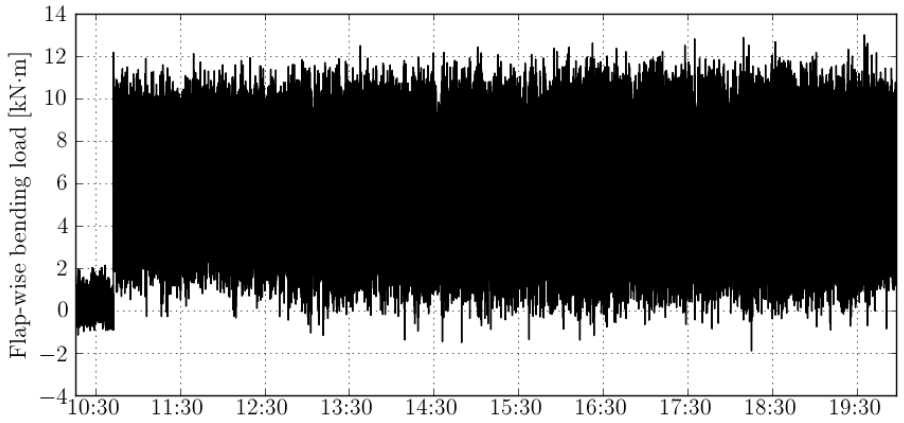

Figure B.49: Flap-wise bending load measured on 22/11/2011

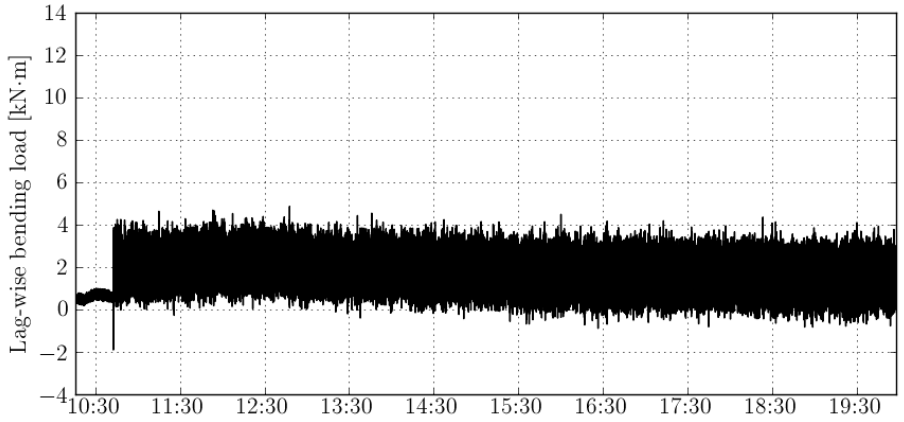

Figure B.50: Lag-wise bending load measured on 22/11/2011

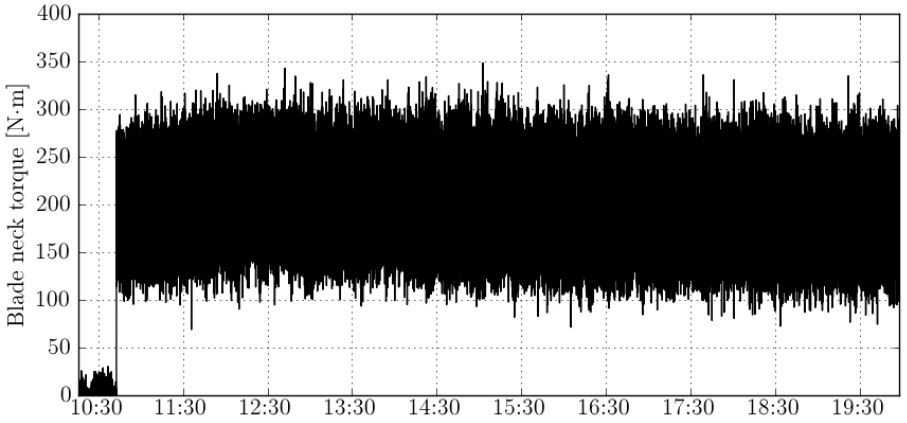

Figure B.51: Blade neck torque measured on 22/11/2011

B.5 Shaft stresses

This section provides the graphs presenting the measured fan shaft bending stresses during the 8 day measurement period. During each day the shaft bending stress varied between −20 MPa and 100 MPa. The offset in bending load indicates that the fan is subjected to a constant unbalanced load. The measured shaft loading is discussed in Section 5.5.2.

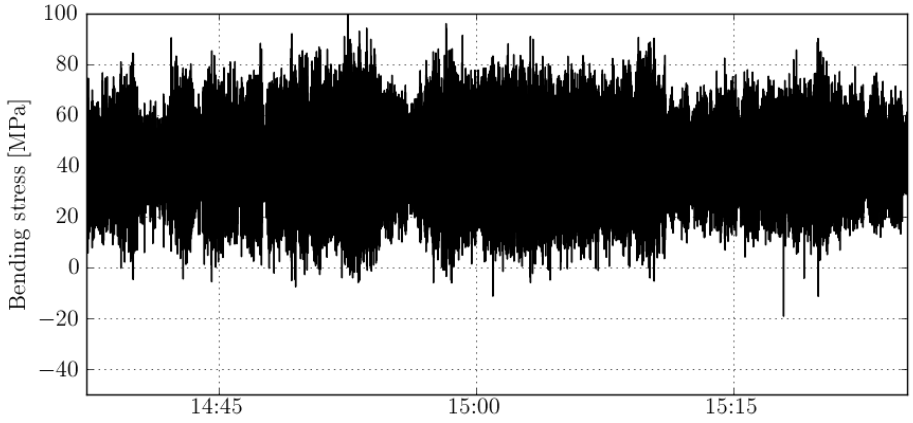

Figure B.52: Shaft bending stress measured on 14/11/2011

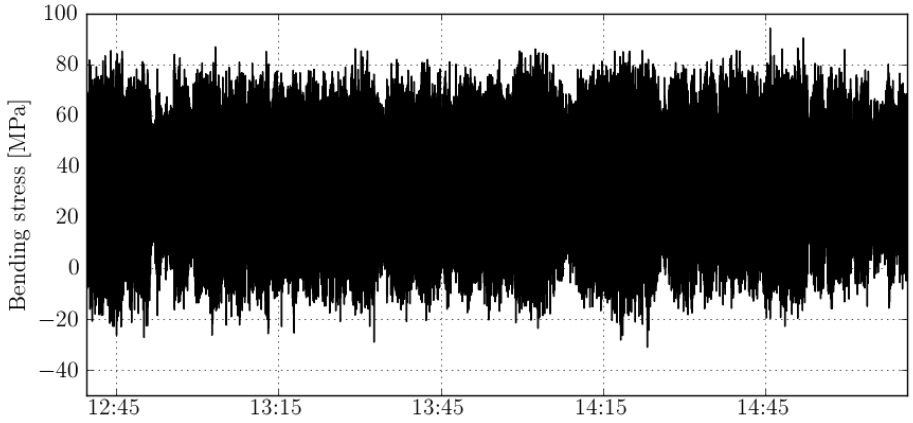

Figure B.53: Shaft bending stress measured on 16/11/2011

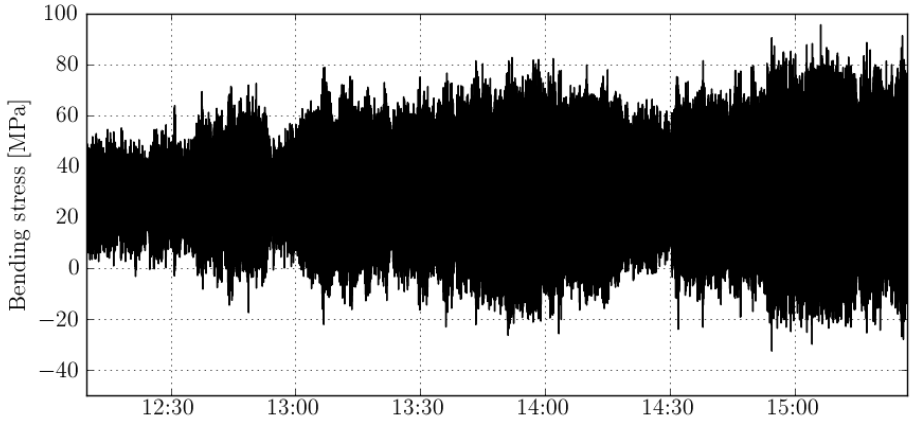

Figure B.54: Shaft bending stress measured on 17/11/2011

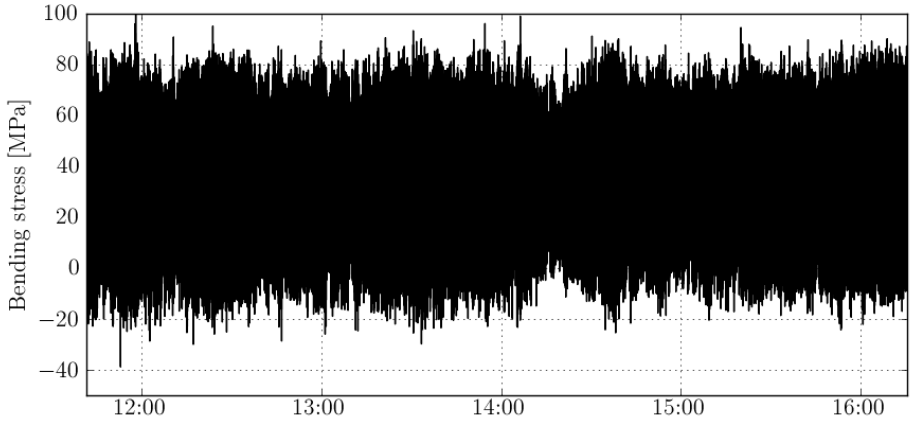

Figure B.55: Shaft bending stress measured on 18/11/2011

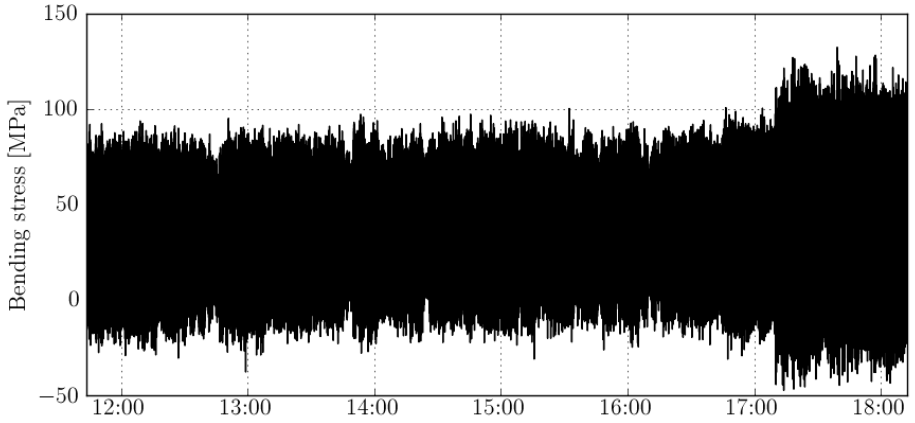

Figure B.56: Shaft bending stress measured on 19/11/2011

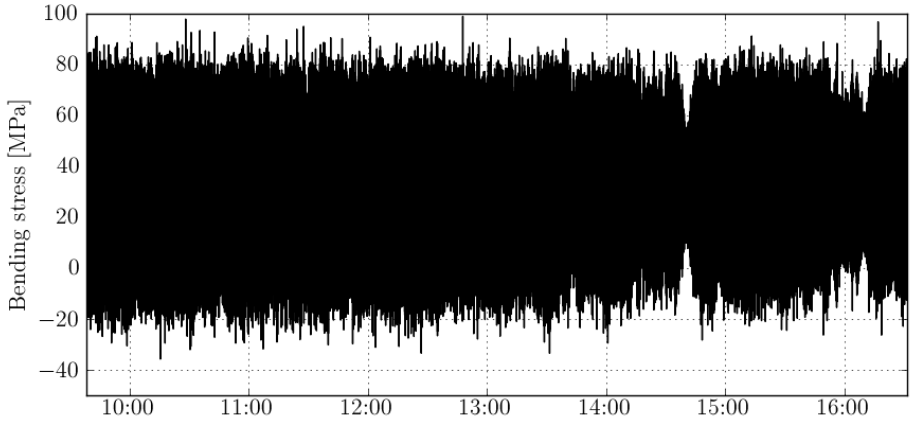

Figure B.57: Shaft bending stress measured on 20/11/2011

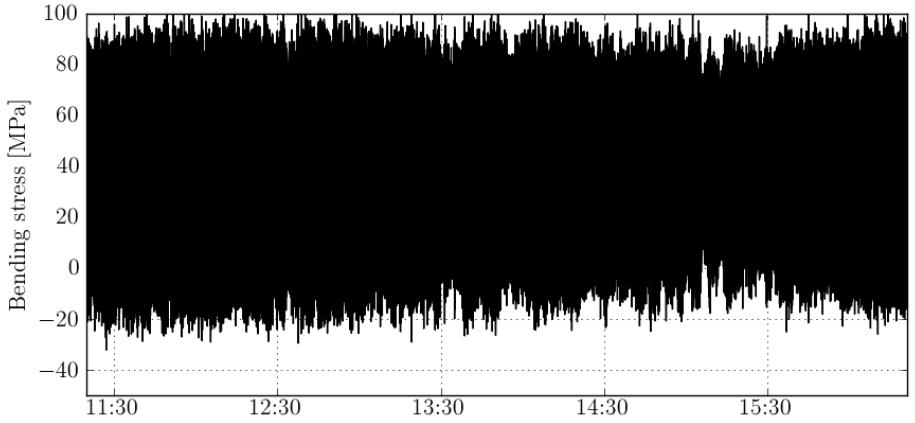

Figure B.58: Shaft bending stress measured on 21/11/2011

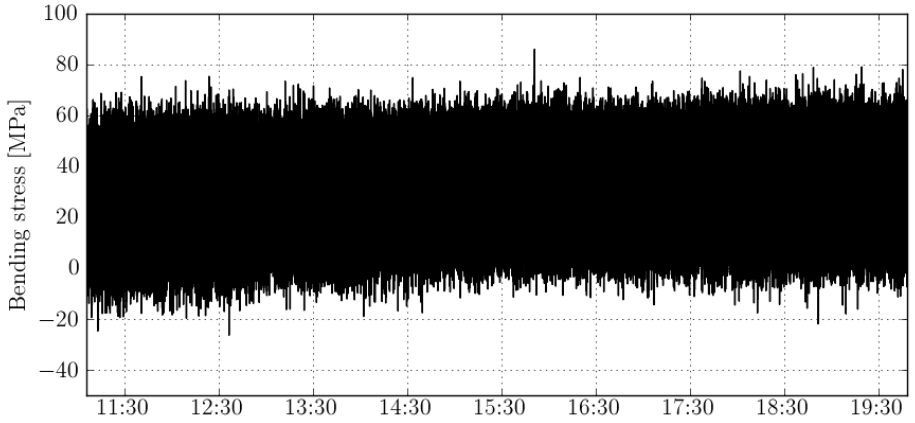

Figure B.59: Shaft bending stress measured on 22/11/2011

B.6 Shaft torque during fan start-up

Figure B.60 shows the shaft torque measured during start-up on 22/11/2011. The measured start-up effects are discussed in Section 5.7. It can be seen that there is a highly damped initial torque spike followed by a second spike once the fan reaches its operating speed.

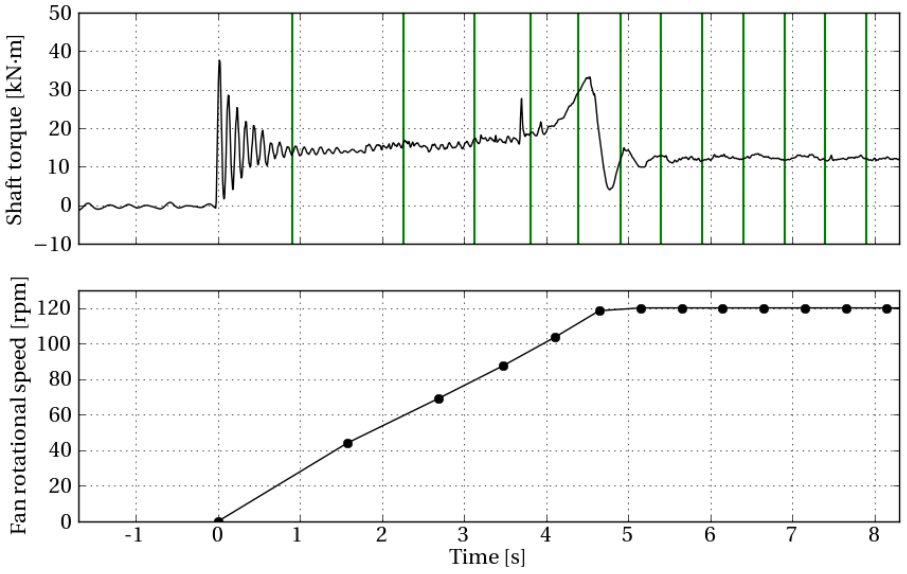

Figure B.60: Shaft torque during start-up on 22/11/2011